

Electronic Thesis and Dissertation Repository

9-24-2019 3:30 PM

Finite Element Analysis of Hollow-stemmed Shoulder Implants in Different Bone Qualities Derived from a Statistical Shape and Density Model

Pendar Soltanmohammadi
The University of Western Ontario

Supervisor
Willing, Ryan T.
The University of Western Ontario

Graduate Program in Biomedical Engineering
A thesis submitted in partial fulfillment of the requirements for the degree in Master of Engineering Science
© Pendar Soltanmohammadi 2019

Follow this and additional works at: <https://ir.lib.uwo.ca/etd>



Part of the [Biomedical Engineering and Bioengineering Commons](#)

Recommended Citation

Soltanmohammadi, Pendar, "Finite Element Analysis of Hollow-stemmed Shoulder Implants in Different Bone Qualities Derived from a Statistical Shape and Density Model" (2019). *Electronic Thesis and Dissertation Repository*. 6631.
<https://ir.lib.uwo.ca/etd/6631>

This Dissertation/Thesis is brought to you for free and open access by Scholarship@Western. It has been accepted for inclusion in Electronic Thesis and Dissertation Repository by an authorized administrator of Scholarship@Western. For more information, please contact wlsadmin@uwo.ca.

Abstract

The incidence of total shoulder arthroplasty procedures (TSA) to treat osteoarthritis has experienced the most rapid growth among all human joint replacements. However, stress shielding of proximal bone following its reconstruction is a complication of TSA triggering unfavorable adaptive bone remodeling, especially for osteoporotic patients.

A better understanding of how the shape and density of the shoulder vary among members of a population can help design more effective population-based orthopedic implants. Therefore, finite element models representing healthy, osteopenic, and osteoporotic bone qualities in a population were developed using our statistical shape and density model. Bones were reconstructed with hollow- and solid-stemmed implants and resulting changes in bone stresses were calculated. We concluded that the use of more compliant stems, such as hollow stems, could marginally mitigate the effect of stress shielding at the proximal humerus. Further increasing the compliance of stems by making them porous could improve bone-implant mechanics.

Keywords

Shoulder, Osteoarthritis, Total shoulder arthroplasty, Stress shielding, Osteoporosis, Bone mechanics, Implant design, Finite element analysis, Statistical shape model, Statistical density model

Summary for Lay Audience

Osteoarthritis of the shoulder is a joint disease that can result in severe pain and stiffness. Total shoulder arthroplasty (TSA) is a clinically successful surgery to relieve pain and restore the natural range of motion to the arthritic shoulder joint. The number of patients who undergo TSA has experienced rapid growth, more than any other joint in the human body over the past decades and is continuing to grow. A seven-fold increase in its incidence is predicted for the next decade. During TSA, an implant is inserted into the humerus bone, the bone of the upper arm, to reconstruct the shoulder joint. However, due to altered loading transmission following implantation, the proximal (near the upper end) humerus will be shielded from experiencing stress. Bone is a self-optimizing structure, which means that it adapts its structure according to the exerted loads. Therefore, the reduction of stress in the proximal humerus can lead to bone loss, implant loosening and, finally, a need for revision surgery.

Humeral implants are comprised of two sections, namely, the stem component and the head component. The design of humeral implants and specifically their stem component has a significant influence on the overall implant success, as the stem is responsible for load transfer from the head component of the implant to the surrounding bone.

We found that the use of more compliant shoulder implants with hollow stems could marginally mitigate the effect of stress shielding and consequently reduce the need for revision surgeries of the shoulder. Also, an exacerbation of stress shielding was found for patients suffering from osteoporosis, a bone disease in which deterioration of bone tissue occurs. Our study suggests that further increasing the compliance of implant stems by making them also porous could increase the bone stresses at the proximal humerus and, therefore, further limit the stress shielding.

Co-Authorship Statement

Chapter 1:

Pendar Soltanmohammadi – Performed the literature survey, helped craft project objectives and wrote the manuscript.

Ryan Willing – Edited the manuscript.

Chapter 2:

Pendar Soltanmohammadi – Developed models, performed data analysis and wrote the manuscript.

Vishnu Veeraraghavan and Josie Elwell – Segmented the CT images and generated surface geometries with identical mesh topologies and edited the manuscript.

Derek Jacobs – Assigned nodal density properties to each specimen's volume mesh with an automated code provided by Pendar Soltanmohammadi.

Ryan Willing – Edited the manuscript.

Chapter 3:

Pendar Soltanmohammadi – Developed models, performed data analysis and wrote the manuscript.

Derek Jacobs – Segmented the healthy and osteoporotic CT images.

George Athwal – Supervised the positioning of the implant

Ryan Willing – Edited the manuscript.

Chapter 4:

Pendar Soltanmohammadi – Wrote the manuscript.

Ryan Willing – Edited the manuscript.

Acknowledgments

I would like to thank my supervisor, Dr. Ryan Willing, for his illuminating guidance and enduring inspiration throughout this research project. Also, I take this opportunity to thank my advisory committee members, Dr. Athwal and Dr. Lalone, for their helpful instructions. I appreciate the support of my fellow labmates at the Musculoskeletal Biomechanics Laboratory at Western University. I am also grateful to Derek Jacobs for his assistance in this project.

This work would not have been possible without the never-ending support of my family and friends: Mehdi Soltan Mohammadi, Samaneh Zaferani, Alireza Rezazadeh, Jahanbakhsh Jahanzamin, Alireza Moslemian, Alisaleh Shariati, Amir Tavakoli, Armin Geraili, and Geoffrey Yamomo.

Although words are not capable of expressing my eternal debt of gratitude to my beloved parents and my dear sister, I will take this opportunity to dedicate this thesis to them who have been a continuous source of moral and emotional support.

Table of Contents

Abstract.....	ii
Summary for Lay Audience.....	iii
Co-Authorship Statement.....	iv
Acknowledgments.....	v
Table of Contents.....	vi
List of Tables.....	viii
List of Figures.....	ix
List of Appendices.....	xi
Chapter 1.....	1
1 Introduction.....	1
1.1 Anatomy of the Shoulder.....	2
1.1.1 Osseous Constructs.....	3
1.1.2 Soft Tissue Constructs.....	6
1.2 Structure and Material Properties of Shoulder Bones.....	7
1.2.1 Structure of Bone.....	7
1.2.2 Material Properties of Bone.....	8
1.3 Shoulder Arthroplasty.....	9
1.4 Wolff's Law and Stress Shielding.....	12
1.5 Statistical Shape and Density Modeling.....	14
1.6 Finite Element Simulation of Shoulder Arthroplasty.....	16
1.7 Project Scope and Objectives.....	17
1.8 Thesis Overview.....	18
Chapter 2.....	19
2 Investigating the Effects of Demographics on the Shape and Density of the Shoulder.....	19

2.1	Introduction.....	19
2.2	Methods.....	21
2.2.1	Development of Statistical Shape and Density Models.....	21
2.2.2	Data Analysis.....	25
2.3	Results.....	26
2.4	Discussion.....	37
	Chapter 3.....	42
3	Structural Analysis of Hollow- Versus Solid-stemmed Shoulder Implants of Proximal Humeri with Different Bone Qualities.....	42
3.1	Introduction.....	42
3.2	Methods.....	43
3.3	Results.....	52
3.4	Discussion.....	63
	Chapter 4.....	68
4	Summary and Future Works.....	68
4.1	Summary.....	68
4.2	Limitations and Strengths.....	69
4.3	Future Directions.....	71
4.4	Significance.....	72
	References.....	73
	Appendices.....	86
	Curriculum Vitae.....	92

List of Tables

Table 2.1 The demographic data for male and female sub-groups.....	25
Table 3.1 Number of donors in each category of bone disease conditions along with the cutoff HUs used for classifications	45
Table 3.2 Values of joint reaction forces (N) and frictional moments (N.mm) applied to the reference point along with their resultants during investigated activities.....	49

List of Figures

Figure 1.1 Three common planes used to define anatomy	2
Figure 1.2 Bones and articulations of the shoulder.....	3
Figure 1.3 Bony Landmarks of the humerus	5
Figure 1.4 Bony landmarks of the scapula.....	6
Figure 1.5 The main forms of shoulder reconstruction.....	10
Figure 2.1 Steps taken toward developing SSMs from CT images	21
Figure 2.2 Baseline mesh mapping	22
Figure 2.3 The first two modes of shape variation of the shoulder	27
Figure 2.4 Cumulative sum of the variability percentage explained by the respective number of PCs.....	29
Figure 2.5 The shape of the humerus and scapula averaged over the entire population and averaged over male/female sub-group	30
Figure 2.6 The boxplot of the PC scores of male and female humeri in the well-matched set for shape.....	31
Figure 2.7 The boxplot of the PC scores of male and female scapulae in the well-matched set for shape.....	32
Figure 2.8 The boxplot of the PC scores of male and female humeri in the well-matched set for density	33
Figure 2.9 The Boxplot of the PC scores of male and female scapulae in the well-matched set for density	34
Figure 2.10 Comparing the male with female bone density distribution.....	35

Figure 3.1 Defined slices to measure density in the proximal humerus	44
Figure 3.2 Solid- and hollow-stemmed implants	46
Figure 3.3 Mesh Planning	47
Figure 3.4 Humeral coordinate systems used for the right humeri along with the boundary conditions applied to their distal end	50
Figure 3.5 Outcome measures were quantified regionally for chosen cortical and trabecular bone slices	52
Figure 3.6 The volume-weighted average change in the magnitude of von Mises stress for the reconstructed cortical bone	54
Figure 3.7 The volume-weighted average change in the magnitude of von Mises stress for the reconstructed trabecular bone	55
Figure 3.8 The volume-weighted average deviatoric component of the change in stress tensor for the reconstructed cortical bone.....	57
Figure 3.9 The volume-weighted average deviatoric component of the change in stress tensor for the reconstructed trabecular bone.....	58
Figure 3.10 The percentage of cortical bone volume with the resorption/formation potential for each bone condition and each stem design.....	60
Figure 3.11 The percentage of trabecular bone volume with the resorption/formation potential for each bone condition and each stem design.....	62

List of Appendices

Appendix A. Specimen Reconstruction Using a Compact SSM/SDM	86
Appendix B. SSM Robustness Analysis.....	88
Appendix C. SDM Robustness Analysis	90

Chapter 1

1 Introduction

Total shoulder arthroplasty (TSA) is widely regarded as a clinically successful surgery, relieving pain, and restoring the natural range of motion (ROM) to an arthritic shoulder joint [1]–[3]. It has the most rapid growth among all human joint replacement procedures, with a projected seven-fold increase in its utilization over the next decade [4]. The number of TSA and hemiarthroplasty procedures performed in the United States increased from approximately 19,000 in 2000 [5] to more than 66,000 in 2011 [6]. The increasing number of arthroplasty procedures, along with their increased charges, can impose a financial burden on the health care system [7]. Stress shielding around the stem component of shoulder replacement implants can result in adaptive bone remodeling and bone resorption leading to implant loosening and the need for revision surgeries [8]–[10]. Elderly patients undergoing TSA may suffer from concurrent osteoporosis. Due to the lower rigidity of osteoporotic versus normal bone, there is an exaggerated stiffness difference between the humerus and implant. Thus osteoporosis at the time of implantation is a risk factor [8], [11]–[13].

A better understanding of how the shape and density of the shoulder vary among members of a population can help design more effective population-based orthopedic implants. To reduce needs for revision surgeries, the gained insight can be leveraged toward investigating the ability of more compliant implants in limiting the stress shielding of proximal humerus by performing finite element analyses.

This chapter describes the anatomy of the shoulder, material properties of shoulder bones, stress shielding, and shoulder arthroplasty. Following that statistical shape and density modeling and finite element simulation of shoulder arthroplasty are presented as tools that were used to achieve the objectives of this study reported at the end of this chapter. Finally, the outlines of the following chapters are described.

1.1 Anatomy of the Shoulder

Being an intrinsically complex system, the shoulder is formed by three bones, and three joints that work in conjunction with four articulations and numerous muscle groups, ligaments, and tendons. The main function of this entire arrangement is to ensure stabilization of the shoulder and also create a maximal ROM in sagittal, frontal (coronal) and transverse planes (Figure 1.1) relative to other joints in the body [14]–[16].

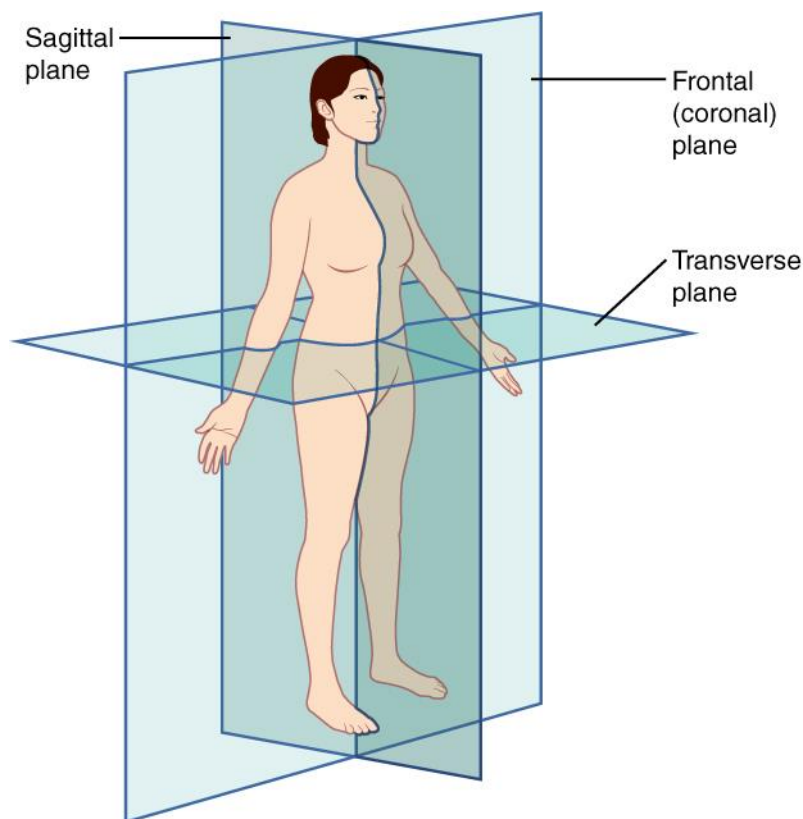


Figure 1.1 Three common planes used to define anatomy [17]

Another way to consider the structure of the shoulder system is by characterizing it via its primary component, namely the glenohumeral joint, which is essentially a shallow ball-and-socket joint made of osseous constructs, muscles and the joint capsule.

1.1.1 Osseous Constructs

The four following articulations are the main constituents of the shoulder: the glenohumeral joint, sternoclavicular joint, acromioclavicular joint, and scapulothoracic joint (Figure 1.2). The bones that are involved in creating these articulations are the humerus, scapula, clavicle, sternum, and ribs. Moreover, the clavicle (collarbone) is also involved in forming the shoulder complex. These articulations act in concert to restrain any unintended movement and allow necessary motion of the shoulder [16]. Located between the humeral head and the glenoid concavity of the scapula, the glenohumeral joint is the major articulation of the shoulder contributing the most to shoulder ROM and the primary articulation of interest in this study.

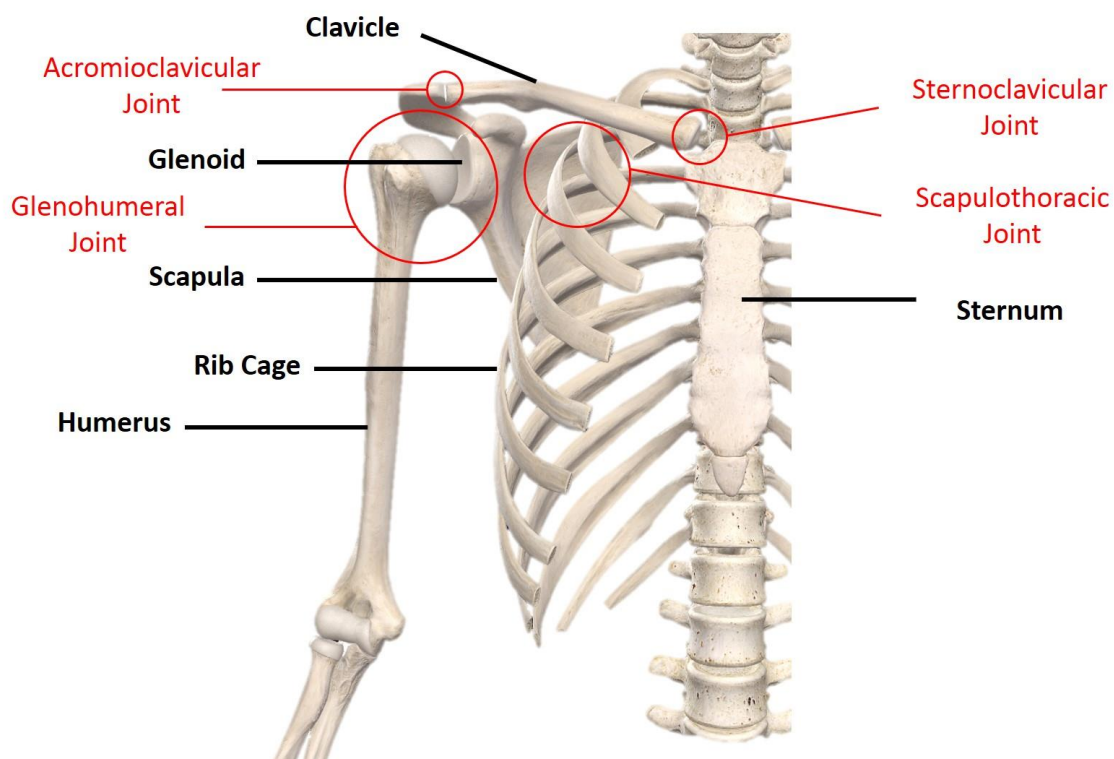


Figure 1.2 Bones and articulations of the shoulder (Image courtesy of Complete Anatomy software, Dublin, Ireland)

1.1.1.1 Joints

The glenohumeral joint is the major articulation of all the joints in the shoulder. Being called the ‘shoulder joint’ in many common usages, it is situated in between the humeral head and the glenoid concavity of the scapula (Figure 1.2). This particular joint has the largest ROM compared to all other joints of the body [18]–[22]. Therefore, in order to conduct any research concerning the shoulder joint or its replacement for that matter, it is imperative to clearly identify and study glenohumeral contact forces. Numerous studies in the literature have done so by investigating the *in vitro* glenohumeral contact forces [23]–[25] or alternatively using either two or three-dimensional musculoskeletal models [26], [27].

Notwithstanding, some inconsistencies arise when one tries to calculate joint reaction forces due to the variety of muscles and consequent indeterminacy. To address this, Bergmann et al. [28] proposed and implemented an *in vivo* method of study that made obtaining more plausible data possible through direct measurements from a telemeterized implant that recorded the glenohumeral contact forces for different activities including shoulder abduction and flexion.

1.1.1.2 Bones

Comprising the glenohumeral joint, the humerus is the most proximal bone of the upper extremity. Its head is situated superior, medial and posterior with respect to the humeral shaft and articulates with the glenoid and is geometrically close to one-third of a sphere (Figure 1.2) [16]. Additionally, the humerus possesses several distinct landmarks: the greater tuberosity (GT), lesser tuberosity (LT), the bicipital groove (between greater and lesser tuberosities), the deltoid tuberosity, and the medial and lateral epicondyles (Figure 1.3). Being in the middle segment of the humeral shaft and on its lateral side, the deltoid tuberosity is the distal insertion location of the deltoid muscle. In addition, the greater tuberosity acts as the nexus of deltoid muscle insertion points on the humerus and its origin located on the acromion of the scapula, enabling the deltoid activity even when the arm is below 45° of glenohumeral abduction [16].

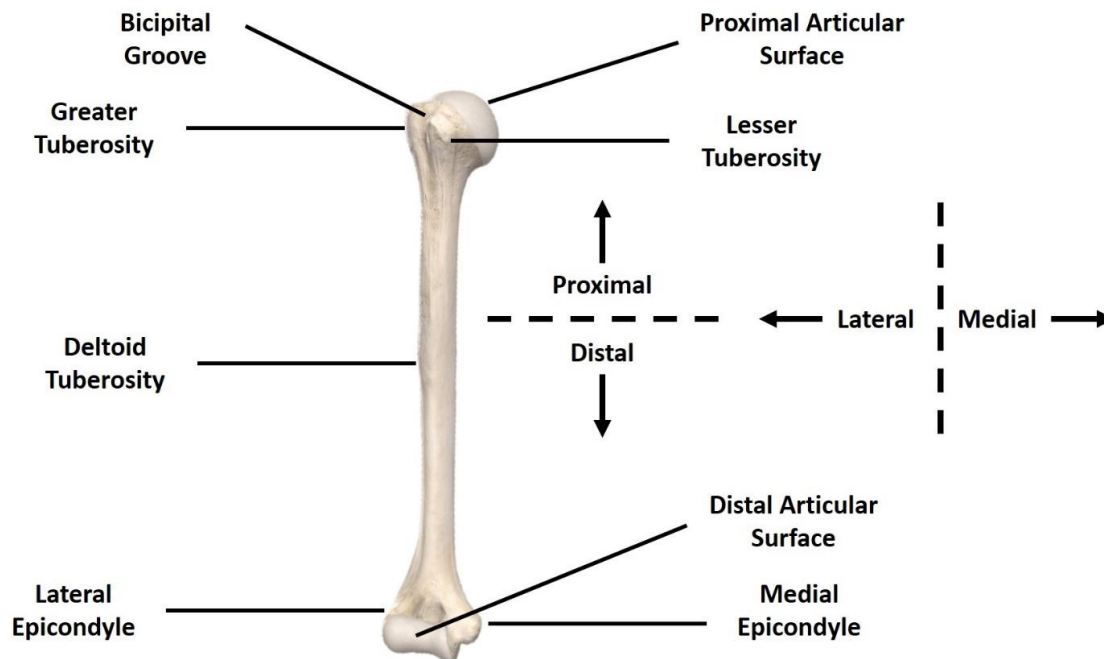


Figure 1.3 Bony Landmarks of the humerus (Image courtesy of Complete Anatomy software, Dublin, Ireland)

Another yet essential part of the shoulder joint, the scapula, is the triangular bone located in the shoulder connecting the upper limb to the thorax and is also partly responsible for the motion of the upper limb by being the origin for multiple muscles (Figure 1.4) [16]. Several bone projections such as the spine, acromion, and coracoid process emanate from this bone.

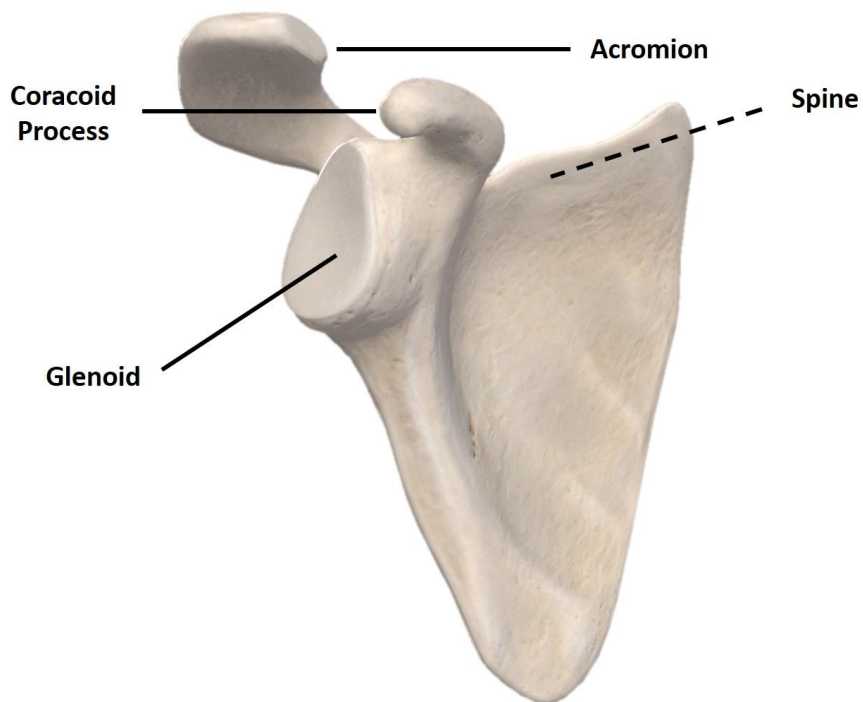


Figure 1.4 Bony landmarks of the scapula (The spine is located on the posterior side)

(Image courtesy of Complete Anatomy software, Dublin, Ireland)

These projections have variegated functions inside the shoulder. For instance, middle and anterior deltoid and the trapezius muscles all originate from the acromion [16], while the trapezius and the posterior deltoid muscles intersect at the scapular spine process.

Moreover, the scapula participates in the shoulder's ROM through its gliding over the ribcage, creating a 2:3 ratio of glenohumeral abduction/flexion angle to gross shoulder abduction/flexion angle for most of its ROM [29], [30].

1.1.2 Soft Tissue Constructs

Many muscles surrounding the shoulder play a role in shoulder stabilization and movement. It is possible to divide such muscles into three distinct categories as follows:

1. Axiohumeral muscles
2. The scapulohumeral muscles
3. The axioscapular muscles

The axiohumeral and axioscapular muscles emanate from the thoracic cage, but the axiohumeral muscles insert on the humerus and axioscapular ones insert on the scapula. Latissimus dorsi and pectoralis major muscles comprise the axiohumeral muscles while the serratus anterior, the levator scapulae, the trapezius, the pectoralis minor, and the rhomboids all form the axioscapular muscles. The function of this muscle group is to facilitate scapula motion. On the other hand, the scapulohumeral muscles, the muscle group that emerges from the scapula toward the humerus, are composed of the deltoid, teres major, teres minor, supraspinatus, subscapularis, infraspinatus, and coracobrachialis.

The deltoid muscle, which is responsible for humerus abduction by generating about half of the elevation moment, is itself separated into three major parts, namely the anterior, middle and posterior sections [31], with more contribution from the first two sections [16]. The posterior deltoid is involved in the external rotation and extension of the humerus, while the anterior deltoid contribution is more involved with internal rotation and flexion of the humerus [32].

The last relevant muscle group is the rotator cuff, attached to the greater tuberosity of the humerus, and is made up of the joint capsule, the ligaments, the teres minor, subscapularis, supraspinatus, and infraspinatus muscles and the tendons surrounding the glenohumeral joint.

1.2 Structure and Material Properties of Shoulder Bones

1.2.1 Structure of Bone

Considered a composite material, bone consists of mineral substances and organic matter with a 2:1 ratio, respectively. Working in concert, these two components bring about the required strength and resilience for the bone. The mineral component makes a greater contribution to the bone strength and resists compressive stress while the collagenous organic component assists in resisting tensile stress and providing viscoelasticity to the bone [33]–[35].

The bone is mainly responsible for bearing the body's mass and the stresses applied to it. To that end, the bone rearranges and restructures itself [36], [37]. This response is, in fact,

a constant destructuring and restructuring cycle attributed to osteoclasts and osteoblasts, which are responsible for bone tissue resorption and formation, in that order [38], [39].

Viewed at a macroscopic scale, the structural components of long bones, which constitute the appendicular (i.e., arm, leg, etc.) skeleton, are divided into three sections: the diaphysis (shaft), epiphysis (where the articulation is located), and metaphysis (between epiphysis and diaphysis) [40]. Also, bones can be categorized as either cortical (compact) or as trabecular (cancellous). Cortical bone is a relatively more homogenous and denser structure when juxtaposed with cancellous bone. The epiphysis is, in essence, a cancellous bone within a cortical shell, while diaphysis is a cortical shell with an inner medullary cavity, a hollow canal containing the bone marrow. A porous, heterogenous and varying structure in its entire volume, cancellous bone can contribute to local anatomic functions [34], [35], [40]. Due to osteoporosis, which is a common bone illness, especially for aged populations, the porosity of cortical and trabecular bone increases and, subsequently, the load-bearing capability of the bone is reduced [41].

In the microscopic realm, the extended bone columns parallel to diaphysis called Osteons constitute the cortical bone. On the contrary, the cancellous bone is made of trabeculae, a set of extremely organized, dense, and aligned isolated struts of tissue. The orientation of the trabeculae is so that they are positioned in line with the stresses applied to them [34].

1.2.2 Material Properties of Bone

Obtaining Young's modulus, or associated stiffness is an integral part of the quantitative analysis of bone elastic properties. Estimating the stiffness of bone is a complicated task due to its heterogeneity, especially for trabecular bone. To address this, sophisticated medical image processing methods are utilized to locally obtain the material properties of bone in small regions termed voxels. In particular, computed tomography (CT) images can provide x-ray attenuation data measured in Hounsfield units (HU). Then, based on a quantitative relationship derived from bone calibration data, the apparent density (defined as wet bone mass over total volume) of a specific region of bone can be obtained [42].

The Young's modulus can be estimated using the measured bone density. Numerous studies have proposed equations relating Young's modulus to bone density [43]–[47]. These equations mostly take into consideration both cortical and trabecular bones. However, Morgan et al. [48] proposed a formula that yields Young's modulus of trabecular bone at various sites in the body utilizing an *in vitro* technique. Similarly, Austman et al. [43] derived a relationship that correlates apparent bone density to Young's modulus for the cortical bone of the ulna. As was suggested by Zannoni et al. [42], by ascribing varying Young's modulus obtained from the CT scan HU data to each element of a mesh, the heterogeneous properties of the bone can be approximated.

1.3 Shoulder Arthroplasty

The first-ever recorded instance of a shoulder replacement occurred in the early 1890s and was successfully used towards treating fractures in proximal humerus while recovering normal ROM of the shoulder and alleviating the associated pain [49]. In the 1970s, Neer [50] expanded the domain of the usage of this method to treat a condition that severely limits the optimal functioning of the shoulder, known as glenohumeral arthritis, which can have many causes such as congenital, traumatic, vascular or septic factors, among others [16], [50]. For addressing severe arthritis of the glenohumeral joint or fractures involving the proximal humerus, shoulder arthroplasty is still the method of choice. Treatment options include partial surface reconstruction, hemiarthroplasty, total shoulder arthroplasty (TSA), and reverse total shoulder arthroplasty (RTSA) (Figure 1.5).

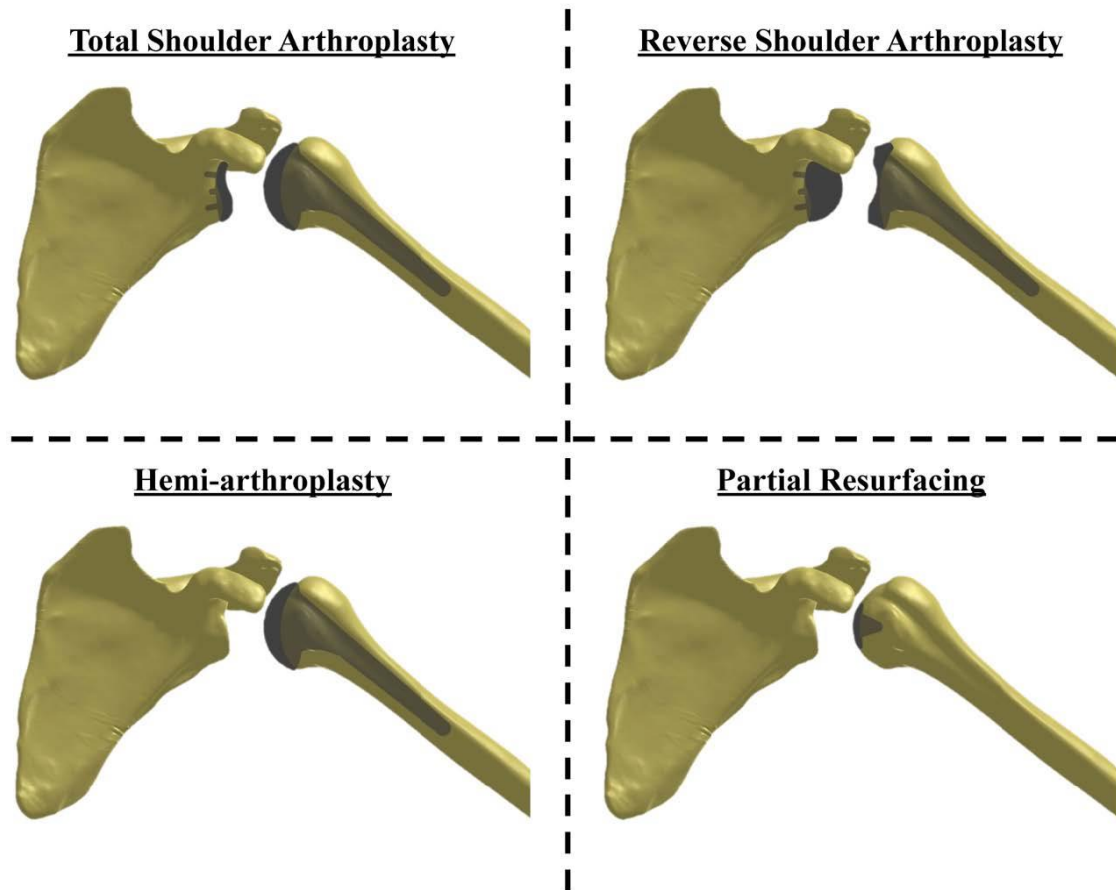


Figure 1.5 The main forms of shoulder reconstruction [51]

During TSA and RTSA, complete (two-sided) replacement of the glenohumeral joint with a prosthesis is required [52].

Typically, a prosthesis designed for shoulder replacement can be divided into three sections, namely, a humeral head, glenoid structure, and the implant stem. In the hemiarthroplasty method, one-sided replacement of the humeral side of the joint with a humeral head and an implant stem occurs, while in partial resurfacing, one of the joint surfaces is replaced and native bone is mainly left intact [52].

Numerous breakthroughs have been made in implant design, materials used and methods related to stabilizing and sterilization of prostheses as well as surgical procedures followed since the introduction of the first shoulder prostheses [53], [54].

More recently, modified implant designs have been proposed that are characterized by either a reduced humeral stem length or having removed them completely. Usage of these shorter versions of implant stems is becoming more commonplace because of the reduction in broaching and reaming of the humeral canal they provide. This, in turn, results in higher preservation of the original native bone while reducing the stress exerted on the cortical bone and also rendering perioperative periprosthetic fracture less likely. As suggested by various studies in the literature, reducing the length of the humeral stems is responsible for the decrease in stress shielding by maintaining a larger portion of the original native bone [54]–[57].

In order to fix the implant into the host bone and link the bone and prosthetic structures together permanently, two main methods, namely, cemented and press-fit are currently being employed. Based on the selection of fixation type, various surface textures such as plasma spray, trabecular metal, grit blast or smooth polished may be used on the implant for improving the biological reaction of the shoulder to the prosthesis [58]. More recently, uncemented types are being preferred due to their longer stability caused by the conservation of a greater portion of the native bone in this technique [59], [60].

Although shoulder implant design has made enormous progress, there are still some challenges that need to be addressed. For instance, implant loosening, proximal bone loss, fractures happening during or after the surgery, and stress shielding are obstacles that still exist and are yet to be overcome [56], [61].

A study by Denard et al. [62] posits that while short stem implants generate less osteolysis compared to regular stems, a significant portion of them, around 20 percent, still cause cortical thinning of the lateral proximal metaphysis and half of them caused cortical thinning of the medial metaphysis. The same study observes an additional 23% partial calcar bone resorption in short stem models. Furthermore, once implanted, 86% of the short stem models were anatomically aligned compared to 98% of regular stems. This increased misalignment, in turn, can compromise shoulder functionality by causing stiffness in the joints or pain [63]. The occurrence of cortical thinning in the medial calcar was also

reported by Schnetzke et al. [64], and a rate of 83% of various forms of bone loss was recorded using a sample study group of 52 short stem models.

Both Casagrande et al. [65], and Morwood et al. [66] indicate a list of problems associated with using short stem models including an 8% revision rate due to humeral loosening in patients, at least one humeral radiolucency in 71% of the implants, partial or complete osteolysis on the medial calcar in 18% of the patients and radiolucencies in 21% of short stem models.

Razfar et al. [67] also observed that although making use of short stem implants reduced the average stress in cortical bone, trabecular bone stresses were elevated relative to the standard stems.

Over 66,000 shoulder replacements are performed annually in the United States [6] and over 4,000 annual shoulder replacements are performed in Canada [68]. Therefore, it is of utmost importance to maintain the long term stability of the implant so as to retrieve normal shoulder joint function and also preclude the occurrence of humeral revision because of the established correlation between humeral revision and periprosthetic fractures, metaphyseal bone loss and other complications [56].

1.4 Wolff's Law and Stress Shielding

When an applied load on a specific portion of bone passes or drops below a certain threshold, bone's reaction includes resorption and remodeling itself. This effect, known as Wolff's law, plays an important role in reconstructed joints as the implant stem or its keel partially bear some of the load applied to the bone [36]. Consequently, the original bone stimulus is reduced and what is known as stress shielding occurs. This phenomenon, in turn, can lead to bone resorption or implant loosening [69]–[71]. Nagels et al. [8] recorded the occurrence of stress shielding in the vicinity of humeral implants in 9% of their sample cases, which comprised of 70 implants. However, when restricted attention to cortical bone, they estimated that the actual development of stress shielding around the shoulder implants to be higher. Several other studies have also reported resorption of the bone near humeral implant stems [9], [10], [72].

Huiskes et al. [37] proposed a strain energy density-based method for bone adaptation and characterized internal bone morphology by the apparent bone density. They stated that when the strain energy density (SED) goes above a specific threshold, the bone density will increase while the bone density will decrease when SED goes below the threshold. They proposed that the rate of bone adaptation is proportional to the amount of increase/decrease of SED beyond the threshold. This energy is, in essence, the internal work (strain energy) balancing the external work done by the externally applied force on an object. SED can be computed using Equation 1.1

$$SED = \frac{\sigma^2}{2E} \quad (\text{Equation 1.1})$$

If the object of interest is linear isotropic that bears small strains, SED can be obtained via Equation 1.2

$$SED = \frac{1}{2} (\sigma_x \varepsilon_x + \sigma_y \varepsilon_y + \sigma_z \varepsilon_z + 2\sigma_{xy} \varepsilon_{xy} + 2\sigma_{yz} \varepsilon_{yz} + 2\sigma_{xz} \varepsilon_{xz}) \quad (\text{Equation 1.2})$$

Where σ and ε show the components of stress and strain tensors, respectively.

Bone adaptations have shown to be well correlated with changes in SED [73], [74]. By comparing two different techniques of SED-based bone remodeling and compliance-based structural topology optimization from a mathematical formulation perspective, Jang et al. [75] showed that the SED-based bone remodeling technique could be mathematically formulated as a compliance-based structural topology optimization problem. In structural topology optimization material is mapped in a design domain systematically and iteratively such that an optimal structure can be achieved, minimizing a predefined objective function. It is possible to obtain an accurate prediction of the density distribution of the bone in response to external loads by using iterative computer models based on SED measurements, and thus estimate the response of the bone to arthroplasty [37], [73], [76], [77]. Neuert et al. [73] modeled human ulna from micro computed-tomography (μ CT) data using the SED-based bone remodeling technique. They considered an initial uniform density distribution for the bone and exerted loads based on *in vivo* data. Different threshold values for the occurrence of bone remodeling were tested, and the resulting steady-state

density distribution was contrasted with μ CT data. The optimal model parameters were then utilized to model six additional human ulnae. They found that the SED threshold as a variance of 55% from the bone's natural SED, results in the smallest error between estimated and physiological density values. Moreover, Reeves et al. [78] used an SED-based bone remodeling algorithm to predict humeral bone initial response to shoulder arthroplasty.

1.5 Statistical Shape and Density Modeling

The enormous variability in anatomical and biomechanical characteristics of biological structures such as material properties, joint kinematics and dynamics, and geometry can be challenging from a medical device design or surgical planning point of view [79].

By using statistical shape models (SSM), and statistical shape and density models (SSDM), the morphological and mechanical variability can be quantitatively analyzed respectively via attaining the average bone shape and average bone density and their main variation modes within a population. Certainly, the accuracy of the predictions of the variation among subjects resulting from any model is contingent upon the selected sample size and the explanatory power of it in terms of representing the population. One advantage of the SSM method is the fact that it can determine the variability in anatomical features of a subpopulation that share the same background [80]. Examples of such subpopulations are individuals with osteoporotic or osteoarthritic conditions or those who share common sex or ethnicity. This feature can allow medical specialists and clinicians to more accurately diagnose diseases and plan the treatment or surgical procedures required and also assist engineers in the design process of medical equipment.

In practice, while it is ideal to have models specifically designed for each individual to address personalized medical needs, time and financial constraints always exist. SSM is capable of decreasing the instances where such costly models are required or at a minimum, render their design less expensive by reducing computational time. As such, SSM has been in use as a predictive tool. For instance, it can be employed to predict the shape of the shoulder joint from adjacent segments [81]. Additionally, as an example, SSM has applications in the knee joint where it is utilized to obtain multiple anatomical variables,

including contact mechanics and kinematics, by analyzing joint shape on patellofemoral and tibiofemoral sides [82], [83].

Numerous studies suggest an alternative usage for SSM, which involves reconstruction of the 3D geometry of bones and cartilages by an automated segmentation of CT or magnetic resonance images eliminating inter- and intra-observer errors [84]–[86].

Until now, much attention has been given to SSM in the literature in different bones throughout the body. Instances of such studies include the humerus [87] or pelvis [88]. They have also been applied to human joints, including the shoulder [81], [89], knee [82], [83], [85], and the spine [90]. However, SSDM has been often neglected in comparison, and only a few studies have used this tool [91]–[93]. Even among these, the common theme is their confined focus on the femur. In order to procure an SSDM of a bone, the mainstream technique in practice is to derive the apparent bone density from CT image values [94] and use the obtained results to subsequently estimate the Young's modulus through a set of experimental formulae as found in studies such as [48], [95]. Design and size determinations of medical devices can be addressed by SSM for any population or subpopulation having similar morphological traits [96], while SSDM can help test these designs due to their ability to create population-based finite element (FE) models of the bone structures along with their associated material distribution. In orthopedics and other medical fields, such finite element models are becoming more commonplace before introducing medical products into the market. FE analyses can be used to predict the distribution of stress or fatigue life in the implanted bone [97], which in turn reduces the associated costs and time needed for *in vivo* or *in vitro* experiments. Furthermore, the effect of implants on the biomechanics of the joint can be estimated using the SSDM, a task that is quite challenging in experiments, especially in measuring muscles, ligaments or internal contact forces [85], [98], [99]. Finally, the intricate and tedious process of the construction of FE models can be greatly shortened by utilizing the SSDM of the bone, rendering this method an increasingly popular option in the manufacturing of medical devices [90].

Both SSM and SSDM can be considered as versatile and powerful platforms that allow a probabilistic analysis of desired populations that enable an in-depth insight on anatomical

variability of the bones by taking into account an entire spectrum of probable outcomes through expanding the original training set. The size of the training set at hand is directly correlated with the amount of anatomical variation SSM and SSDM can explain within a population. For this purpose, a principal component analysis initiates SSM and SSDM to avoid the difficulties accompanying identifying main independent variation modes in large data sets. This statistical procedure diminishes the original data set at hand in terms of its dimension while maintaining the same level of variation contained in it [100].

1.6 Finite Element Simulation of Shoulder Arthroplasty

Joint forces, movements, and anatomy are increasingly being simulated by the FE analysis method, a subcategory of *in silico* techniques. The FE approach is, in essence, the discretization of a solid continuum into a finite number of smaller elements that are joined together at nodes. This unit consisting of nodes and elements, constitutes what is known as a mesh. The method then proceeds to predict the characteristics of the entire system using localized data. In particular, the applied load, material properties of the system investigated and boundary conditions determine the displacements at each individual node. To further facilitate the incorporation of the variability present in these factors, the values of these parameters can be adjusted for each specific mesh.

On the contrary, more expensive and time-consuming *in vitro* experiments are only useful for localized and isolated analyses, and their predictions cannot be extrapolated accurately to other parts of the bone.

The selection of mesh size is an essential phase of any FE analysis as the accuracy of the FE technique hinges upon mesh resolution, which in itself is a function of the mesh size. However, a trade-off exists between the accuracy of the results, which increases with the number of elements and the computational load associated with the higher number of equations needed. Therefore, an optimal number of elements would be small enough to provide adequate accuracy while not being severely time-consuming for the computation devices. The process that enables the determination of this optimal mesh size is known as convergence analysis.

First- and second-order tetrahedral/hexahedral elements can be used to generate FE volume meshes. In the case of curved boundary zones, second-order (quadratic) elements perform more favorably compared to first-order (linear) ones. Some studies present in the literature indicate that the second-order tetrahedral mesh configuration provides more accurate estimates [101], [102].

Following the discretization step and generation of the meshes, modeling parameters such as load characteristics, element material properties, and boundary conditions are inserted into the model. After that, the displacements attributed to each individual node can be provided by an FE analysis software suite, such as ABAQUS 2018 (Dassault Systèmes, Johnston, RI, USA), which was utilized in this study. Finally, all recorded stresses, strains and other relevant data can be rendered for interpretations. Advanced FE software empowers the researchers in the field of biomechanics, tasked with implant design, to test numerous design configurations by adjusting design factors such as bone geometry, implant design, material properties and loading conditions [103], [104].

1.7 Project Scope and Objectives

This study aims to contribute to enhancing the performance of shoulder replacement implants by firstly providing a better understanding of how shoulder's shapes and densities vary among members of a population by utilizing statistical shape and density modeling. Secondly, the gained insight was leveraged toward investigating the ability of hollow stemmed-implants in limiting the stress shielding of proximal humerus by performing finite element analysis.

Therefore, the objectives of this study are as follows:

1. To develop a statistical shape model and a statistical density model for the shoulder, and to correlate main modes of its shape and density variation with available demographic data; specifically, sex and age.
2. To determine if hollow titanium stems can mitigate stress shielding in comparison with solid stems at the proximal humerus for a variety of bone qualities using finite element methods.

1.8 Thesis Overview

Chapter 2 describes steps taken toward developing our statistical shape and density models and correlations found between the main modes of shape and density variations and demographic data such as age and sex. Also, the symmetry of contralateral shoulders in terms of shape and density are discussed. Chapter 3 examines the implications of using hollow-stemmed implants on changes in the stress distribution of bone and percentage of bone volume with resorption/formation potential following bone reconstruction. Chapter 4 summarizes the findings of chapters 2 and 3, mentions the strength and limitations of this work and outlines future directions. Supplementary information regarding chapter 2 can be found in the Appendix.

Chapter 2

2 Investigating the Effects of Demographics on the Shape and Density of the Shoulder

This chapter describes steps taken toward developing our statistical shape and density models and correlations found between the main modes of shape and density variations and demographic data such as age and sex. Also, the symmetry of contralateral shoulders in terms of shape and density are discussed.

2.1 Introduction

Total shoulder arthroplasty (TSA) is widely regarded as a clinically successful surgery used to relieve pain or restore movement to an arthritic shoulder joint [1]–[3]. This has led to a significant increase in its utilization over the past several decades [5], [105]–[107]. The number of TSA and hemiarthroplasty procedures performed in the United States increased from approximately 19,000 in 2000 [5] to more than 66,000 in 2011 [6]. The increasing number of arthroplasty procedures, along with their increased charges, can impose a financial burden on the health care system [7]. The most technically complicated class of shoulder arthroplasty is the revision of a failed TSA, as various factors can lead to failure [108]. As the number of TSA procedures increases, the need for revision surgeries also rises [109]. In the United States, the revision burden for upper extremity arthroplasty increased from 4.5% in 1993 to approximately 7% in 2007 [7]. Also, the revision rates for TSA grew by 29% between 2006 and 2010 in France, while this rate was 10% for knee and 1% for hip implants in an identical period [110]. Poor bone quality around the implants, or sub-optimal load transfer between implant components and surrounding bone, may affect long-term fixation and ultimately lead to implant loosening and the need for revision surgeries [108], [111].

Therefore, a better understanding of the normal and pathological bone shape and density distribution in the proximal humerus and glenoid may help design implants with improved bone-implant mechanics. Furthermore, tailoring implant shape/stiffness to match specific patient sub-populations may result in a more suitable selection of implant shapes than a one-design-fits-all approach. Thus, finding possible correlations between the main modes

of variation in the shape and density distribution of the shoulder in a population and the demographics of that population would be beneficial.

SSM [112], and SDM [113] are tools capable of describing the shape and complex density distribution of bones in terms of a relatively small set of uncorrelated variables called principal components (PCs). PCs can describe the main modes along which the shape and the spatial distribution of bone density can vary among the members of a population with respect to the average shape and the average density distribution of that set. Describing the shape and density distribution of a given bone by a small set of principal component weighting factors, rather than using physical descriptors, can be more accurate and efficient. Previously, SSMs have successfully been applied to describe the main modes of variation in the shape of different organs such as the liver [114], [115], heart [116], [117], and brain [118], [119]. Examples of bones and joints include the femur [120], hip [121], [122] and knee joint [123]. Furthermore, SDMs have been applied to the femur [91], [93], [113] and the mandibular condyle [124]. At the shoulder, there has been recent progress in applying SSMs to characterize the variability of shapes at the shoulder joint [89], [125]; however, despite its importance for understanding the mechanics of bone-implant load transfer, neither of these works considered the variability in the density distribution of the shoulder.

Therefore, the objective of this study is to develop an SSM and an SDM for the shoulder, and to correlate shape and density PC scores with available demographic data; specifically, sex and age. We hypothesize that the main mode of shape variation in our SSM will be a scaling factor related to the size of the bones. To that end, we theorize that males, on average, have larger humeri and scapulae than females; however, well-matched individuals by weight, height, BMI and age of a different sex will have similar size bones. Moreover, the first PC of the SDMs will likely scale the density over the entire bone, and we anticipate that this PC will be inversely correlated with age (due to natural bone density loss with age) and will, on average, be greater for males than females. Finally, because we are creating separate SSMs and SDMs for each of the humerus and scapula based on one population, we also hypothesize that there will be correlations between several PCs of shape and density.

2.2 Methods

2.2.1 Development of Statistical Shape and Density Models

Specimens

Separate SSMs and SDMs were created for the humerus and scapula using available computed tomography (CT) scans of 75 human cadaveric shoulder joints. This set includes 57 male (20 pairs) and 18 female shoulders (1 pair) from 54 donors, with ages ranging between 21 and 94 years (mean 73 ± 13). Heights ranged from 147 to 191 centimeters (mean 173 ± 10), and weights ranged from 30 to 116 kilograms (mean 65 ± 18). Thus, the shoulders in the set represented large anatomical and size variability with two donors were noted to have osteoarthritis and one to have osteopenia.

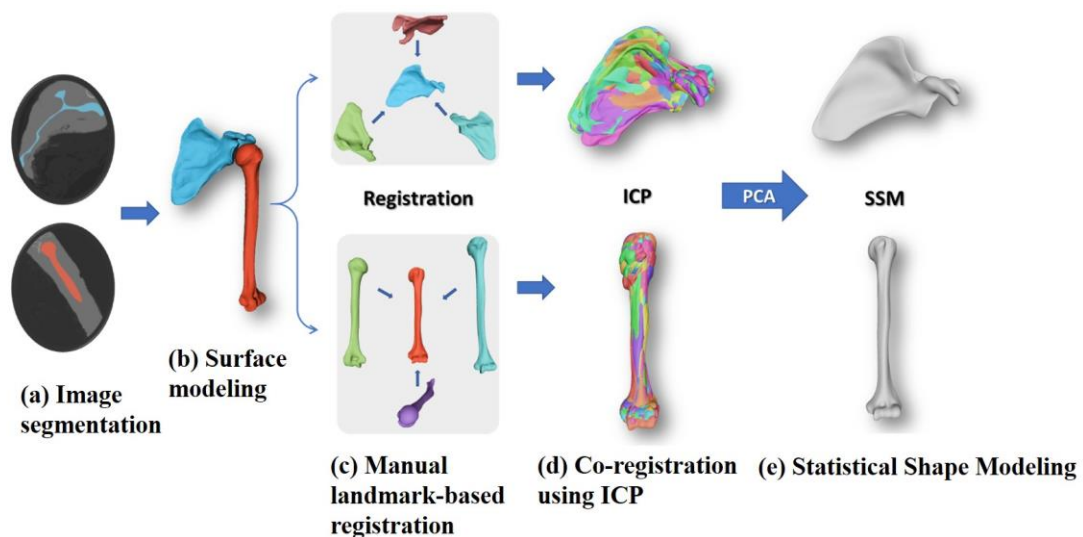


Figure 2.1 Steps taken toward developing SSMs from CT images

Three-Dimensional Model Reconstruction

Surface geometries of each scapula and humerus were segmented from CT scan data using the 3D medical image processing software 3DSlicer [126] (Figure 2.1(a)). A threshold-based segmentation protocol, based on previously described techniques, was employed for each CT scan to label, reconstruct, smooth, and create triangle-tessellated models of each bone (Figure 2.1(b)) [127]. The procedure was repeated for all the subjects for both scapula

and humerus bones, and triangular meshes were extracted for all the segmented 3D models. Right-side scapulae and humeri data were reflected to be left-sided, to simplify the development of the SSMs.

Co-registration and surface mapping

Further data processing was performed in MeshLab [128]. A baseline shape was chosen at random for each of the scapula and humerus, after which they were re-meshed to obtain a smooth and uniform topology with a mean edge-length of 0.6 mm. This resulted in meshes with about 110,000 vertices and 230,000 faces for scapula and about 90,000 vertices and 170,000 faces for the humerus. The 3D meshes of the remaining scapulae and humeri were imported separately into MeshLab and aligned to the baseline shapes. Registration was performed in two steps, first manually using defined homologous points (Figure 2.1(c)) and then refined using an iterative closest point algorithm (Figure 2.1(d)). The two baseline meshes were then mapped/morphed to each of the segmented and aligned meshes in the scapulae, and humeri model sets using R3DS Wrap 3.2 (R3DS, Voronezh, Russia). This process resulted in a mesh for each specimen with similar topology and identical vertex numbering but customized to the individual shape of each specimen (Figure 2.2). Having the same topology simplified point-to-point comparison between the models.

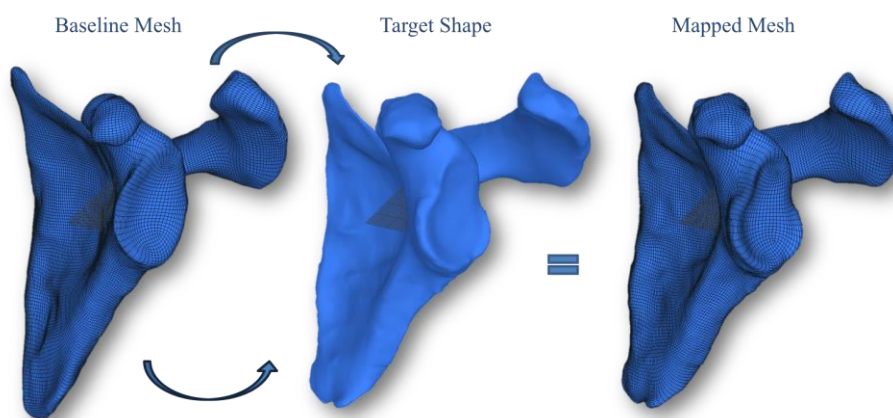


Figure 2.2 Baseline mesh mapping (It was mapped to each of the aligned meshes to obtain the same topology)

Creating homologous volumetric meshes

Just as the humerus and scapula SSMs required a baseline surface mesh that could be mapped or morphed to the shape of each individual specimen, the SDMs required a baseline volumetric mesh, which could be fit into the individual surface mesh of each specimen. This was achieved by first creating baseline humerus and scapula tetrahedral element meshes in TetGen [129] from the same baseline specimen as in the SSMs. These meshes used elements with mean edge-lengths of 0.7 mm, resulting in about 810,000 nodes / 4,800,000 elements for the humerus and about 460,000 nodes / 2,500,000 elements for the scapula base meshes. These meshes were morphed to individual specimens by leveraging the fact that identical surface mesh topologies already existed; thus, displacements, applied directly to the surface nodes of the baseline model, could be used to match the surface to any candidate model, and these displacements were distributed throughout the inner volumetric mesh accordingly via the element shape functions and mesh connectivity. This process resulted in a set of 75 corresponding shoulder mesh models.

Assigning nodal density properties

Each humerus and scapula mesh was then transformed back into its original CT coordinates and imported into the open-source mesh pre-processing software MITK-GEM [130], along with the corresponding CT data set. Using this software, the CT image intensity (in HU) at each node location in the volume mesh could be computed from the CT data. As a result, a set of 75 humerus and scapula 3D meshes, with homologous mesh topologies, each had specimen-specific CT image intensity data assigned at each node. Due to the homologous mesh topologies, the CT image intensity of any given node within a model could be compared directly with the CT image intensity of the same node (at the same *relative* position) within any other model.

Principal Component Analysis

The vertex coordinate data for all specimen models were imported into MATLAB R2017b (Mathworks Inc., Natick, MA, USA) as point clouds, where the coordinates for all n vertices were concatenated to one vector \mathbb{X} that described the shape, i.e., $\mathbb{X} =$

$(x_1, y_1, z_1, \dots, x_n, y_n, z_n)$. Each vector represented the point coordinates for a single specimen, and all were assembled into a single matrix (but a separate matrix for the humerus and scapula coordinate data). Principal component analyses (PCAs) were performed separately for the assembled humerus and scapula coordinate matrices to identify principal components (PCs) of the shape for the humerus and scapula. These PCs described the main modes of shape variation within each set most efficiently and were used to find the average shape of the bones (Figure 2.1(e)).

In a similar manner, PCA was also performed on the spatial distribution of bones' densities to identify main modes of density variation within each set of the humeri and scapulae separately.

Defining positive direction of PCs

In order to have a consistent definition for the positive direction of each individual PC of the SSMs, all the specimens were sorted based on their volume in ascending order and evenly split into two groups (high volume and low volume). The positive direction of each PC was defined such that the corresponding PC score of the high-volume group would be greater (more positive) than the corresponding PC score of the low-volume group.

Similarly, to establish a consistent direction of each individual PC of the SDMs, specimens were sorted based on their average density over their entire volume in an ascending order, divided into two equal groups (high density and low density), and the positive directions of PCs were defined such that the high-density group had a higher average PC score (more positive) than the low-density group.

Evaluating compactness and robustness of statistical models

A primary objective of statistical models (and PCA in general) is to use a compact set of parameters (fewer parameters) to describe variability in a set. To evaluate the compactness of models, the percentage of variability between meshes in the set explained by each PC was calculated for SSMs and SDMs for each of the humerus and scapula. Furthermore, for each specimen, the error in reconstructing the shape and density distribution of the humerus and scapula using a compact SSM/SDM was evaluated (Appendix A).

The robustness of the SSMs (Appendix B) and SDMs (Appendix C) against the particular specimens used in the study was also assessed.

2.2.2 Data Analysis

The shape and density of the humerus and scapula, as described using principal components, were compared for males versus females. To reduce the bias of the larger average male subject sizes, a more comparable sub-group of males and females in the height range of 157 to 170 centimeters was chosen, which included 7 male and 11 female donors. The age, height, weight and BMI of these donor sets were not significantly different (Table 2.1).

Table 2.1 The demographic data for male and female sub-groups

	Male	Female	P
Age (years)	79 ± 9	73 ± 10	0.24
Height (centimeters)	166.1 ± 3.6	163.3 ± 4.3	0.19
Weight (kilograms)	55.2 ± 10.3	51.5 ± 7.8	0.46
BMI	20 ± 3	19 ± 3	0.54

To test the hypothesis that the shapes of the humeri and scapulae from well-matched male and female donor subsets were the same, student's *t*-tests were used to compare the shape and density PC scores of the humeri/scapulae of the well-matched male versus female subsets (excluding contralateral bones) and statistically significant differences were determined ($p \leq 0.05$). To test the hypothesis that bone density will decrease with age, Pearson correlation coefficients were calculated for age and PC scores of all the specimens in the SDM (excluding contralateral bones).

Furthermore, since contralateral specimens were included in the study set, shape and density PC scores of another sub-group containing 21 pairs of contralateral humeri and scapulae were analyzed using paired *t*-tests in order to identify asymmetry in bone shapes or densities. As information regarding the dominant hand of the donors was not available, we compared the right versus left shoulders. Finally, correlation coefficients between PCs

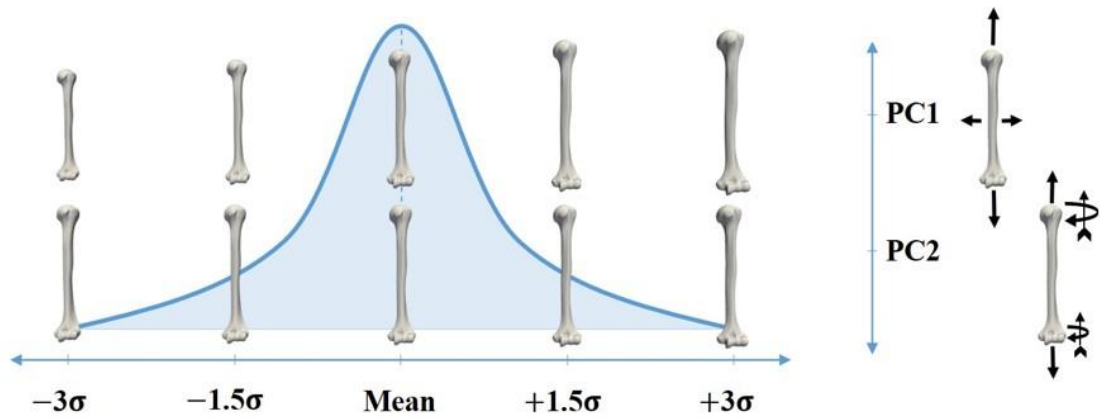
of the SSM and PCs of the SDM were calculated for each of the humerus and scapula separately. Each statistical analysis using SSM/SDM data only included the first few principal components, as determined by the results of compactness analysis.

2.3 Results

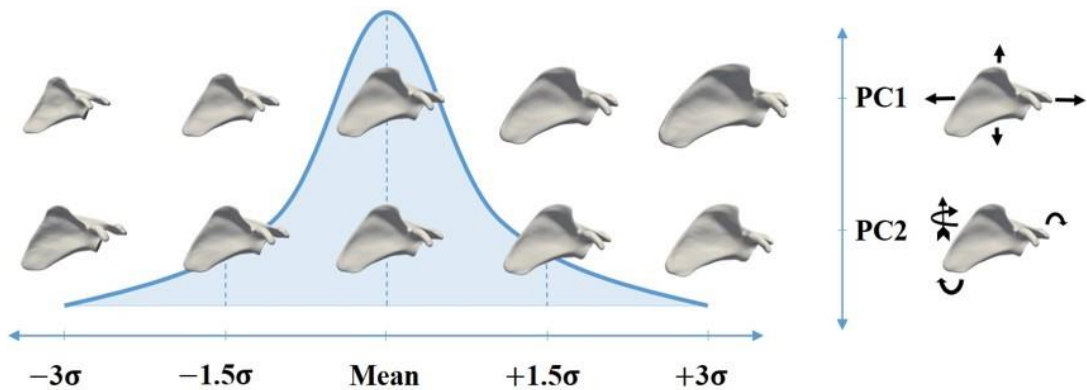
Main Modes of Shape and Density Variations

For the SSMs, the first mode of shape variation, as predicted, was a scaling factor in the model set and the second mode correlated to the orientation of the bones as shown by the arrows (Figure 2.3).

For the SDMs, the first mode of density variation scaled the density over the entire bone while the second mode described a thinning of the cortical shell.



(a) Humerus



(b) Scapula

Figure 2.3 The first two modes of shape variation of the shoulder; (a) for the humerus, (b) for the scapula (Arrows with a vane at the end show the directions of out-of-plane rotations)

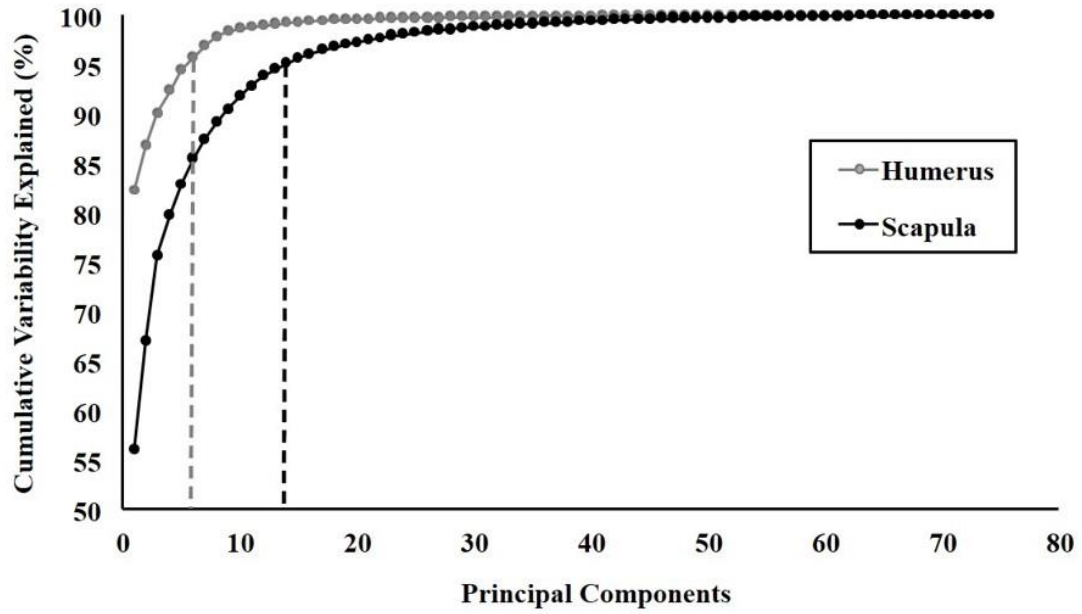
SSM and SDM compactness

Using the SSMs, the highly correlated nodal coordinates of the shapes were reduced into a relatively small set of 74 uncorrelated and independent shape variables (SSM PCs). Similarly, using the SDMs, the highly correlated nodal density variables were reduced into 74 uncorrelated SDM PCs.

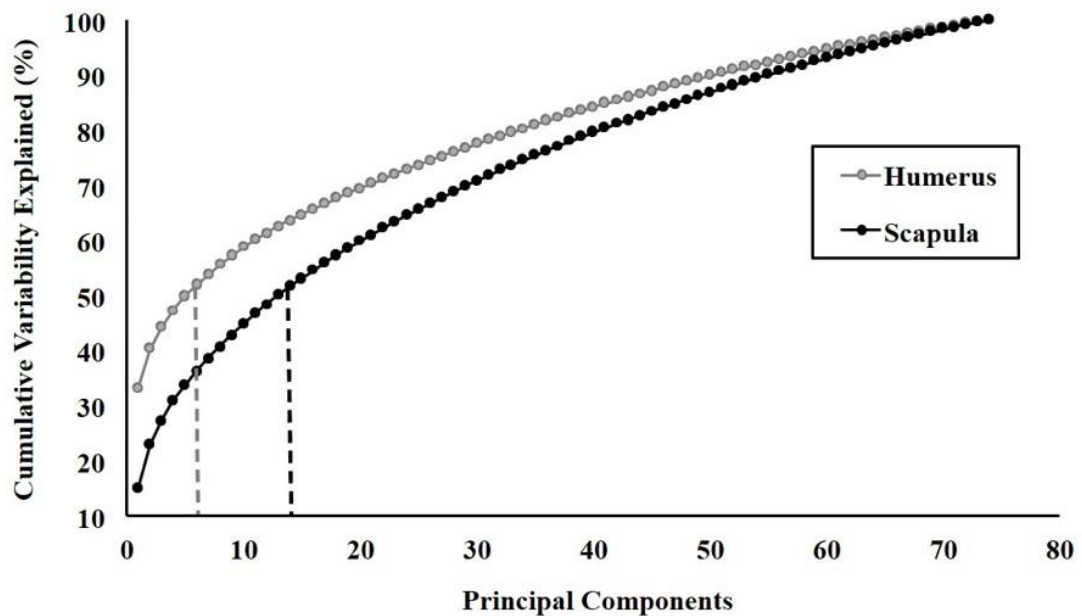
To assess the compactness of the SSMs and SDMs, the percentage of variability between meshes in the training set accounted for by each PC was calculated for both the humerus and scapula (Figure 2.4).

Each statistical analysis using SSM / SDM data only included the first few principal components, which cumulatively accounted for 95% / 50% of the variability in the set as almost all 74 PCs were required in order to describe more than 95% of the variability in the SDMs (required 64 PCs for the scapula, and 61 PCs for the humerus). However, by reconstructing specimens in the set, using a few numbers of PCs, we were able to capture the pattern of density distribution for each specimen (Appendix A).

Ultimately, all statistical analyses of the scapula SSM and SDM data included the first 14 PCs of either model, which cumulatively explained 95.1% and 51.5% of the variability in those models, respectively. All statistical analyses of the humerus SSM and SDM data included the first 6 PCs of either model, which cumulatively explained 95.7% and 51.8% of the variability in those models, respectively.



(a) SSM



(b) SDM

Figure 2.4 Cumulative sum of the variability percentage explained by the respective number of PCs; (a) for the SSM, (b) for the SDM

Sex Analysis

The mean shape of both scapula and humerus is shown in (Figure 2.5), which also shows the average male and female scapula and humerus shapes resulting from the well-matched subsets. Comparing the bone shapes (Figure 2.5 (d)), the male bones in the well-matched set have, on average, a longer medial/inferior border and acromion of the scapula, and a larger humeral head when compared to the average female shape.

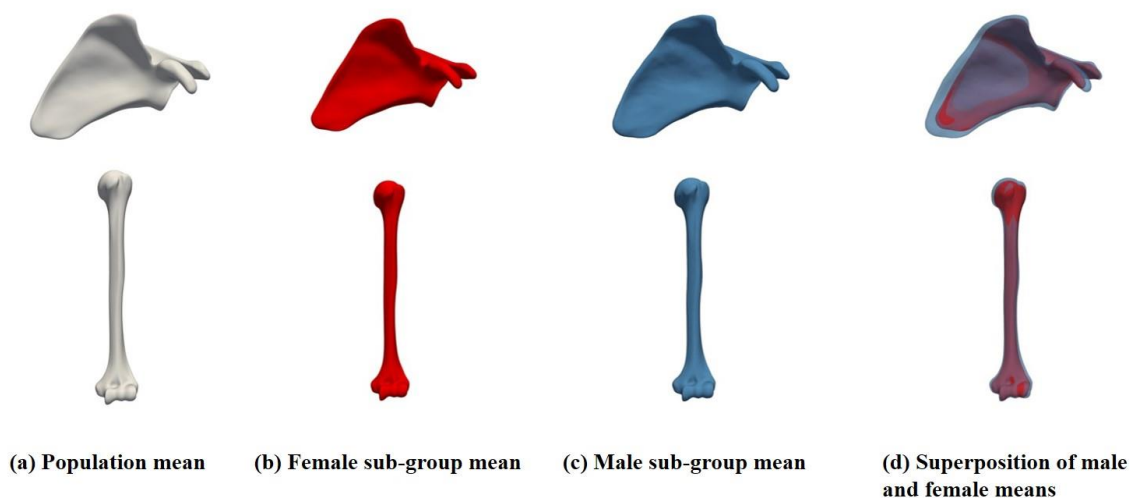


Figure 2.5 The shape of the humerus and scapula averaged over the entire population and averaged over male/female sub-group (These sub-groups were well-matched for age, height, weight, and BMI as explained in Table 2.1)

The PC scores of the SSM for male versus female humeri (Figure 2.6) and scapulae (Figure 2.7) in this set, were compared. For the humerus, statistically significant differences were identified in PCs 3 and 5 of the SSM, with average PC scores differing by $+1.4 \pm 0.3$ and $+1.0 \pm 0.3$ standard deviations, respectively, for males relative to the females (all $p \leq 0.01$). Statistically significant differences were identified in PCs 1, 2, and 9 for the scapula SSM, with average PC scores differing by $+1.3 \pm 0.2$, -1.1 ± 0.4 , and -0.9 ± 0.4 standard deviations, respectively for males relative to the females (all $p \leq 0.04$).

PC Comparison between Male & Female Humerus for Shape

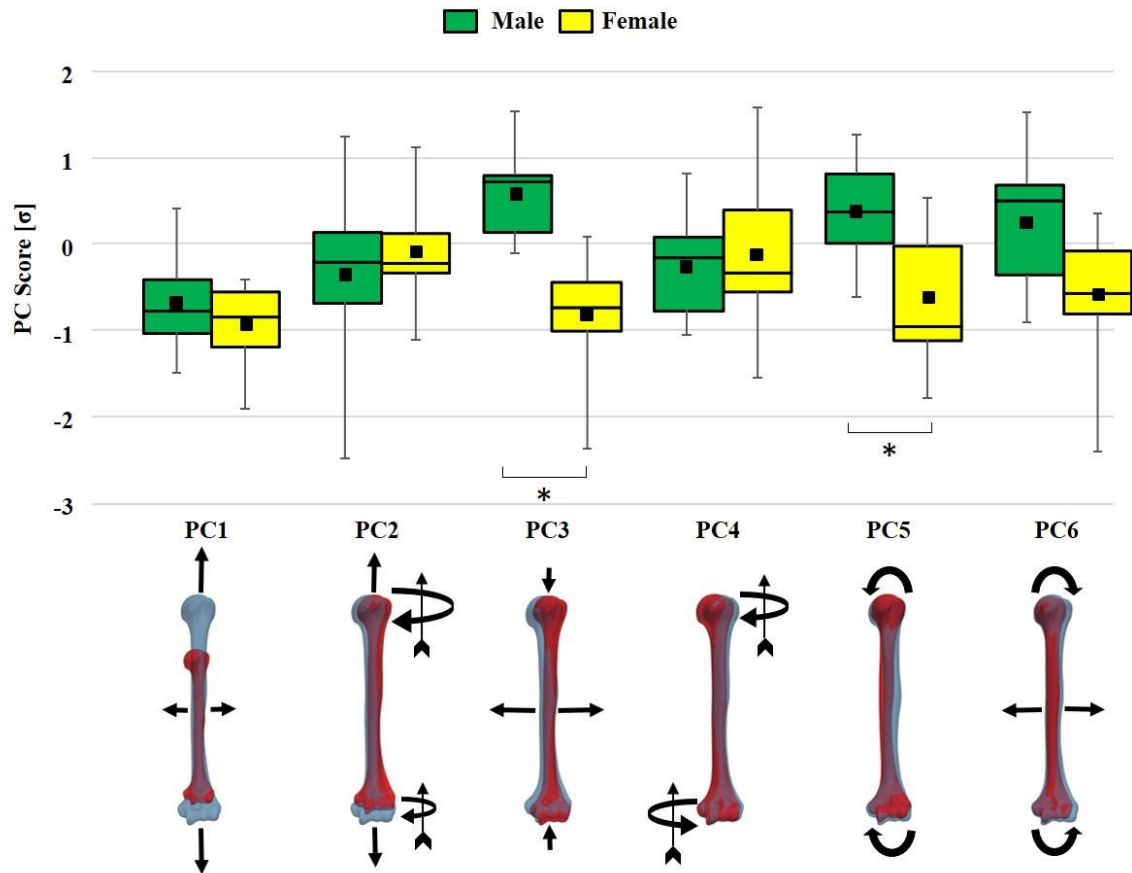


Figure 2.6 The boxplot of the PC scores of male and female humeri in the well-matched set for shape (Green: PC scores of male humeri, yellow: PC scores of female humeri). The boxes represent the 1st to the 3rd quartiles, whiskers represent the range, lines in the box represent the median values, and squares represent the mean values of the PC scores. The blue icons show the average humerus shape deviated along the corresponding PC by $+3\sigma$, while the red icons show the same for deviations by -3σ . The arrows show the effect of each PC on the shape of the humerus along the positive direction of that PC (Arrows with a vane at the end show the directions of out-of-plane rotations).

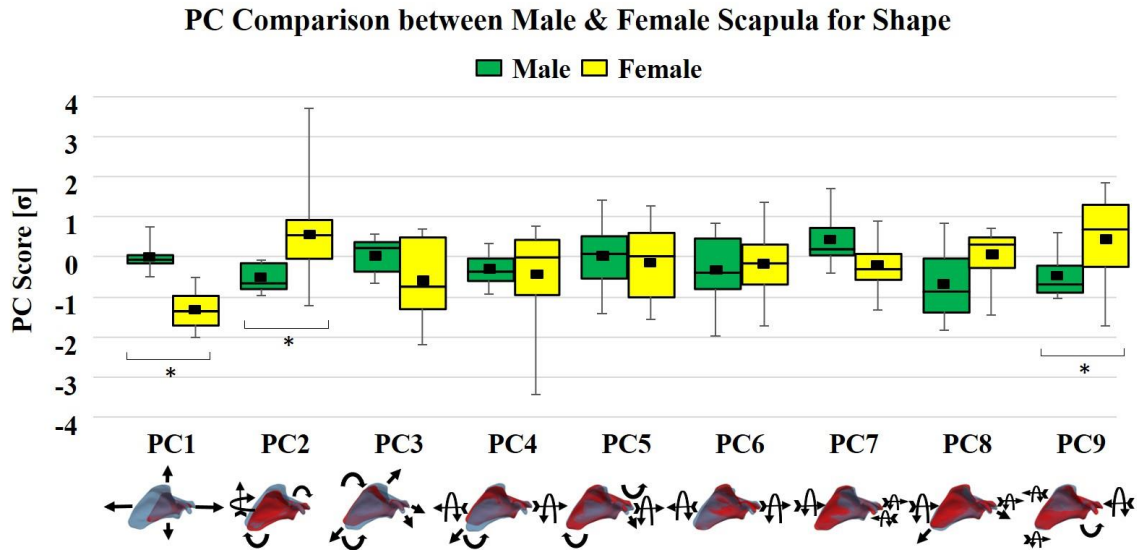


Figure 2.7 The boxplot of the PC scores of male and female scapulae in the well-matched set for shape (Green: PC scores of male scapulae, yellow: PC scores of female scapulae). The boxes represent the 1st to the 3rd quartiles, whiskers represent the range, lines in the box represent the median values, and squares represent the mean values of the PC scores. Only the first 9 PCs, of the 14 used for statistical analyses, are shown for brevity. The blue icons show the average scapula shape deviated along the corresponding PC by $+3\sigma$, while the red icons show the same for deviations by -3σ . The arrows show the effect of each PC on the shape of the scapula along the positive direction of that PC (Arrows with a vane at the end show the directions of out-of-plane rotations).

The PC scores of the SDM for male versus female humerus (Figure 2.8) and scapula (Figure 2.9) were compared as well. For the humerus, statistically significant differences were identified in PC 2, 3, and 5 with average PC scores differing by -1.1 ± 0.5 , $+1.2 \pm 0.4$, and -1.2 ± 0.4 standard deviations, respectively for males relative to the females (all $p \leq 0.04$). For the scapula, statistically significant differences were identified in PC 2 of the SDM, with average PC scores differing by -1.2 ± 0.5 standard deviations, for males relative to the females ($p \leq 0.03$).

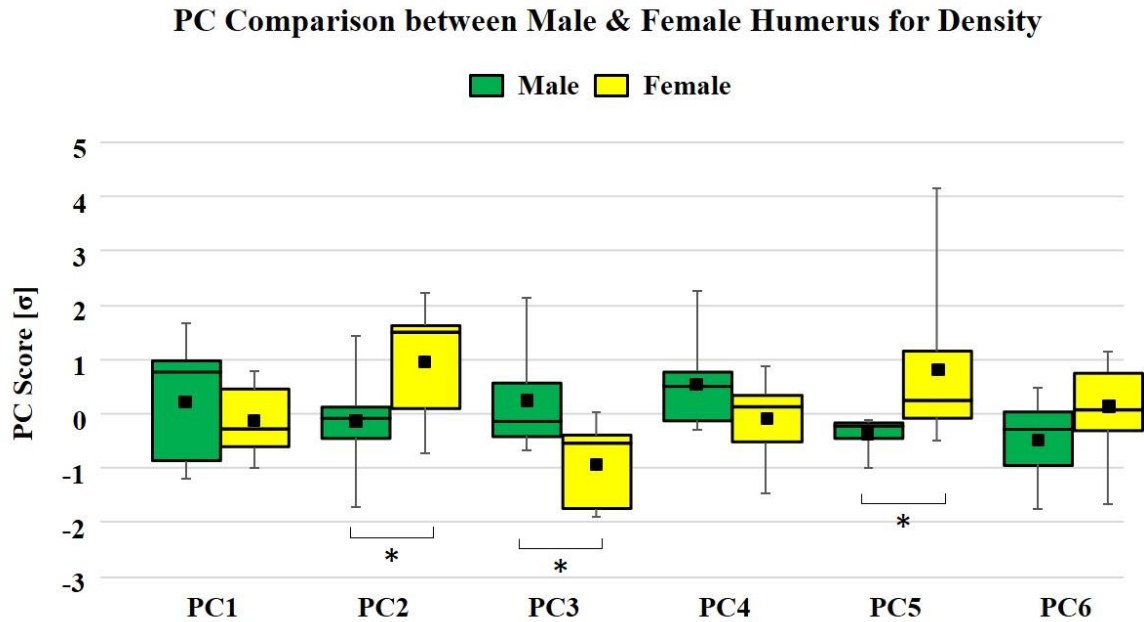


Figure 2.8 The boxplot of the PC scores of male and female humeri in the well-matched set for density (Green: PC scores of male humeri, yellow: PC scores of female humeri). The boxes represent the 1st to the 3rd quartiles, whiskers represent the range, lines in the box represent the median values, and squares represent the mean values of the PC scores.

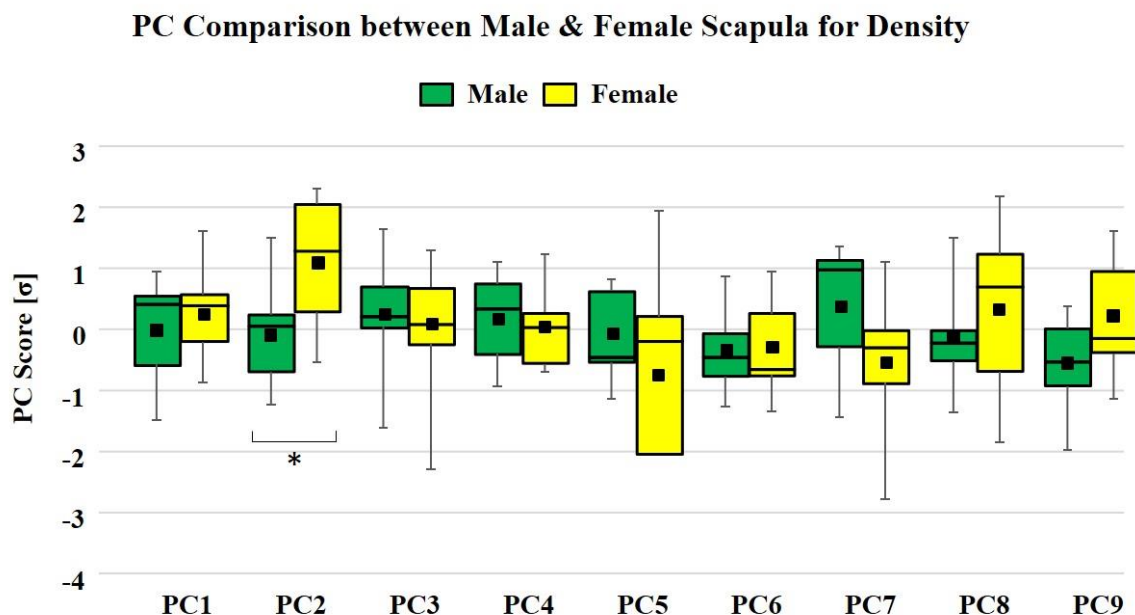


Figure 2.9 The Boxplot of the PC scores of male and female scapulae in the well-matched set for density (Green: PC scores of male scapulae, yellow: PC scores of female scapulae). The boxes represent the 1st to the 3rd quartiles, whiskers represent the range, lines in the box represent the median values, and squares represent the mean values of the PC scores. Only the first 9 PCs, of the 14 used for statistical analyses, are shown for brevity.

The density distribution of the average male and female humerus and glenoid in the well-matched set using all the PCs were compared (Figure 2.10). It can be seen that male humerus and glenoid are denser than the female ones in the trabecular bone region.

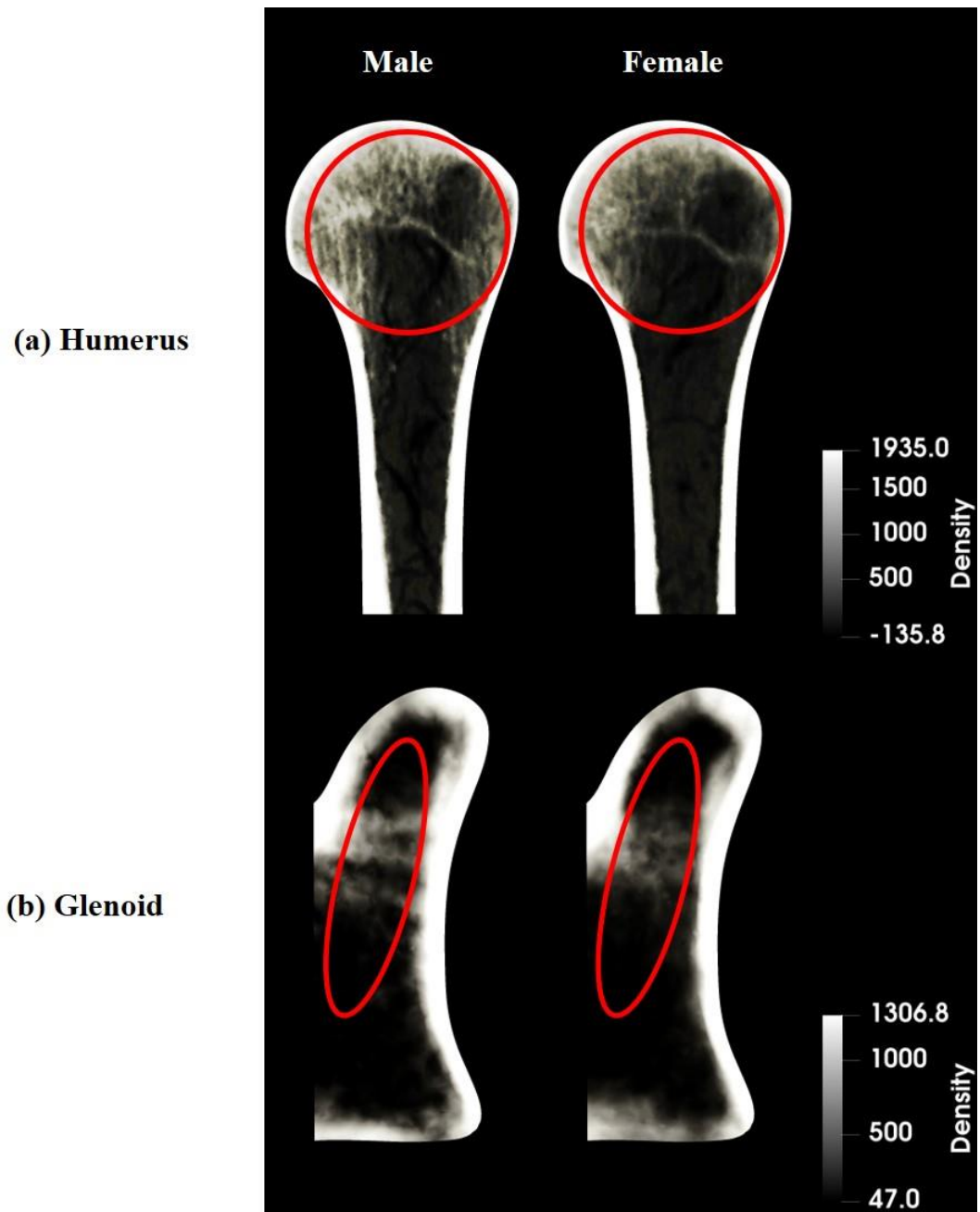


Figure 2.10 Comparing the male with female bone density distribution (Left: male, right: female). They were averaged over the well-matched set and mapped to the overall average bone shape; (a) for the humerus, (b) for the glenoid

Age Analysis

For the humerus, the first and sixth PCs of the SDM demonstrated a weak [131] and moderate (respectively), but significant, correlation with age ($\rho = -0.29$, and $\rho = -0.40$,

both $p \leq 0.03$). For the ten youngest specimens, the averages of the first and sixth PC scores were greater than that of the ten oldest by 1.0 and 0.5 standard deviation, respectively. For the scapula, the first and ninth PCs showed such weak, but significant, correlations ($\rho = -0.31$, and $\rho = -0.32$, both $p \leq 0.02$). For the ten youngest specimens, the averages of the first and ninth PC scores were greater than that of the ten oldest by 1.0 and 0.9 standard deviation, respectively. No other significant correlation was observed for other PCs with age.

Pairs Analysis

Using paired t-tests, PC scores of the SSM & SDM for paired right versus left shoulders for both the humerus and scapula were compared. For the humerus SSM, statistically significant differences were observed in PC 2, 4, and 5 with average PC scores differing by $+0.4 \pm 0.9$, $+0.5 \pm 1.0$, and -0.5 ± 0.9 standard deviations, respectively for right humeri relative to the left ones (all $p \leq 0.04$). For the scapula, statistically significant differences were identified in PCs 4 and 8 of the SSM, with average PC scores differing by $+0.4 \pm 0.6$, and $+0.3 \pm 0.5$ standard deviations, for right scapulae relative to lefts (all $p \leq 0.01$). For the humerus SDM, PC 1 was significantly different, with average PC score differing by -0.3 ± 0.7 standard deviation, for right humeri relative to the lefts ($p \leq 0.03$). For the scapula, statistically significant differences were observed in PCs 2 and 13 of the SDM, with average PC scores differing by -0.4 ± 0.8 , and -0.3 ± 0.7 standard deviations, for right scapulae relative to the lefts (all $p \leq 0.03$).

Correlation between SSM/SDM

Finally, there were weak, but statistically significant, correlations between several PCs of shape and density. For both bones, the first PC of the SSMs, which is generally an overall size scaling factor, showed a weak but, significant correlation, with the second PC of the SDM, which generally influences the thickness of the cortical shell ($\rho = -0.25$, $p \leq 0.03$ for the humerus, and $\rho = -0.39$, $p \leq 0.001$ for the scapula). Also, the first PC of the SSM & SDM for the humerus showed such a correlation. ($\rho = 0.31$, $p \leq 0.01$). The first PC of the SDM mostly scales the density over the entire bone.

2.4 Discussion

The primary objective of this study was to develop shoulder (humerus and scapula bone) SSMs and SDMs, which could have many applications, including population-based modeling of bone-implant mechanics, population-based implant design, computer-aided surgery, etc. After developing these models, statistical analyses were performed on their PCs to find correlations between the shape, density distributions, and demographics of the given population.

The results of this study suggest that, as anticipated, the first PCs of the SSMs describe the size of the bones. As expected, for well-matched individuals of different sex, no statistically significant difference between males and females was observed for the first PC of the humerus SSM. This could be attributed to the effect of size-matching male and female subsets. However, surprisingly, the first PC of the SSM for the scapula was significantly larger for males than the females for the same set. Also, statistically significant differences were found for the third and fifth PC of the humerus SSM between males and females. These PCs appeared to be modes of shape variations that highly depend on *in vivo* mechanical loading conditions (Figure 2.6). Jacobson et al. [132] showed that humerus, scapula, and glenoid morphology varies between males and females. Their study suggests that male humeri are significantly larger than female humeri in approximately two-thirds of anatomic parameters, while the male scapulae are significantly larger than the female ones in approximately half of the anatomic parameters. Although they had matched male and female specimens in terms of age and BMI, they were not matched for height. As a result, the effect of the average height difference between males and females was not taken into account in their work. In another study, Robertson et al. [133], demonstrated that male humeri were significantly longer and had a larger head radius and head thickness than female humeri. Also, there was a significant difference between males and females for their medial head offset. This can also be partially seen through the significant difference in the third PC of the humerus SSM between males and females in our study (Figure 2.6). However, male and female sets were not matched for height, age or BMI in their study.

For the first PC of the SDMs, which scales the density over the entire bone, no statistically significant difference was observed between males and females. However, the second PC of the humerus and scapula, which describes a thinning of the cortical shell, differed significantly between males and females, implying that cortical bone thickness differs between sexes. Due to the fact that females, on average, have significantly higher scores in the second PC of the SDMs than males for both the humerus (Figure 2.8) and scapula (Figure 2.9), our results indicate that males, on average, have thicker cortical bones than females. These findings are generally supported by the literature. Jacobson et al. [132] showed that humeral intramedullary canal diameter and humeral shaft outer diameter is significantly larger for males than females at different heights along the humeral shaft. Although Tingart et al. [134] found no significant differences in mean cortical thickness of the proximal humeral diaphysis between females and males (3.9 ± 0.44 mm vs. 4.6 ± 1.02 mm, $p = 0.08$), the differences were close to being statistically significant. However, male and female sets were not matched for height, age or BMI in their study. They also demonstrated that males have a significantly higher bone mineral density (BMD) in the surgical neck than females, while for the humeral head, as well as the greater and lesser tuberosities, the differences were insignificant. Barvencik et al. [135] concluded that the bone volume to total volume ratio (BV/TV) is significantly different between males and females in half of the regions of interest (ROI) in the frontal plane section of the humeral head (being larger for males in most of ROI).

As hypothesized, our study implies that age has a significant inverse influence on the first PC of the SDMs for both the humerus and scapula, suggesting a natural bone density loss of the shoulder with age. This result is in accordance with that of previously published anatomical studies. A model developed by Roosa et al. [136] indicated that the areal BMD of the proximal humerus declined by 29% between ages 30 and 80 ($p < 0.001$) in addition to declines in cortical bone mass, area, and thickness with aging (all $p < 0.01$). Kirchhoff et al. [137] noticed a strong inverse correlation between age and BV/TV of the humeral head, being more marked in females ($\rho = -0.72$, $p < 0.00001$). In another study by Laval-Jeantet et al. [138], it was shown that the mean cortical porosity grows from 4.6% in men and 4% in women at the age of 40 to more than 10% at the age of 80. Apparent BMD, which is inversely linked to porosity, was shown to decrease with age in both males and

females. Tingart et al. [134] demonstrated that the mean cortical thickness of the proximal humerus is significantly lower in donors aged over 70 versus younger donors (3.8 ± 0.86 mm vs. 4.8 ± 0.96 mm, $p < 0.05$).

One of the interesting findings of this study is that, in terms of the shape, statistically significant differences were observed for contralateral humeri and scapulae. Statistically significant differences in PCs 2, 4, and 5 of the humerus SSM and PCs 4 and 8 of the scapula SSM were observed. However, they combined only explain 5.8% and 8.9% of the variability in shapes in our set, respectively. Therefore, these differences in shape may be inconsequential, implying that contralateral shoulders have quite symmetric shapes.

A common method to evaluate the native shape of a bone for computer-aided planning of a reconstructive surgery is using its contralateral bone as a template; for instance, Gelaude et al. [139] applied this technique for pelvic reconstructive surgery, and Verhaegen et al. [140] showed the feasibility of using contralateral scapulae as a reliable template to guide shoulder surgical reconstruction. They demonstrated that contralateral scapulae are quite symmetrical in terms of scapular offset, glenoid inclination, and version. Also, Shi et al. [141] indicated that there is no significant difference in contralateral glenoids' length ($p = 0.53$), width ($p = 0.42$), area ($p = 0.36$), or circumference ($p = 0.73$) and concluded that contralateral glenoids are strongly symmetric in shape and size.

However, the symmetry of contralateral scapulae in terms of density has not been investigated to the best of authors' knowledge. Diederichs et al. [142] concluded that there is a strong correlation between contralateral humeri in terms of BMD for both the distal ($\rho = 0.90$) and the proximal humerus ($\rho = 0.74$) (all $p < 0.01$), which may be due to the symmetrical *in vivo* biomechanical loading conditions. Yet, the results of our study indicated that the first PC of the SDM, which mostly scales the density over the entire bone, is significantly different between contralateral humeri. This implies that there is, to some extent, asymmetry in the density of the paired humeri. Also, statistically significant differences in the second PC of the SDM for contralateral scapulae were observed, suggesting a difference in the thickness of the cortical shell between paired scapulae. These observations can be attributed to the effect of the dominant hand and the associated

asymmetry in the *in vivo* biomechanical loadings. However, as the information regarding the dominant hand of the donors was not available, we were not able to further investigate this effect.

Interestingly, the first PC of the SSM was significantly correlated with the second PC of the SDM, for both the humerus and the scapula. This finding suggests that there is a direct, significant correlation between the size of a bone and the thickness of its cortical shell. Furthermore, the first PC of the SSM and the SDM of the humerus are significantly correlated, which implies that the larger humeri are also, on average, denser. A strength of our study was developing separate statistical models for shape and density instead of combining them into a single model, as in the works of [91], [93], [113]. This allowed us to separate the correlated main modes of shape and density variation of the shoulder.

Our study is limited by the number of specimens and their age range (mean 73 ± 13). However, the sensitivity of our results to the number of included specimens was investigated through a robustness study (Appendix C). In the future, by including younger specimens, we will be able to further investigate the effect of age on the density distribution of the shoulder. Another limitation of our study is that 71 out of 75 specimens were from donors of Caucasian ethnicity; including specimens from other ethnicities in future studies would allow us to investigate the effect of this factor on the shape and density distribution of the bones. The lack of compactness of the SDMs, compared to our SSMs (where only a few PCs were required to describe 95% of shape variations of the bones), is a limitation of our model; however, the SDMs could still successfully be used to reconstruct all the specimens in our set and capture the pattern of their density distribution effectively (Appendix A). This lack of compactness can be attributed to the high three-dimensional variability in density distribution across specimens (compared to shape variations), possibly due to adaptations of bones according to their *in vivo* mechanical loadings. Furthermore, the SSMs only considered the external cortex of the bones. In future studies, including the inner cortical boundary (and therefore cortical bone thickness) as a shape parameter may be more effective than incorporating it as a bone density distribution parameter. This may allow more compact SDMs; however, it will likely increase variability in the SSMs. Moreover, the density distribution for the humerus is more uniform compared

to the scapula, which has more complex geometry and density distribution. In future work, it may be advantageous to develop scapula SDMs that focus more on a certain area of interest (e.g., the glenoid), as the actual structural distribution of bone in different regions may not be of use in all models.

The statistical shape and density models are tools capable of describing the main modes of variation in the shape and density distribution of the shoulders in a population. This study suggests that the demographics of a population, such as sex and age, have a significant influence on the shape and density distribution of the shoulder and encourages the use of contralateral bones as templates for shoulder reconstruction. Also, it shows that there is a significant correlation between many modes of shape and density variations in the shoulder. The results of this study can help guide the designs of population-based prosthesis components and can be useful for computer-aided surgical navigation, surgical implant positioning and also preoperative surgical planning.

Chapter 3

3 Structural Analysis of Hollow- Versus Solid-stemmed Shoulder Implants of Proximal Humeri with Different Bone Qualities

The current chapter examines the implications of using hollow-stemmed implants on changes in the stress distribution of bone and percentage of bone volume with resorption/formation potential following bone reconstruction. Also, these outcome measures were quantified for humeri with different bone qualities to assess the effect of osteoporosis on the severity of stress shielding.

3.1 Introduction

Total shoulder arthroplasty (TSA) is one of the most successful procedures to treat osteoarthritis of the glenohumeral joint by reducing pain levels and restoring nearly normal shoulder function [143]–[147] leading to significant growth in its use over the past decades [5], [105]–[107]. Among all human joint replacements, it has the most rapid growth with a projected seven-fold increase in its utilization over the next decade [4]. However, stress shielding of bone around the stem component of shoulder replacement implants can occur as a long-term complication of TSA due to the altered pattern of load transfer relative to the intact state. This can trigger a cascade effect where the resulting adaptive bone remodeling and bone resorption can lead to implant loosening and the need for revision surgeries [8]–[10]. Inoue et al. [9] observed that bone resorption occurred in 85.7% of 147 patients who underwent TSA with uncemented stems. Moreover, elderly patients with osteoarthritis undergoing TSA may suffer from concurrent osteoporosis [11]–[13]. Pervaiz et al. [11] reported that 12% of 230 osteoarthritic patients who underwent TSA were osteoporotic, while 44% were osteopenic. Due to the lower rigidity of the osteoporotic versus normal healthy bone, there is an amplified stiffness difference between the humerus and implant, making osteoporosis at the time of implantation a risk factor [8].

The design of humeral stems has a significant impact on the overall implant success, as they are responsible for load transfer from the head component of the implant to the bone [148]–[150]. In attempts to reduce the amount of stress shielding-induced bone remodeling,

it has been shown that reducing the stem length can result in bone stresses that better match the intact state of long bones [67], [151]–[153]. However, there are concerns regarding the long-term stability and alignment of stemless implants [151], [154], [155]. The use of more flexible stems could mitigate the effect of stress shielding while maintaining some of the benefits of longer stems.

Conventional manufacturing techniques limit our ability to create metallic stems with reduced stiffness while simultaneously satisfying shape, materials and durability constraints. Recent advances in additive manufacturing (AM) have enabled the production of parts with complex geometries and stiffness distributions from biocompatible metal alloys [156], [157]. Hollow stems fabricated using AM could be an attractive solution to the problem of stress shielding in the surrounding bone. Hollow stems have been explored for the stem components of hip implants providing a better performance compared to solid stems [158]–[161], but the use of hollow stems for TSA implants has not yet been documented.

In light of the foregoing, the objective of this computational study was to determine if hollow titanium stems can mitigate stress shielding at the proximal humerus for a variety of bone qualities using finite element (FE) methods. We hypothesize that hollow TSA implant stems will result in stresses that better mimic the intact state and reduced bone resorption potential in comparison with solid stems. Also, we anticipate significant differences between healthy, osteopenic, and osteoporotic bones in terms of stress distribution and the risk of bone resorption following reconstruction using both the solid- and hollow-stemmed implants.

3.2 Methods

Development of Artificial CTs

A statistical shape and density model (SSDM) of the humerus based on 75 cadaveric shoulders (37 males and 17 females, 21 pairs, 73 ± 13 years) was previously developed which resulted in a mesh for each specimen with similar topology and identical node numbering but customized to the individual shape of each specimen. Having the same

topology enabled node-to-node density comparison between the models of each specimen. The homologous meshes were leveraged to simulate an average computed tomography (CT) image by averaging the shapes and densities in the Hounsfield unit (HU) at each mesh node across all the specimens. Three equidistant transverse slices were then defined along the distance from the superior edge of the average proximal humerus to approximately the surgical neck (Figure 3.1). The density distributions in HU for each of the donors were mapped onto the average humerus shape (pairs were averaged), and the mean of the three proximal slices (excluding the cortex) was calculated. Next, donors were sorted in terms of the calculated proximal densities and classified as healthy, osteopenic and osteoporotic based on the density ranges defined by Pervaiz et al. [11] (Table 3.1). It should be noted that our cutoff HUs were shifted by amounts of differences in the mean of proximal densities over our sample and over the sample of Pervaiz et al. [11] to account for possible systematic errors.

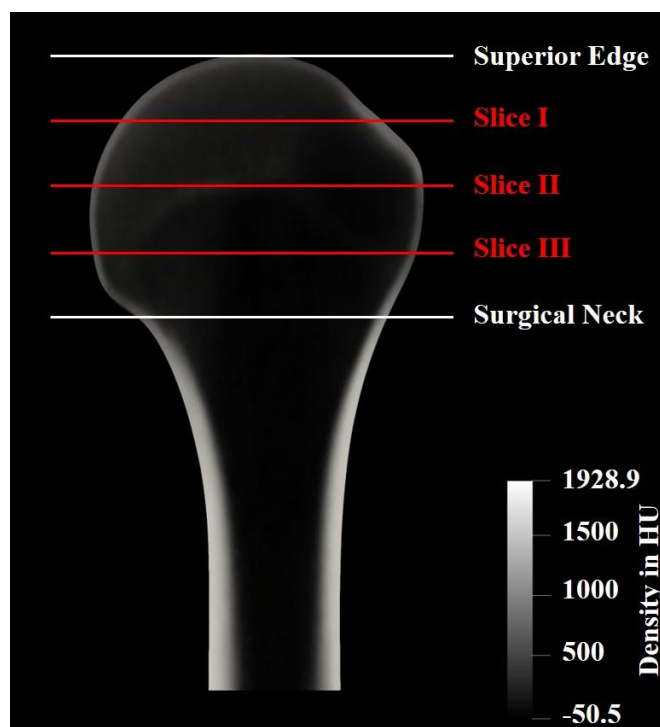


Figure 3.1 Defined slices to measure density in the proximal humerus (Three equidistant transverse slices were defined along the distance from the superior edge of the average proximal humerus to approximately the surgical neck)

Table 3.1 Number of donors in each category of bone disease conditions along with the cutoff HUs used for classifications

Bone Disease Conditions	Number of Donors	HU Ranges in Proximal Humerus
Healthy	23	$HU \geq 144.5$
Osteopenic	11	$129.9 \leq HU < 144.5$
Osteoporotic	20	$HU < 129.9$

Based upon this categorization, two more artificial CTs were developed by preserving the shape of the average CT but mapping the average densities of all the healthy and then osteoporotic donors, respectively, onto the same mesh allowing for direct comparisons.

Development of 3D Humeri Models and in silico Osteotomy

Using the 3D medical image processing software 3DSlicer [126], the cortical and trabecular bones were separately segmented for each of the artificial CTs by using an upper threshold of 600 HU for the trabecular bone [162] followed by manual identification of the inner cortical boundaries. Separate three-dimensional surface models were created for cortical and trabecular bones (including internal canal). The bottom one-third of all the bones were resected transversely to reduce the computational cost of FE analysis. Next, three bones representing an average (classified as osteopenic), a healthy and an osteoporotic humerus were virtually resected according to standard surgical approaches confirmed by an orthopedic surgeon (G. Athwal). The resected bones acted as hosts for testing the performance of solid- and hollow-stemmed implants for TSA.

Implant Design and Positioning

Two generic solid- and hollow-stemmed (with an inner-wall thickness of 1 mm) implant models sharing an identical humeral head component were developed using SolidWorks software (Dassault Systèmes, Waltham, MA, USA). These short implants (~70 mm) only differed in terms of the presence of a hollow in their stems and had identical stem lengths and outer boundaries. Boolean operations were used to virtually ream the bones and position the implants at the same locations across all the models. The implants were centered in the diaphyseal canal and the bottom surface of the head components were made

coincident with the resected surface of the bones and concentric with a circle fit onto that surface. This way, we avoided gaps between bones and head components as per current surgical practice (Figure 3.2). The positioning of implants was reviewed by an orthopedic surgeon.

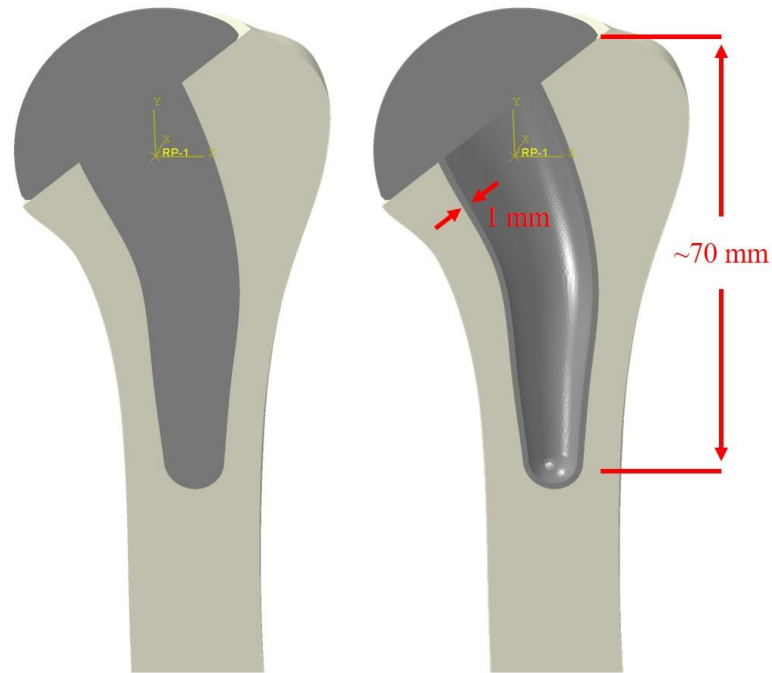


Figure 3.2 Solid- and hollow-stemmed implants with similar lengths and identical head components positioned centrally in the diaphyseal canal

Mesh Planning

Aligned model components were imported into the ABAQUS 2018 FE analysis software suite (Dassault Systèmes, Johnston, RI, USA). Three models were developed for each of the three humerus models: (1) an intact proximal humerus, (2) a solid-stemmed implant reconstructed humerus, and (3) a hollow-stemmed implant reconstructed humerus. The meshing was planned such that it respected the outer boundaries of stems and inner boundaries of cortical bones (Figure 3.3). This way, we ensured identical meshing of intact and reconstructed models for each bone, outside of where resecting/reaming had occurred, allowed for element-by-element comparisons of outcome measures and assured consistency of material properties. Each of the bones and implants was meshed using

quadratic tetrahedral elements with an average edge-length of 1.5 mm based on mesh convergence analysis results of similar studies for shoulder [67], [78], [163].

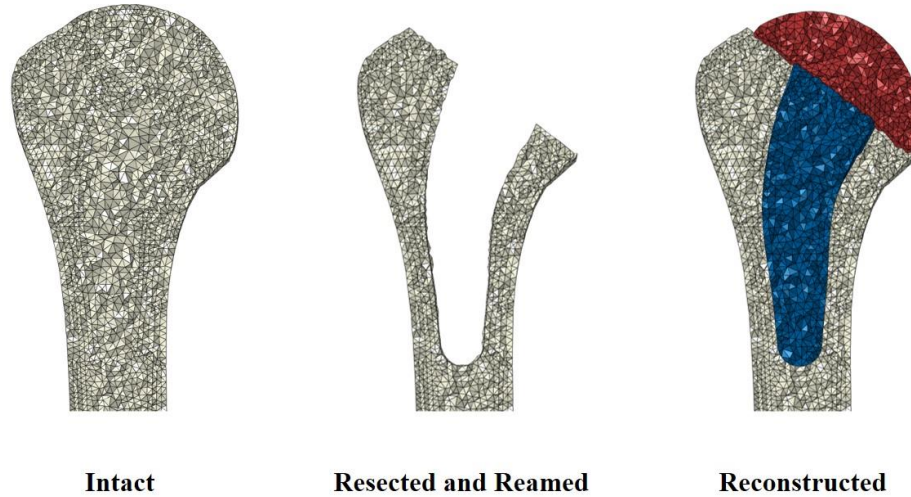


Figure 3.3 Mesh Planning (The mesh was planned such that it respected the outer boundaries of stems and inner boundaries of cortical bones)

Application of Material Properties

Cortical and trabecular bones were modeled as isotropic and inhomogeneous materials, with Young's moduli defined element-by-element based on the corresponding population-averaged CT image intensities (in HU) to better mimic *in vivo* bone mechanical properties [46], [163], [164]. In this regard, CT attenuation values (HU) were first converted to apparent bone densities (ρ_{app} in $\frac{g}{cm^3}$) using a calibration relationship (Equation 3.1) [51]:

$$\rho_{app} = 0.001044 \times HU \quad (\text{Equation 3.1})$$

Consequently, using MITK-GEM [130], which is an open-source software to generate FE models from medical images, Young's moduli were calculated for each element. In order to do so, apparent bone densities were first converted to corresponding Young's moduli using density-modulus relationships available in the literature [43], [48]. For trabecular bone, the equation reported by Morgan et al. [48] was used (Equation 3.2):

$$E = 8920\rho_{app}^{1.83} \quad (\text{Equation 3.2})$$

Where E is Young's modulus in MPa. However, for cortical bone, to prevent overestimation of Young's moduli which would result from using the aforementioned equation, The relationship derived by Austman et al. for ulna cortical bone [43] was utilized (Equation 3.3):

$$E = 8346\rho_{app}^{1.5} \quad (\text{Equation 3.3})$$

Next, the moduli were mapped from the CT grid locations into a single value for each element (partial volume artifacts were also corrected) [164]. A total of 1000 possible material bins were considered, and each element was assigned to the appropriate material group to reduce computational cost. A minimal stiffness of 0.001 MPa was assigned to all the elements of the diaphyseal canal. For all the models, the stem component material was defined as titanium (E = 110 GPa), while the material property of cobalt-chrome was applied to the humeral head component (E = 210 GPa). In agreement with previous studies, the Poisson's ratio for all the bones and implant components was set to 0.3 [46], [51], [67], [78], [165], [166]. Grit blast surface textures were assumed for implant-bone interface and frictional contact was modeled using a penalty-based approach ($\mu = 0.63$) [67], [78], [167].

Loading Configurations and Boundary Conditions

To simulate common arm motions, four different loading scenarios (45° and 75° of shoulder abduction as well as 90° and 120° of flexion) based on an *in vivo* study by Bergmann et al. [28] were applied to each host bone, while keeping the forces identical across intact and reconstructed models. The joint reaction forces and frictional moments were calculated using the average weight of donors (63.5 kg) (Table 3.2). To find nodes that will be used for applying loads anatomically, the average humerus and the corresponding average scapula (derived from our SSDM) were registered to the bones in Holzbaur's shoulder model [168] in the neutral body position using anatomic landmarks within the open-source OpenSim software [169]. A circle was then fitted onto the glenoid surface of the scapula. The center of that circle was projected onto the articular surface of

the corresponding humerus. Next, assuming a fixed 2:3 ratio of glenohumeral abduction/flexion to scapulothoracic motion (scapulohumeral rhythm) [30], for each loading configuration, the projected point was appropriately rotated, and all the nodes in its vicinity within the radius of the fitted circle were used to apply loads. Humeral coordinate systems were defined for right humeri [170], and these nodes were rigidly fixed to a reference point at the humeral head center. The components of loads and moments were then directly applied to the reference point [28]. Distal ends of humeri were fully constrained (Figure 3.4) [67], [78].

Table 3.2 Values of joint reaction forces (N) and frictional moments (N.mm) applied to the reference point along with their resultants during investigated activities

Activity	F_x	F_y	F_z	$F_{Resultant}$	M_x	M_y	M_z	$M_{Resultant}$
45° of Abduction	130.8	-274.1	99.7	319.6	1370.5	1183.6	872.1	2009.9
75° of Abduction	211.8	-461.0	155.7	530.7	1806.5	1681.9	1495.0	2885.7
90° of Flexion	193.1	-417.4	143.3	481.7	809.8	498.3	-747.5	1209.5
120° of Flexion	317.7	-666.5	230.5	773.5	1868.8	1370.5	2242.6	3224.9

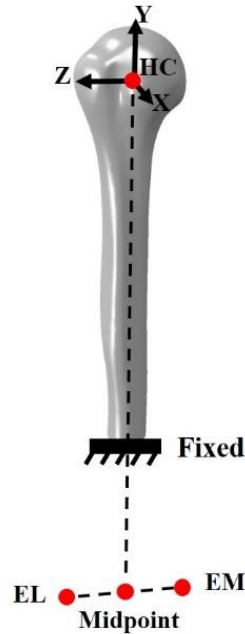


Figure 3.4 Humeral coordinate systems used for the right humeri along with the boundary conditions applied to their distal end. Y-axis connects the humeral head center (HC) to the midpoint of the most caudal point on lateral epicondyle (EL) and the most caudal point on medial epicondyle (EM); Z-axis points laterally in the plane spanned by the long axis of the humerus (Y-axis) and EM/EL; X-axis is directed anteriorly.

Outcome Measures

36 FE analyses were performed on all the host bones (healthy, osteopenic, and osteoporotic humeri) for each model (intact, solid-stemmed, and hollow-stemmed reconstructed models) and each loading scenario (2 different degrees of abduction/flexion) in ABAQUS 2018 to assess the following outcome measures: (1) The volume-weighted average change in the magnitude of von Mises stress of the bone following reconstruction calculated with respect to the intact state ($\Delta\sigma_{VWA}$) (Equation 3.4 - Equation 3.6).

$$\Delta\sigma_{VWA} = \frac{\sum(\Delta\sigma_{VM1}) \times Volume_{Reconstructed\ Element}}{\sum(\sigma_{VM})_{Intact} \times Volume_{Reconstructed\ Element}} \times 100 \quad (Equation\ 3.4)$$

$$\Delta\sigma_{VM1} = (\sigma_{VM})_{Reconstructed} - (\sigma_{VM})_{Intact} \quad (Equation 3.5)$$

$$\sigma_{VM} = \sqrt{0.5 \times [(\sigma_{11} - \sigma_{22})^2 + (\sigma_{22} - \sigma_{33})^2 + (\sigma_{33} - \sigma_{11})^2 + 6 \times (\sigma_{12}^2 + \sigma_{23}^2 + \sigma_{31}^2)]} \quad (Equation 3.6)$$

(2) The volume-weighted average deviatoric component of the change in stress tensor with respect to the intact state to capture any changes in the direction of stress (ΔS) (Equation 3.7 - Equation 3.9).

$$\Delta S = \frac{\sum(\Delta\sigma_{VM2}) \times Volume_{Reconstructed Element}}{\sum(\sigma_{VM})_{Intact} \times Volume_{Reconstructed Element}} \times 100 \quad (Equation 3.7)$$

$$\Delta\sigma_{VM2} = \sqrt{0.5 \times [(\Delta\sigma_{11} - \Delta\sigma_{22})^2 + (\Delta\sigma_{22} - \Delta\sigma_{33})^2 + (\Delta\sigma_{33} - \Delta\sigma_{11})^2 + 6 \times (\Delta\sigma_{12}^2 + \Delta\sigma_{23}^2 + \Delta\sigma_{31}^2)]} \quad (Equation 3.8)$$

$$\Delta\sigma_{ij} = (\sigma_{ij})_{Reconstructed} - (\sigma_{ij})_{Intact} \quad (Equation 3.9)$$

Where i, and j = 1, 2, 3.

(3) The percentage of bone volume with the potential for bone resorption/formation (bone remodeling).

The strain energy density (SED) of each element in the reconstructed models was compared to its intact value. If the SED of the reconstructed element was more than 55% above/below its intact state, the element was classified as having the potential for bone formation/resorption according to established strain-adaptive FE models in the literature [37], [73], [78].

These outcome measures were separately quantified for the cortical and trabecular bones of each model. For cortical bones, they were averaged over each of the eight equidistant transverse slices defined along the top 80 mm of the proximal humeri. However, for trabecular bones, outcome measures could only be calculated for the top four slices due to the absence of the trabecular bones in the inferior slices (Figure 3.5). Also, the outcome measures were averaged over the entire cortical/trabecular bones in the top 80 mm/40 mm of the proximal humeri. Additionally, maximum stresses in the implants were calculated and compared to the yield stresses of their components.

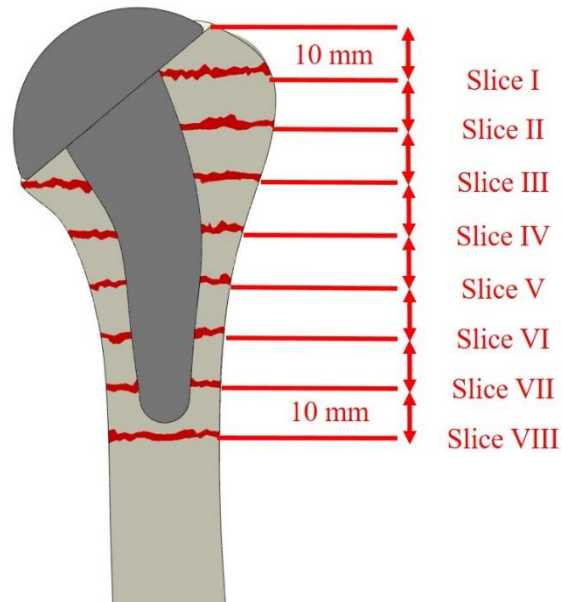


Figure 3.5 Outcome measures were quantified regionally for chosen cortical and trabecular bone slices (defined transversely along the top 80 mm of the proximal humeri).

Statistical Analyses

To evaluate the effect of bone disease condition (healthy, osteopenic, osteoporotic) and hollowness of stem components on the outcome measures, using SPSS software (IBM, Armonk, NY, USA), a two-way repeated-measures analysis of variances was performed ($\alpha = 0.05$).

3.3 Results

Change in the Magnitude of von Mises Stress

Cortical region

Following reconstruction with a humeral stem, the volume-weighted average magnitude of the von Mises stress in cortical bone decreased with respect to its intact state for the top five slices for all bone and stem conditions (Figure 3.6). However, beginning with slice 6, it slightly increased. Overall, cortical bone experienced a decrease in stress when an implant was used (in comparison to the corresponding intact state), ranging from $5.9\% \pm$

0.3% (standard deviation) when the hollow-stemmed implant and average bone material properties were used to $6.8\% \pm 0.4\%$ when a solid-stemmed implant and osteoporotic bone material properties were used.

Statistically significant differences in cortical bone stresses were observed between solid- and hollow-stemmed implants across the majority of sampling locations (slices) and bone material properties. Statistically significant differences were also observed between healthy, average, and osteoporotic bone material properties for most of the stem conditions and sampling locations. On average, the change in cortical bone stress (with respect to the intact bone) with the hollow-stemmed implant was less than with the solid-stemmed implant by $0.3\% \pm 0.02\%$, $0.2\% \pm 0.02\%$, and $0.1\% \pm 0.02\%$ for healthy, average, and osteoporotic bone material properties, respectively (all $p \leq 0.001$). Using the hollow-stemmed implant, the average change in cortical bone stress for healthy and osteoporotic bone material properties were greater than for the average bone material properties by $0.3\% \pm 0.03\%$, and $0.8\% \pm 0.2\%$, respectively (all $p \leq 0.02$). The same significant differences between bone qualities were observed for the solid-stemmed implant (all $p \leq 0.02$).

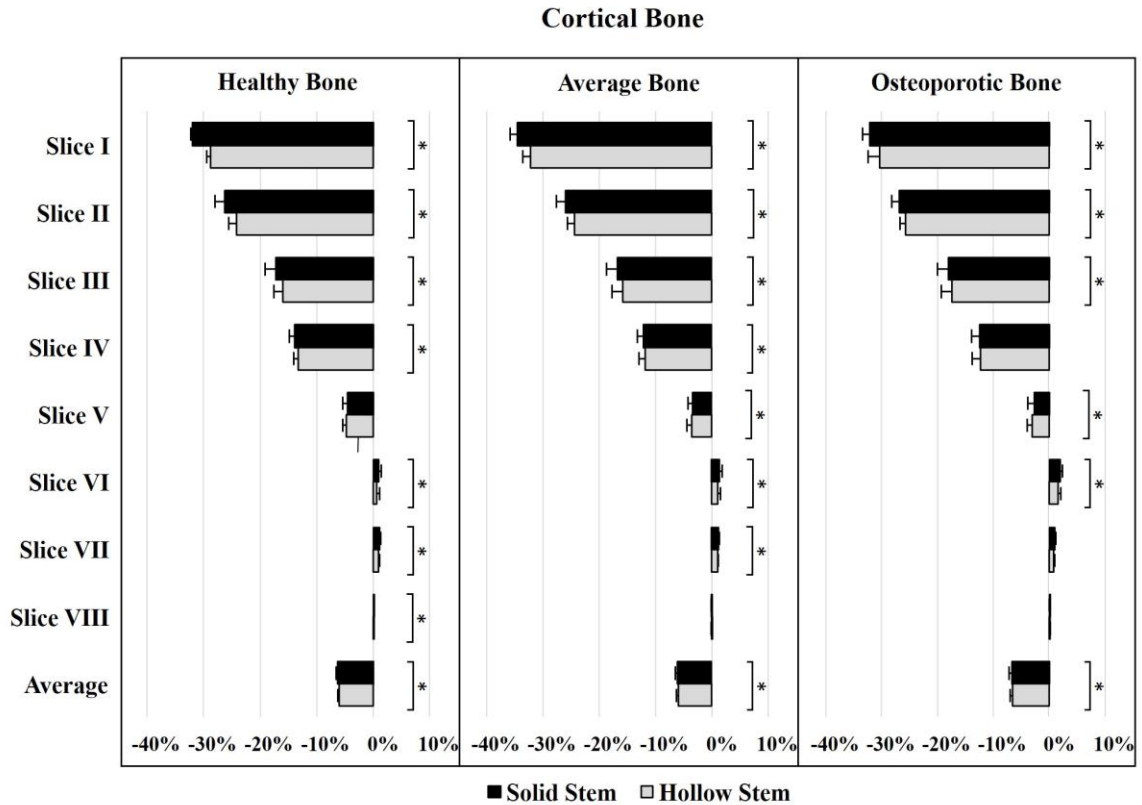


Figure 3.6 The volume-weighted average change in the magnitude of von Mises stress for the reconstructed cortical bone (as a percentage of its intact state ($\Delta\sigma_{VWA}$) for each bone condition and each stem design). Mean (+ standard deviation) stresses in each cortical bone slices as well as the entire cortical bone in the top 80 mm of the proximal humerus are presented (stresses are averaged over different loading configurations). * shows a significant difference between stems.

Trabecular region

Similarly, for trabecular bone, the von Mises stress declined with respect to its intact state following reconstruction, for all the bone material properties and stem types (except in the most proximal slice of the osteoporotic bone) (Figure 3.7). On average, the trabecular bone showed a reduction in von Mises stress (in comparison to the corresponding intact state) ranging from $11.1\% \pm 1.9\%$ when using the hollow-stemmed implant and osteoporotic bone material properties to $16.0\% \pm 1.3\%$ when using the solid-stemmed implant and healthy bone material properties.

Statistically significant differences were observed in the changes in trabecular bone von Mises stresses between the solid- and hollow-stemmed implants, at slice 1 and 2, and the average across the entire trabecular bone region, for all bone material properties. On average, the change in trabecular bone von Mises stress when using the hollow-stemmed implant was less than when the solid-stemmed implant was used, by $1.6\% \pm 0.08\%$, $1.3\% \pm 0.08\%$, and $0.7\% \pm 0.1\%$ for simulated healthy, average, and osteoporotic bone material properties, respectively (all $p \leq 0.001$). Also, considering the average von Mises stress across all trabecular bone, significant differences were observed in results obtained using different bone material properties for both the solid and hollow stem implants (all $p \leq 0.01$). The largest differences in changes in the overall average trabecular von Mises stress occurred between the results for the solid-stemmed implant, whose decreases in stress with healthy bone material properties were greater than when osteoporotic bone material properties were used, by $4.2\% \pm 0.5\%$.

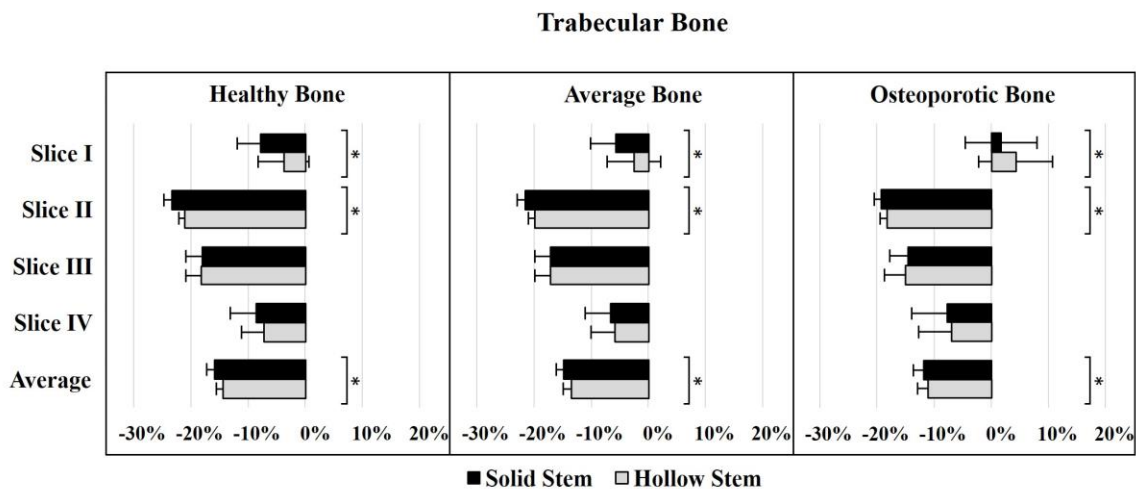


Figure 3.7 The volume-weighted average change in the magnitude of von Mises stress for the reconstructed trabecular bone (as a percentage of its intact state ($\Delta\sigma_{VWA}$) for each bone condition and each stem design). Mean (+ standard deviation) stresses in each trabecular bone slices as well as the entire trabecular bone in the top 40 mm of the proximal humerus are presented (stresses are averaged over different loading configurations). * shows a significant difference between stems.

Deviatoric Component of the Change in Stress Tensor

Cortical region

The volume-weighted average deviatoric component of the change in stress tensor for the reconstructed cortical bone decreased by moving distally along the bone (Figure 3.8). Overall, cortical bone experienced a deviatoric change in stress tensor when an implant was used (with respect to the corresponding intact state), ranging from $13.4\% \pm 0.6\%$ when the hollow-stemmed implant and healthy bone material properties were used to $17.0\% \pm 1.3\%$ when a solid-stemmed implant and osteoporotic bone material properties were used.

Statistically significant differences were observed between solid- and hollow-stemmed implants across all the slices and bone material properties (except for the most proximal slice of the osteoporotic bone). On average, the deviatoric stress change in cortical bone (with respect to the intact state) with the hollow-stemmed implant was less than with the solid-stemmed implant by $1.6\% \pm 0.1\%$, $1.2\% \pm 0.1\%$, and $1.1\% \pm 0.1\%$ for healthy, average, and osteoporotic bone material properties, respectively (all $p \leq 0.001$). Also, considering the average deviatoric change in stress across the proximal cortical bone, significant differences were found in results attained using different bone material properties, for both the solid and hollow stem implants (except between healthy and average bone material properties when the solid-stemmed implant was used) (all $p \leq 0.03$). The largest differences in deviatoric changes in the overall average cortical stress tensor occurred between the results for the hollow-stemmed implant, whose deviatoric stress change with osteoporotic bone material properties were greater than when healthy bone material properties were used, by $2.5\% \pm 0.7\%$.

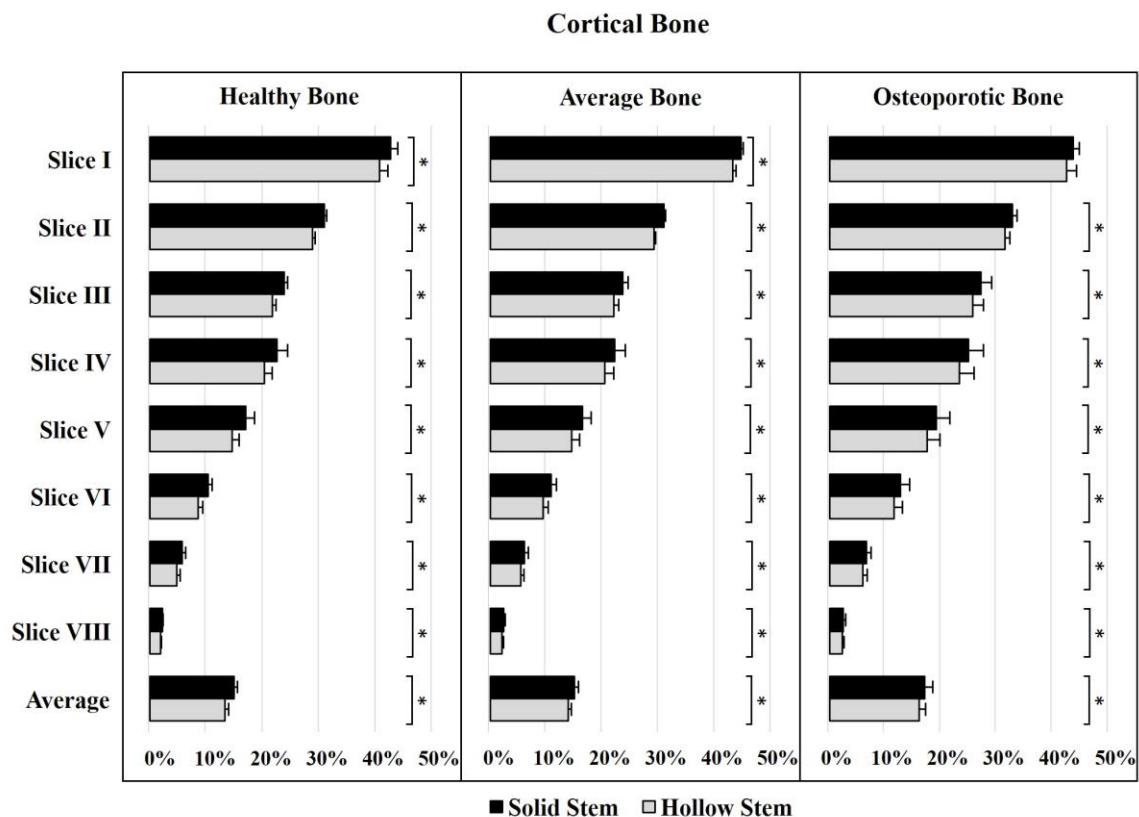


Figure 3.8 The volume-weighted average deviatoric component of the change in stress tensor for the reconstructed cortical bone (as a percentage of its intact state (ΔS) for each bone condition and each stem design). Mean (+ standard deviation) stresses in each cortical bone slices as well as the entire cortical bone in the top 80 mm of the proximal humerus are presented (stresses are averaged over different loading configurations). * shows a significant difference between stems.

Trabecular region

For trabecular bone, the average deviatoric change in stress was more pronounced than cortical bone (Figure 3.9). On average, trabecular bone experienced a deviatoric change in stress tensor when an implant was used (with respect to the intact state), ranging from $40.1\% \pm 1.5\%$ when the hollow-stemmed implant and average material properties were used to $45.0\% \pm 2.1\%$ when a solid-stemmed implant and osteoporotic material properties were applied. Statistically significant differences were observed between solid- and hollow-stemmed implants across all the slices and bone material properties (except for the

most proximal slice). On average, the deviatoric stress change in trabecular bone (with respect to the intact state) with the hollow-stemmed implant was less than with the solid-stemmed implant by $1.7\% \pm 0.2\%$, $1.3\% \pm 0.1\%$, and $1.1\% \pm 0.1\%$ for healthy, average, and osteoporotic bone material properties, respectively (all $p \leq 0.001$). Also, considering the average deviatoric change in stress across the proximal trabecular bone, significant differences were found in results attained using different bone material properties, for both the solid and hollow stem implants (all $p \leq 0.05$). The largest differences in deviatoric changes in the overall average trabecular stress tensor occurred between the results for the hollow-stemmed implant, whose deviatoric stress change with osteoporotic bone material properties were greater than when average bone material properties were used, by $3.8\% \pm 0.8\%$.

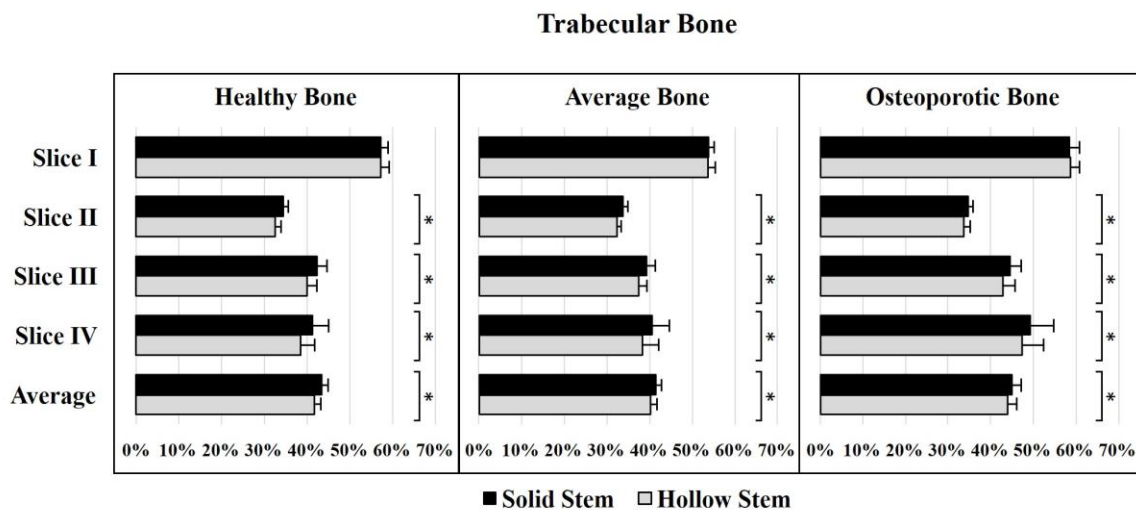


Figure 3.9 The volume-weighted average deviatoric component of the change in stress tensor for the reconstructed trabecular bone (as a percentage of its intact state (ΔS) for each bone condition and each stem design). Mean (+ standard deviation) stresses in each trabecular bone slices as well as the entire trabecular bone in the top 40 mm of the proximal humerus are presented (stresses are averaged over different loading configurations). * shows a significant difference between stems.

Initial Bone Response

Cortical region

On average, the percentage of cortical bone volume with the potential for bone resorption when an implant was used, ranged from $12.9\% \pm 1.2\%$ when the hollow-stemmed implant and healthy bone material properties were used to $17.0\% \pm 2.4\%$ when a solid-stemmed implant and osteoporotic bone material properties were simulated (Figure 3.10). Statistically significant differences were observed between solid- and hollow-stemmed implants for the average cortical bone and the most proximal slice across all the bone material properties. On average, the percentage of potentially resorbing cortical bone with the hollow-stemmed implant was less than with the solid-stemmed one by $3.0\% \pm 0.8\%$, $1.9\% \pm 0.6\%$, and $1.5\% \pm 0.4\%$ for healthy, average, and osteoporotic bone material properties, respectively (all $p \leq 0.01$). Also, using the solid-stemmed implant, the average percentage of potentially resorbing cortical bone for healthy bone material properties was greater than for the average bone material properties by $0.9\% \pm 0.3\%$ ($p \leq 0.03$). Using the hollow-stemmed implant, this resorbing volume percentage for osteoporotic bone material properties was larger than for the healthy bone material properties by $2.5\% \pm 1.0\%$ ($p \leq 0.05$).

The average percentage of potentially forming cortical bone when an implant was used, ranged from $0.5\% \pm 0.2\%$ when the hollow-stemmed implant and average bone material properties were used to $1.0\% \pm 0.3\%$ when a solid-stemmed implant and healthy bone material properties were simulated (Figure 3.10). On average, the percentage of potentially forming cortical bone with the hollow-stemmed implant was less than with the solid-stemmed one by $0.3\% \pm 0.09\%$, $0.2\% \pm 0.1\%$, and $0.3\% \pm 0.1\%$ for healthy, average, and osteoporotic bone material properties, respectively (all $p \leq 0.04$). Moreover, using the solid-stemmed implant, the average percentage of potentially forming cortical bone for healthy bone material properties was greater than for the average bone material properties by $0.4\% \pm 0.06\%$ ($p \leq 0.01$).

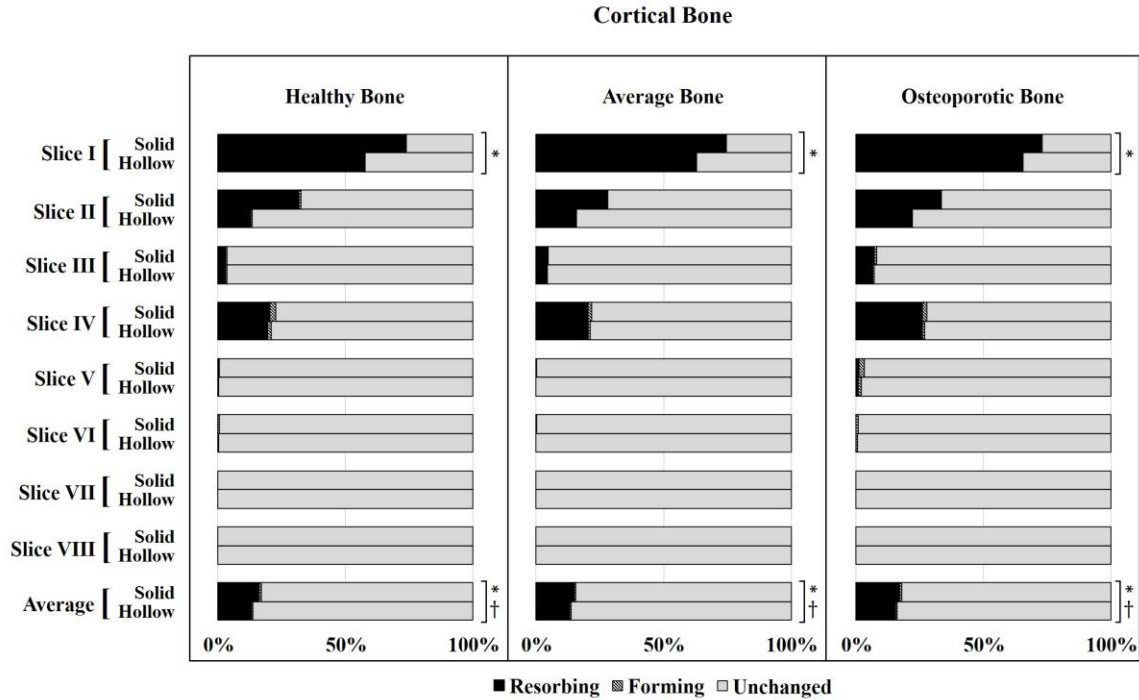


Figure 3.10 The percentage of cortical bone volume with the resorption/formation potential for each bone condition and each stem design. The volume percentage of remodeling bone in each cortical bone slices, as well as the entire cortical bone in the top 80 mm of the proximal humerus, are presented (results are averaged over different loading configurations). */† shows a significant difference in the resorption/formation potential between stems.

Trabecular region

On average, the percentage of trabecular bone volume with the potential for bone resorption when an implant was used, ranged from $16.6\% \pm 1.4\%$ when the hollow-stemmed implant and average bone material properties were used to $23.8\% \pm 1.9\%$ when a solid-stemmed implant with osteoporotic bone material properties was simulated (Figure 3.11). Statistically significant differences were observed between solid- and hollow-stemmed implants for the average trabecular bone, slice 1, and slice 2 across all the bone material properties (except for the second slice of the osteoporotic bone). On average, the percentage of potentially resorbing trabecular bone with the hollow-stemmed implant was less than with the solid-stemmed one by $2.0\% \pm 0.4\%$, $1.5\% \pm 0.2\%$, and $1.1\% \pm 0.4\%$ for

healthy, average, and osteoporotic bone material properties, respectively (all $p \leq 0.01$). Also, for average trabecular bone, significant differences were observed in results obtained using different bone material properties, for both the solid- and hollow-stemmed implants (all $p \leq 0.02$). The largest differences in the overall average percentage of potentially resorbing trabecular bone occurred between the results for the hollow-stemmed implant, whose percentage of potentially resorbing bone with osteoporotic bone material properties were greater than when average bone material properties were used, by $6.2\% \pm 0.9\%$.

The average percentage of potentially forming trabecular bone when an implant was used, ranged from $9.3\% \pm 0.7\%$ when the solid-stemmed implant and healthy bone material properties were used to $13.5\% \pm 0.7\%$ when a hollow-stemmed implant with osteoporotic bone material properties was simulated (Figure 3.11). On average, the percentage of potentially forming trabecular bone with the hollow-stemmed implant was more than with the solid-stemmed one by $0.4\% \pm 0.1$ for average bone material properties ($p \leq 0.01$). Moreover, for average trabecular bone, significant differences were observed in results attained using different bone material properties, for both the solid- and hollow-stemmed implants (all $p \leq 0.01$). The largest differences in the overall average percentage of potentially forming trabecular bone occurred between the results for the solid-stemmed implant, whose percentage of potentially forming bone with osteoporotic bone material properties were greater than when healthy bone material properties were used, by $4.1\% \pm 0.3\%$.

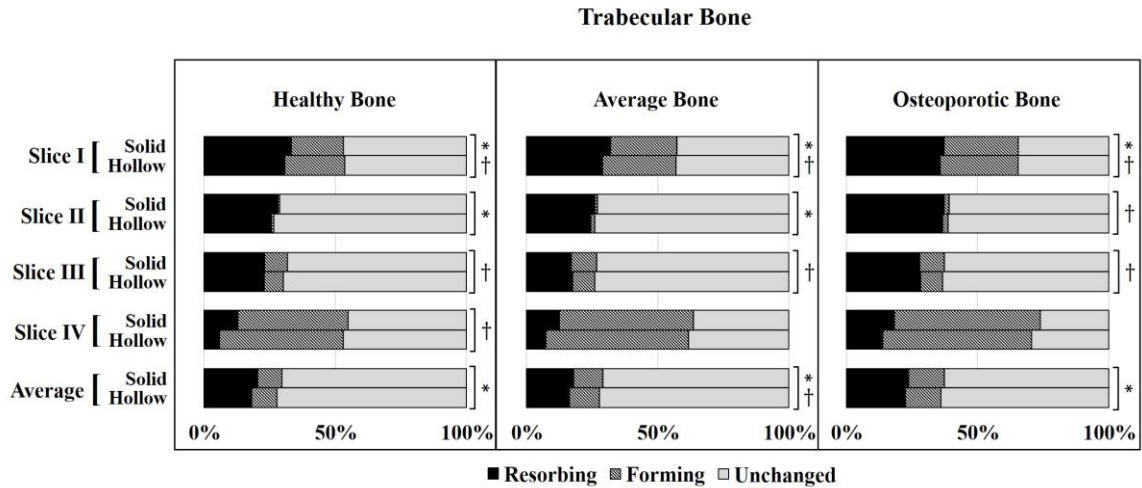


Figure 3.11 The percentage of trabecular bone volume with the resorption/formation potential for each bone condition and each stem design. The volume percentage of remodeling bone in each trabecular bone slices, as well as the entire trabecular bone in the top 40 mm of the proximal humerus, are presented (results are averaged over different loading configurations). */† shows a significant difference in the resorption/formation potential between stems.

Stem Stress

The maximum stem stress was identified for the hollow stem with healthy bone material properties at 120° of flexion, which was about 20 MPa. Therefore, stem stress levels remained well below the yield stress of titanium (about 1100 MPa) [171] for both the solid and hollow stems and all the loading configurations and bone material properties.

3.4 Discussion

The primary objective of this computational study was to quantify the ability of hollow-stemmed titanium implants to limit stress shielding at the proximal humerus for bones with different material properties representing healthy, average and osteoporotic bone conditions in comparison with otherwise identical but solid-stemmed implants. After developing corresponding FE models for intact and reconstructed bones with the solid- and hollow-stemmed implants, three different outcome measures were evaluated. Subsequently, significant differences between healthy, osteopenic, and osteoporotic bones with respect to various FE outcomes were noted.

Considering changes in the magnitude of von Mises stresses following TSA ($\Delta\sigma_{VWA}$), our results confirmed the hypothesis that hollow TSA implant stems would result in stresses that better mimic the intact state in comparison with solid stems, especially for the healthy bone. This measure only considers changes in the magnitude of von Mises (deviatoric) stress and is blind to changes in the direction of stress. However, it can indicate whether the stresses are increasing or decreasing. For cortical bone, it was observed that using a humeral stem implant decreases von Mises stress (σ_{VWA}) with respect to intact values (up to 34.4%), with a more pronounced effect at more proximal slices. These changes are believed to occur as a result of the majority of the load being borne through the stem instead of cortical bone, due to its higher stiffness. However, near the tip of the stem, the load transfers into the cortical bone, nearly matching the stresses there for the intact state. For the most proximal slice, using a hollow-stemmed implant instead of a solid-stemmed one could decrease $\Delta\sigma_{VWA}$ for cortical bone up to 3.2% of intact values for the humerus with healthy bone material properties. Regarding the trabecular bone, similarly, stress levels decreased with respect to the intact state after bone reconstruction except for the most proximal slice of the osteoporotic bone in 45 degrees of abduction and 90 degrees of flexion. This opposing trend can be partially attributed to the lower load-bearing capability of osteoporotic trabecular bone in its intact state, and altered loading distribution following TSA from peripheral cortical shell toward the central stem and surrounding trabecular bone in the most proximal slice. At this level, use of a hollow-stemmed implant instead of one with a solid stem reduced $\Delta\sigma_{VWA}$ for trabecular bone up to 4.0% of intact values for the

humerus with healthy bone material properties. On average, the decline in stress for trabecular bone was more pronounced than for cortical bone.

Considering the deviatoric component of the change in stress tensor (ΔS), as anticipated, hollow-stemmed implants were able to reduce change in stress to some extent over solid-stemmed designs. This measure only recognizes the deviatoric component of the stress changes and cannot specify if stress levels are increasing or decreasing hydrostatically. However, ΔS quantifies changes in the direction of stress and together with the aforementioned measure, we can better quantify changes in stress levels following TSA. For cortical bone, following TSA, a ΔS of 44.7% was measured in the most proximal slice. For this bone, on average, a hollow-stemmed implant reduced ΔS up to 1.6% of intact values over a solid-stemmed one. For trabecular bone, stress changes of up to 58.5% were noticed in the most proximal slice with respect to the intact state, showing more pronounced ΔS in comparison with cortical bone results. For this bone, on average, the hollow-stemmed implant mitigated ΔS up to 1.7% of intact values compared to the solid-stemmed one.

Moreover, as anticipated, osteoporotic bone experienced more marked ΔS over other bone conditions, implying more pronounced bone remodeling for this bone material properties. For cortical bone, on average, using the solid-stemmed/hollow-stemmed implant, the average ΔS for osteoporotic bone was greater than for healthy bone by 2.0% / 2.5% of intact values. For trabecular bone, on average, using the solid-stemmed/hollow-stemmed implant, the average ΔS for osteoporotic bone was greater than for the average bone by 3.6% / 3.8% of intact values.

In terms of initial bone response following TSA, results confirmed the hypothesis of reduced bone resorption potential for hollow-stemmed implants compared to the solid-stemmed ones. For cortical bone, up to 74.6% of the most proximal slice showed a potential for resorption, which shows the severity of stress shielding for this region. In this slice, hollow-stemmed implants marginally outperformed solid-stemmed ones through reducing bone volume with resorption potential by up to 3.0%. Regarding the trabecular bone, up to 37.2% of the bone in the most proximal slice presented resorption potential. On average,

the percentage of trabecular bone volume with resorption potential reduced by up to 2.0% by replacing solid-stemmed implants with hollow-stemmed ones. However, generally, the percentage of trabecular bone with resorption potential was still more than that of potential with formation.

Moreover, as anticipated, there was higher bone resorption potential for osteoporotic bone compared to other bone material properties. For cortical bone, on average, the percentage of bone with resorption potential for the osteoporotic bone material properties was greater than for the healthy bone material properties by up to 2.5%. For trabecular bone, on average, the percentage of bone with resorption potential for the osteoporotic bone material properties was greater than for the average bone material properties by up to 6.2%. However, for trabecular bone, the percentage of bone with formation potential for the osteoporotic bone material properties was greater than for the healthy bone material properties by up to 4.1%. This can be explained by the lower load-bearing capability of osteoporotic trabecular bone in its intact state, and more pronounced increase in its loading following TSA. Loads will be shifted from peripheral cortical shell toward the central stem and surrounding trabecular bone due to higher stiffness of stem compared to the cortical shell. This pronounced increase in loads could encourage bone formation for osteoporotic bone.

The results of this study, generally, agree well with results of other studies reported in the literature considering stress shielding due to implants at the shoulder, wrist and hip, which have indicated that increasing the compliance of stems can lead to bone stresses that better match the intact state of long bones. Utilizing FE modeling, Razfar [51] found that increasing the compliance of humeral stems yields humeral stresses that better mimic the intact stress distribution in cortical bone. In her study, PEEK stem, which has higher compliance compared to titanium and cobalt-chrome stems, outperformed the other two stems through reducing changes in the cortical bone stresses and better mimicking the intact state of the bones. By using FE simulations and *in vitro* experiments, Austman et al. [152], [172] observed less stress shielding at the ulna using more compliant titanium short stems instead of stainless steel and cobalt-chrome short stems. Using FE modeling, Gross et al. [158] achieved cortical stresses that better mimicked the intact state of the femur by

using a cylindrical hollow-stemmed cemented hip implant. They could elevate proximal cortical bone stress levels up to 28% by using a cylindrical hollow stem with an inner-wall thickness of 1mm (the same inner-wall thickness was used in our study) relative to a solid stem with similar outer diameter. The gains of the hollow stem immediately reduced by moving distally along the stem in agreement with our results. They further increased proximal cortical bone stresses by another 5% by optimizing the design of their hollow stem. They also concluded that reducing the inner-wall thickness of a hollow stem as well as its Young's modulus can reduce the stress shielding. Similarly, in a clinical study of 40 implantations of cementless hollow femoral stems, Schmidt et al. [159] found promising clinical results regarding the reduction of stress shielding at the proximal femur using hollow stems. Moreover, a FE analysis by Mattheck et al. [160] demonstrated a significant increase in proximal cortical femur stresses up to 20% by using hollow stems.

Our study is limited in its simulation of *in vivo* loading configurations. Only four loading scenarios were considered based on telemetered shoulder prosthesis data of Bergmann et al. [28] to represent common arm motions during activities of daily living. Also, for modeling material properties of trabecular bones, a modulus-density relationship pooled from different anatomic sites was used [48] as no humerus-specific equation has been derived to this date. Yet, Reeves et al. [78] demonstrated a low variability induced by changing the trabecular stiffness relationship for the outcome measures investigated in our study. Another limitation of this work is idealizing the bone-implant interface. However, it enabled element-by-element comparisons of FE outcome measures for the intact and reconstructed bones due to one-to-one mesh correspondence outside of where cropping/reaming occurred. Moreover, one-to-one *in vitro* validation was not possible in our study, as artificial population-averaged CT images were used to develop the finite element models. However, *in vitro* experiments can only quantify changes in peripheral strain distributions and overall deflections and are limited in strain gauging at isolated locations. FE simulations like this can provide valuable insights into the complex three-dimensional distribution of stresses at every location across the bone noninvasively and be beneficial for parametric comparisons as performed herein. One of the strengths of this study was developing models that represent a population of 75 humeri while keeping the

mesh and material properties consistent across intact and reconstructed bones allowing for direct comparisons of results for a variety of bone qualities.

While the improvements in the bone-implant mechanics of hollow versus solid stems for femur seem promising, our results suggest a marginal enhancement for the humerus, for which osteoporosis can exacerbate stress shielding to some extent, regardless of stem design. One of the interesting findings of this study is that healthy and possibly younger patients who undergo TSA may benefit more from using more compliant stems than do osteoporotic patients. By making stems hollow, the stem stresses remained well below the yield stress of titanium for all bone material properties and loading conditions, suggesting that further increasing the compliance of these stems can be achieved. By adding pores or reducing the inner-wall thickness of short stems, possibly by using optimization techniques, their performance may be improved.

Chapter 4

4 Summary and Future Works

This chapter recapitulates the objectives, answers to the hypotheses of this work, and techniques used to achieve those objectives. This will be followed by a description of the strengths and limitations that arose throughout this study. Finally, the future directions and the significance of this work in improving the population-based design of shoulder prostheses are discussed.

4.1 Summary

Over the past decades, the number of TSA procedures has been increasing rapidly with the most rapid growth among all human joint replacements leading to a projected seven-fold increase in their incidences over the next decade [4]–[6]. This rising number can be attributed to their success in relieving pain, and restoring the natural ROM to an arthritic shoulder joint [1]–[3]. However, there are complications associated with TSA, including the stress shielding of proximal bone following its reconstruction, which can stimulate adaptive bone remodeling [8]–[10]. This phenomenon can be exaggerated for patients suffering from concurrent osteoporosis [8], [11]–[13].

A better understanding of how the shape and density of the shoulder vary among members of a population can help design more effective population-based orthopedic implants. The first objective of this study was to develop SSMs and SDMs for the shoulder serving as tools to describe the main modes of variability in the shape and density distributions of bones within the population of interest expressed as a set of parameters called PCs. These PCs were further analyzed and significant correlations observed between the shape and density distributions of the shoulder and demographics of the population, such as sex and age. It was concluded that age has a significant inverse effect on the density within the entire shoulder, with a pronounced effect for females. This effect implied a natural bone density loss of the shoulder with aging. Moreover, our results demonstrated that males, on average, have larger humeri and scapulae with thicker cortical bones than females based on observed significant differences in PCs of the shoulder SSMs and SDMs between sexes.

Also, it was shown that significant correlations exist between many modes of shape and density variations in the shoulder. Finally, while contralateral bone shapes were found to be symmetric, asymmetry, to some extent, was noted regarding their bone density distributions. These results encourage the use of contralateral bones as templates for shoulder reconstruction and can also help guide designs of population-based prostheses.

Use of more compliant stems (e.g., hollow-stemmed implants or implants manufactured from less stiff materials like porous titanium) could mitigate the effect of stress shielding, and consequently reduce needs for revision surgeries [152], [158]–[161], [172]. Recent advances in AM have enabled the production of titanium alloy parts with complex geometries, such as hollow stems [156], [157]. The second objective of this study was to determine if such hollow titanium stems can mitigate stress shielding at the proximal humerus for a variety of bone qualities, using finite element methods. While the improvements in the bone-implant mechanics of hollow versus solid stems for femurs seemed promising [158], [160], [161], our results suggested a marginal improvement for the humerus, for which osteoporosis could exacerbate stress shielding to some extent, regardless of stem design. One of the interesting findings of this study was that healthy and possibly younger patients who undergo TSA might benefit more from using more compliant stems than do osteoporotic patients. By making stems hollow, the stem stresses remained well below the yield stress of titanium for all bone material properties and loading conditions, suggesting that further increasing the compliance of these stems can be achieved, which may be beneficial. For instance, adding pores to the walls, or reducing the inner-wall thickness of stems, possibly using optimization techniques, may improve their performance and further limit stress shielding and bone resorption.

4.2 Limitations and Strengths

Regarding the first objective of this work, our study is limited by the number of specimens and their age range (mean 73 ± 13). However, the sensitivity of our results to the number of included specimens was investigated through a robustness study (Appendix C). In the future, by including younger specimens, we will be able to further investigate the effect of age on the density distribution of the shoulder. Another limitation was that 71 out of 75

specimens were from donors of Caucasian ethnicity. Including specimens from other ethnicities in future studies would allow us to also investigate the effect of this factor on the shape and density distribution of the bones. The lack of compactness of the SDMs, compared to our SSMs, is a limitation. However, the SDMs could still successfully reconstruct all the specimens in our set and capture the pattern of their density distribution effectively using a small set of PCs (6 PCs for the humerus and 14 PCs for the scapula) (Appendix A). In future works, it may be advantageous to develop scapula SDMs that solely focus on particular areas of interest (e.g., the glenoid), as including the density distribution of the bone in all of its regions may not be of use while limiting the compactness of our model. Furthermore, the SSM only considered the outer cortex of the bones. In future studies, including the inner cortical shell as a shape parameter, may be more effective than incorporating it as a bone density distribution parameter resulting in more compact SDMs. However, it will likely increase variability in the SSMs.

Regarding the second objective of this work, our study is limited in its simulation of *in vivo* loading configurations. Only four loading scenarios were considered based on telemetered shoulder prosthesis data of Bergmann et al. [28] to represent common arm motions during activities of daily living. Another limitation was that a modulus-density relationship pooled from different anatomic sites was used [48] to model material properties of trabecular bones, as no humerus-specific equation has been derived to this date. Yet, Reeves et al. [78] demonstrated a low variability induced by changing the trabecular stiffness relationship for the outcome measures investigated in our study. Moreover, one-to-one *in vitro* validation was not possible in our study, as artificial population-averaged CT images were used to develop the finite element models. However, *in vitro* experiments can only quantify changes in peripheral strain distributions and overall deflections and are limited in strain gauging at isolated locations. FE simulations like this can provide valuable insights into the complex three-dimensional distribution of stresses at every location across the bone noninvasively and be beneficial for parametric comparisons as performed herein. One of the strengths of this study was developing models that represent a population of 75 humeri while keeping the mesh and material properties consistent across intact and reconstructed bones allowing for direct comparisons of results for a variety of bone qualities. Moreover, careful mesh planning resulted in identical surrounding bone meshes

with one-to-one mesh correspondence outside of where cropping/reaming occurred for the intact and reconstructed bones. This mesh correspondence was then leveraged for element-by-element comparisons of FE outcome measures between intact and reconstructed bones with solid and hollow stems.

4.3 Future Directions

Since our results indicate making stems hollow is safe, as the stem stress levels remained well below the yield stress of titanium, it can be inferred that further increasing the compliance of these stems can be advantageous. Hollow [158], [160], [161] or porous [173] stems have been explored for the stem components of hip implants, but not both simultaneously. Although no such study for shoulder implants has been documented yet, hollow porous stems produced using AM can be an attractive solution to further reduce stress shielding at the proximal humerus. One interesting future study would be to optimize the design of hollow and porous stems to minimize stress shielding while also addressing manufacturability and cost constraints associated with AM. Furthermore, the hollow design of stems can potentially be leveraged for drug delivery.

In order to achieve these future optimization objectives, a parametric model of the shoulder stem should be developed first. The current hollow design of the stem can be a suitable start point for this purpose. Essential design features such as stem length, width, aspect ratio, curvature, inner-wall thickness, and pore boundaries across the surface geometry will be defined parametrically to facilitate future customizations. Parametric analyses will be performed in order to examine the influence of pore size, distribution and inner-wall thickness on stress shielding. We anticipate that larger pore sizes, especially more proximally, and thinner inner-walls will further limit stress shielding. Moreover, changes in cortical surface strains following reconstruction will be measured at predefined locations to validate the model against *in vitro* tests. Similar to the current study, an FE model of a cadaveric humerus will be developed, and subsequently, the *in vitro* test can be performed on it. The cadaveric humerus upon which FE was developed will be denuded of all soft tissues, transected proximal to the elbow, and potted distally in a custom fixture using dental stone. The potted bone will be mounted to six degrees of freedom joint motion simulator (AMTI VIVO) to apply the simulated loads. Strain gauges will be placed at the

same locations as where surface strains were measured using the FE model. *In silico* predicted and measured *in vitro* strains for the intact humerus will be directly compared. Subsequently, the bone will be cropped and reamed to act as the host for a candidate implant. Next, the stem will be implanted into the bone and loaded. Measured surface strains will be compared with intact values, and with corresponding values computed *in silico*. We anticipate that the relative strain levels for the intact and reconstructed humerus will agree with FE predictions, although absolute strains may not be the same.

4.4 Significance

To the author's best knowledge this is the first study developing an SSDM for both of the corresponding shoulder bones (humerus, and scapula) and finding the correlations between the main modes of variability in the shape and density distributions of these bones within a population of interest, and demographic data of that population such as sex and age. Also, this is the first study on the hollow stems for shoulder implants. The results of this study encourage the use of more compliant stems for TSA implants, e.g., hollow porous stems, especially for patients without signs of metabolic bone diseases, to limit stress shielding at the proximal humerus. An exacerbation of the stress shielding problem was found for patients who suffer from concurrent osteoporosis for which SSDM can be leveraged to optimize the performance of implants specifically designed for such a population. Together, the results of this work can pave the way for improving the population-based design of shoulder prostheses.

References

- [1] W. P. Barrett, J. L. Franklin, S. E. Jackins, C. R. Wyss, and F. A. Matsen III, "Total shoulder arthroplasty," *J. Bone Jt. Surg.*, vol. 69, no. 6, pp. 865–872, 1987.
- [2] T. R. Norris and J. P. Iannotti, "Functional outcome after shoulder arthroplasty for primary osteoarthritis: A multicenter study," *J. Shoulder Elb. Surg.*, vol. 11, no. 2, pp. 130–135, 2002.
- [3] B. A. Goldberg, K. Smith, S. Jackins, B. Campbell, and F. A. Matsen, "The magnitude and durability of functional improvement after total shoulder arthroplasty for degenerative joint disease," *J. Shoulder Elb. Surg.*, vol. 10, no. 5, pp. 464–469, 2001.
- [4] V. T. Deore, E. Grif, and P. Monga, "Journal of Arthroscopy and Joint Surgery Shoulder arthroplasty — Past , present and future," vol. 5, pp. 3–8, 2018.
- [5] S. H. Kim, B. L. Wise, Y. Zhang, and R. M. Szabo, "Increasing incidence of shoulder arthroplasty in the United States," *J. Bone Jt. Surg. - Ser. A*, vol. 93, no. 24, pp. 2249–2254, 2011.
- [6] W. W. Schairer, B. U. Nwachukwu, S. Lyman, E. V. Craig, and L. V. Gulotta, "National utilization of reverse total shoulder arthroplasty in the United States," *J. Shoulder Elb. Surg.*, vol. 24, no. 1, pp. 91–97, 2015.
- [7] J. S. Day, E. Lau, K. L. Ong, G. R. Williams, M. L. Ramsey, and S. M. Kurtz, "Prevalence and projections of total shoulder and elbow arthroplasty in the United States to 2015," *J. Shoulder Elb. Surg.*, vol. 19, no. 8, pp. 1115–1120, 2010.
- [8] J. Nagels, M. Stokdijk, and P. M. Rozing, "Stress shielding and bone resorption in shoulder arthroplasty," *J. Shoulder Elb. Surg.*, vol. 12, no. 1, pp. 35–39, 2003.
- [9] K. Inoue *et al.*, "Humeral bone resorption after anatomic shoulder arthroplasty using an uncemented stem," *J. Shoulder Elb. Surg.*, vol. 26, no. 11, pp. 1984–1989, 2017.
- [10] C. Spormann *et al.*, "Patterns of proximal humeral bone resorption after total shoulder arthroplasty with an uncemented rectangular stem," *J. Shoulder Elb. Surg.*, vol. 23, no. 7, pp. 1028–1035, 2014.
- [11] K. Pervaiz, A. Cabezas, K. Downes, B. G. Santoni, and M. A. Frankle, "Osteoporosis and shoulder osteoarthritis: Incidence, risk factors, and surgical implications," *J. Shoulder Elb. Surg.*, vol. 22, no. 3, p. e1, 2013.
- [12] J. Glowacki and T. S. Thornhill, "Osteoporosis and Osteopenia in Patients with Osteoarthritis," *Ortho Rheum Open Access J*, vol. 2, no. 3, pp. 555–590, 2016.
- [13] J. H. Healey, V. J. Vigorita, and J. M. Lane, "The coexistence and characteristics of osteoarthritis and osteoporosis.," *J. Bone Joint Surg. Am.*, vol. 67, no. 4, pp. 586–592, 1985.
- [14] L. U. Bigliani, R. Kelkar, E. L. Flatow, R. G. Pollock, and V. C. Mow, "Glenohumeral stability: biomechanical properties of passive and active

- stabilizers,” *Clin. Orthop. Relat. Res.*, vol. 330, pp. 13–30, 1996.
- [15] E. Culham and M. Peat, “Functional anatomy of the shoulder complex,” *J. Orthop. Sport. Phys. Ther.*, vol. 18, no. 1, pp. 342–350, 1993.
- [16] C. A. Rockwood, *The shoulder*, vol. 1. Elsevier Health Sciences, 2009.
- [17] G. Betts *et al.*, “Anatomy and Physiology,” *OpenStax*, 2013. [Online]. Available: <https://openstax.org/books/anatomy-and-physiology/pages/1-6-anatomical-terminology>.
- [18] K.-N. An, A. O. Browne, S. Korinek, S. Tanaka, and B. F. Morrey, “Three-dimensional kinematics of glenohumeral elevation,” *J. Orthop. Res.*, vol. 9, no. 1, pp. 143–149, 1991.
- [19] L. A. Curl and R. F. Warren, “Glenohumeral joint stability: selective cutting studies on the static capsular restraints,” *Clin. Orthop. Relat. Res.*, vol. 330, pp. 54–65, 1996.
- [20] A. M. Halder, C. G. Halder, K. D. Zhao, S. W. O’Driscoll, B. F. Morrey, and K. N. An, “Dynamic inferior stabilizers of the shoulder joint,” *Clin. Biomech.*, vol. 16, no. 2, pp. 138–143, 2001.
- [21] A. R. Karduna, G. R. Williams, J. P. Iannotti, and J. L. Williams, “Kinematics of the glenohumeral joint: influences of muscle forces, ligamentous constraints, and articular geometry,” *J. Orthop. Res.*, vol. 14, no. 6, pp. 986–993, 1996.
- [22] S. Lippitt and F. Matsen, “Mechanisms of glenohumeral joint stability,” *Clin. Orthop. Relat. Res.*, no. 291, pp. 20–28, 1993.
- [23] C. Anglin, U. P. Wyss, and D. R. Pichora, “Glenohumeral contact forces,” *Proc. Inst. Mech. Eng. Part H J. Eng. Med.*, vol. 214, no. 6, pp. 637–644, 2000.
- [24] A. Conzen and F. Eckstein, “Quantitative determination of articular pressure in the human shoulder joint,” *J. Shoulder Elb. Surg.*, vol. 9, no. 3, pp. 196–204, 2000.
- [25] A. R. Hopkins, U. N. Hansen, A. A. Amis, M. Taylor, and R. J. Emery, “Glenohumeral kinematics following total shoulder arthroplasty: a finite element investigation,” *J. Orthop. Res.*, vol. 25, no. 1, pp. 108–115, 2007.
- [26] A. Terrier, S. Ramondetti, F. Merlini, D. D. Pioletti, and A. Farron, “Biomechanical consequences of humeral component malpositioning after anatomical total shoulder arthroplasty,” *J. Shoulder Elb. Surg.*, vol. 19, no. 8, pp. 1184–1190, 2010.
- [27] F. C. T. der Helm, “A finite element musculoskeletal model of the shoulder mechanism,” *J. Biomech.*, vol. 27, no. 5, pp. 551–569, 1994.
- [28] G. Bergmann, F. Graichen, A. Bender, M. Kääh, A. Rohlmann, and P. Westerhoff, “In vivo glenohumeral contact forces-Measurements in the first patient 7 months postoperatively,” *J. Biomech.*, vol. 40, no. 10, pp. 2139–2149, 2007.
- [29] B. Bolsterlee, D. H. E. J. Veeger, and E. K. Chadwick, “Clinical applications of musculoskeletal modelling for the shoulder and upper limb,” *Med. Biol. Eng. Comput.*, vol. 51, no. 9, pp. 953–963, 2013.

- [30] V. T. Inman, J. B. deC M. Saunders, and L. C. Abbott, "Observations on the function of the shoulder joint," *JBJS*, vol. 26, no. 1, pp. 1–30, 1944.
- [31] S. A. Hess, "Functional stability of the glenohumeral joint," *Man. Ther.*, vol. 5, no. 2, pp. 63–71, 2000.
- [32] D. C. Ackland and M. G. Pandy, "Moment arms of the shoulder muscles during axial rotation," *J. Orthop. Res.*, vol. 29, no. 5, pp. 658–667, 2011.
- [33] A. D. P. Bankoff, "Biomechanical characteristics of the bone," *Hum. Musculoskelet. Biomech.*, vol. 61, p. 86, 2012.
- [34] H. Gray, L. H. Bannister, M. M. Berry, and others, "Gray's Anatomy: The anatomical basis of medicine and surgery 38th ed," *Churchill Livingstone, Edinburgh*, pp. 443–452, 1995.
- [35] S. H. Ralston, "Bone structure and metabolism," *Medicine (Baltimore)*, vol. 45, no. 9, pp. 560–564, 2017.
- [36] J. Wolff, "Das gesetz der transformation der knochen," *DMW-Deutsche Medizinische Wochenschrift*, vol. 19, no. 47, pp. 1222–1224, 1893.
- [37] R. Huiskes, H. Weinans, H. J. Grootenboer, M. Dalstra, B. Fudala, and T. J. Slooff, "Adaptive bone-remodeling theory applied to prosthetic-design analysis," *J. Biomech.*, vol. 20, no. 11–12, pp. 1135–1150, 1987.
- [38] S. C. Cowin and D. H. Hegedus, "Bone remodeling I: theory of adaptive elasticity," *J. Elast.*, vol. 6, no. 3, pp. 313–326, 1976.
- [39] D. J. Hadjidakis and I. I. Androulakis, "Bone remodeling," *Ann. N. Y. Acad. Sci.*, vol. 1092, no. 1, pp. 385–396, 2006.
- [40] B. Clarke, "Normal bone anatomy and physiology," *Clin. J. Am. Soc. Nephrol.*, vol. 3, no. Supplement 3, pp. S131–S139, 2008.
- [41] G. Osterhoff, E. F. Morgan, S. J. Shefelbine, L. Karim, L. M. McNamara, and P. Augat, "Bone mechanical properties and changes with osteoporosis," *Injury*, vol. 47, pp. S11–S20, 2016.
- [42] C. Zannoni, R. Mantovani, and M. Viceconti, "Material properties assignment to finite element models of bone structures: a new method," *Med. Eng. Phys.*, vol. 20, no. 10, pp. 735–740, 1999.
- [43] R. L. Austman, J. S. Milner, D. W. Holdsworth, and C. E. Dunning, "Development of a customized density—modulus relationship for use in subject-specific finite element models of the ulna," *Proc. Inst. Mech. Eng. Part H J. Eng. Med.*, vol. 223, no. 6, pp. 787–794, 2009.
- [44] D. R. Carter and W. C. Hayes, "The compressive behavior of bone as a two-phase porous structure.," *J. Bone Joint Surg. Am.*, vol. 59, no. 7, pp. 954–962, 1977.
- [45] A. S. O. Leung, L. M. Gordon, T. Skrinskas, T. Szwedowski, and C. M. Whyne, "Effects of bone density alterations on strain patterns in the pelvis: application of a finite element model," *Proc. Inst. Mech. Eng. Part H J. Eng. Med.*, vol. 223, no. 8, pp. 965–979, 2009.

- [46] E. Schileo, F. Taddei, A. Malandrino, L. Cristofolini, and M. Viceconti, "Subject-specific finite element models can accurately predict strain levels in long bones," *J. Biomech.*, vol. 40, no. 13, pp. 2982–2989, 2007.
- [47] F. Taddei, L. Cristofolini, S. Martelli, H. S. Gill, and M. Viceconti, "Subject-specific finite element models of long bones: an in vitro evaluation of the overall accuracy," *J. Biomech.*, vol. 39, no. 13, pp. 2457–2467, 2006.
- [48] E. F. Morgan, H. H. Bayraktar, and T. M. Keaveny, "Trabecular bone modulus-density relationships depend on anatomic site," *J. Biomech.*, vol. 36, no. 7, pp. 897–904, 2003.
- [49] W. A. Wallace, *Joint replacement in the shoulder and elbow*. Butterworth-Heinemann Oxford, 1998.
- [50] I. I. CHARLES S NEER, "Replacement arthroplasty for glenohumeral osteoarthritis," *JBJS*, vol. 56, no. 1, pp. 1–13, 1974.
- [51] N. Razfar, "Finite Element Modeling of the Proximal Humerus to Compare Stemless , Short and Standard Stem Humeral Components of Varying Material Stiffness for Shoulder Arthroplasty," *Univ. West. Ontario - Electron. Thesis Diss. Repos.*, vol. 2431, no. October, pp. 1–138, 2014.
- [52] P. Boileau, R. J. Sinnerton, C. Chuinard, and G. Walch, "Arthroplasty of the shoulder," *J. Bone Joint Surg. Br.*, vol. 88, no. 5, pp. 562–575, 2006.
- [53] H. Derar and M. Shahinpoor, "Recent patents and designs on hip replacement prostheses," *Open Biomed. Eng. J.*, vol. 9, p. 92, 2015.
- [54] L. Harmer, T. Throckmorton, and J. W. Sperling, "Total shoulder arthroplasty: are the humeral components getting shorter?," *Curr. Rev. Musculoskelet. Med.*, vol. 9, no. 1, pp. 17–22, 2016.
- [55] P. W. Jost, J. S. Dines, M. H. Griffith, M. Angel, D. W. Altchek, and D. M. Dines, "Total shoulder arthroplasty utilizing mini-stem humeral components: technique and short-term results," *HSS Journal®*, vol. 7, no. 3, pp. 213–217, 2011.
- [56] J. D. Keener, P. N. Chalmers, and K. Yamaguchi, "The humeral implant in shoulder arthroplasty," *JAAOS-Journal Am. Acad. Orthop. Surg.*, vol. 25, no. 6, pp. 427–438, 2017.
- [57] A. A. Romeo, R. J. Thorsness, S. A. Sumner, R. Gobezie, E. S. Lederman, and P. J. Denard, "Short-term clinical outcome of an anatomic short-stem humeral component in total shoulder arthroplasty," *J. shoulder Elb. Surg.*, vol. 27, no. 1, pp. 70–74, 2018.
- [58] D. R. Sumner, "Long-term implant fixation and stress-shielding in total hip replacement," *J. Biomech.*, vol. 48, no. 5, pp. 797–800, 2015.
- [59] R. B. Litchfield *et al.*, "Cemented versus uncemented fixation of humeral components in total shoulder arthroplasty for osteoarthritis of the shoulder: a prospective, randomized, double-blind clinical trial—A JOINTs Canada Project," *J. shoulder Elb. Surg.*, vol. 20, no. 4, pp. 529–536, 2011.

- [60] F. Schmidutz, Y. Agarwal, P. E. Müller, B. Gueorguiev, R. G. Richards, and C. M. Sprecher, "Stress-shielding induced bone remodeling in cementless shoulder resurfacing arthroplasty: a finite element analysis and in vivo results," *J. Biomech.*, vol. 47, no. 14, pp. 3509–3516, 2014.
- [61] P. Collin, T. Matsukawa, P. Boileau, U. Brunner, and G. Walch, "Is the humeral stem useful in anatomic total shoulder arthroplasty?," *Int. Orthop.*, vol. 41, no. 5, pp. 1035–1039, 2017.
- [62] P. J. Denard *et al.*, "Proximal stress shielding is decreased with a short stem compared with a traditional-length stem in total shoulder arthroplasty," *J. Shoulder Elb. Surg.*, vol. 27, no. 1, pp. 53–58, 2018.
- [63] F. Duparc, "Malunion of the proximal humerus," *Orthop. Traumatol. Surg. Res.*, vol. 99, no. 1, pp. S1–S11, 2013.
- [64] M. Schnetzke, S. Coda, P. Raiss, G. Walch, and M. Loew, "Radiologic bone adaptations on a cementless short-stem shoulder prosthesis," *J. shoulder Elb. Surg.*, vol. 25, no. 4, pp. 650–657, 2016.
- [65] D. J. Casagrande *et al.*, "Radiographic evaluation of short-stem press-fit total shoulder arthroplasty: short-term follow-up," *J. shoulder Elb. Surg.*, vol. 25, no. 7, pp. 1163–1169, 2016.
- [66] M. P. Morwood, P. S. Johnston, and G. E. Garrigues, "Proximal ingrowth coating decreases risk of loosening following uncemented shoulder arthroplasty using mini-stem humeral components and lesser tuberosity osteotomy," *J. shoulder Elb. Surg.*, vol. 26, no. 7, pp. 1246–1252, 2017.
- [67] N. Razfar, J. M. Reeves, D. G. Langohr, R. Willing, G. S. Athwal, and J. A. Johnson, "Comparison of proximal humeral bone stresses between stemless, short stem, and standard stem length: A finite element analysis," *J. Shoulder Elb. Surg.*, vol. 25, no. 7, pp. 1076–1083, 2016.
- [68] "Canadian Institute for Health Information," 2017. [Online]. Available: <https://www.cihi.ca/en/patient-cost-estimator>.
- [69] T. W. Bauer and J. Schils, "The pathology of total joint arthroplasty. I. Mechanisms of implant fixation.," *Skeletal Radiol.*, vol. 28, no. 8, pp. 423–432, 1999.
- [70] K. I. Bohsali, M. A. Wirth, and C. A. Rockwood Jr, "Complications of total shoulder arthroplasty," *JBJS*, vol. 88, no. 10, pp. 2279–2292, 2006.
- [71] P. Y. K. Chin, J. W. Sperling, R. H. Cofield, and C. Schleck, "Complications of total shoulder arthroplasty: are they fewer or different?," *J. shoulder Elb. Surg.*, vol. 15, no. 1, pp. 19–22, 2006.
- [72] O. Verborgt, R. El-Abiad, and D. F. Gazielly, "Long-term results of uncemented humeral components in shoulder arthroplasty," *J. shoulder Elb. Surg.*, vol. 16, no. 3, pp. S13–S18, 2007.
- [73] M. A. C. Neuert and C. E. Dunning, "Determination of remodeling parameters for a strain-adaptive finite element model of the distal ulna," vol. 227, no. 9, pp. 994–

1001, 2013.

- [74] R. Huiskes, R. Ronald, G. H. van Lenthe, and D. J. Jan, “Effects of mechanical forces on maintenance and adaptation of form in trabecular bone,” *Nature*, vol. 405, no. 6787, pp. 704–706, 2000.
- [75] I. G. Jang, I. Y. Kim, and B. M. Kwak, “Analogy of strain energy density based bone-remodeling algorithm and structural topology optimization,” *J. Biomech. Eng.*, vol. 131, no. 1, p. 11012, 2009.
- [76] H. Weinans, R. Huiskes, and H. J. Grootenboer, “The behavior of adaptive bone-remodeling simulation models,” *J. Biomech.*, vol. 25, no. 12, pp. 1425–1441, 1992.
- [77] D. R. Carter, D. P. Fyhrie, and R. T. Whalen, “Trabecular bone density and loading history: regulation of connective tissue biology by mechanical energy,” *J. Biomech.*, vol. 20, no. 8, pp. 785–794, 1987.
- [78] J. M. Reeves, G. S. Athwal, J. A. Johnson, and G. D. G. Langohr, “The Effect of Inhomogeneous Trabecular Stiffness Relationship Selection on Finite Element Outcomes for Shoulder Arthroplasty,” *J. Biomech. Eng.*, vol. 141, no. 3, p. 034501, 2018.
- [79] P. J. Laz and M. Browne, “A review of probabilistic analysis in orthopaedic biomechanics,” *Proc. Inst. Mech. Eng. Part H J. Eng. Med.*, vol. 224, no. 8, pp. 927–943, 2010.
- [80] N. Sarkalkan, H. Weinans, and A. A. Zadpoor, “Statistical shape and appearance models of bones,” *Bone*, vol. 60, pp. 129–140, 2014.
- [81] Y. M. Yang, D. Rueckert, and A. M. J. Bull, “Predicting the shapes of bones at a joint: application to the shoulder,” *Comput. Methods Biomech. Biomed. Engin.*, vol. 11, no. 1, pp. 19–30, 2008.
- [82] C. K. Fitzpatrick, M. A. Baldwin, P. J. Laz, D. P. FitzPatrick, A. L. Lerner, and P. J. Rullkoetter, “Development of a statistical shape model of the patellofemoral joint for investigating relationships between shape and function,” *J. Biomech.*, vol. 44, no. 13, pp. 2446–2452, 2011.
- [83] L. M. Smoger *et al.*, “Statistical modeling to characterize relationships between knee anatomy and kinematics,” *J. Orthop. Res.*, vol. 33, no. 11, pp. 1620–1630, 2015.
- [84] J. Fripp, S. Crozier, S. K. Warfield, and S. Ourselin, “Automatic segmentation of the bone and extraction of the bone--cartilage interface from magnetic resonance images of the knee,” *Phys. Med. Biol.*, vol. 52, no. 6, p. 1617, 2007.
- [85] M. A. Baldwin, J. E. Langenderfer, P. J. Rullkoetter, and P. J. Laz, “Development of subject-specific and statistical shape models of the knee using an efficient segmentation and mesh-morphing approach,” *Comput. Methods Programs Biomed.*, vol. 97, no. 3, pp. 232–240, 2010.
- [86] A. Rasoulian, R. Rohling, and P. Abolmaesumi, “Lumbar spine segmentation using a statistical multi-vertebrae anatomical shape+ pose model,” *IEEE Trans. Med. Imaging*, vol. 32, no. 10, pp. 1890–1900, 2013.

- [87] L. Kamer, H. Noser, A. W. Popp, M. Lenz, and M. Blauth, “Computational anatomy of the proximal humerus: An ex vivo high-resolution peripheral quantitative computed tomography study,” *J. Orthop. Transl.*, vol. 4, pp. 46–56, 2016.
- [88] H. Lamecker, M. Seebass, H.-C. Hege, and P. Deuflhard, “A 3D statistical shape model of the pelvic bone for segmentation,” in *Medical Imaging 2004: Image Processing*, 2004, vol. 5370, pp. 1341–1351.
- [89] T. Mutsvangwa, V. Burdin, C. Schwartz, and C. Roux, “An Automated Statistical Shape Model Developmental Pipeline: Application to the Human Scapula and Humerus,” *IEEE Trans. Biomed. Eng.*, vol. 62, no. 4, pp. 1098–1107, 2015.
- [90] J. Q. Campbell and A. J. Petrella, “Automated finite element modeling of the lumbar spine: Using a statistical shape model to generate a virtual population of models,” *J. Biomech.*, vol. 49, no. 13, pp. 2593–2599, 2016.
- [91] L. B. Querol, P. Büchler, D. Rueckert, L. P. Nolte, and M. Á. G. Ballester, “Statistical Finite Element Model for Bone Shape and Biomechanical Properties,” in *International Conference on Medical Image Computing and Computer-Assisted Intervention*, 2006, pp. 405–411.
- [92] R. Bryan, P. S. Mohan, A. Hopkins, F. Galloway, M. Taylor, and P. B. Nair, “Statistical modelling of the whole human femur incorporating geometric and material properties,” *Med. Eng. Phys.*, vol. 32, no. 1, pp. 57–65, 2010.
- [93] D. P. Nicoletta and T. L. Bredbenner, “Development of a parametric finite element model of the proximal femur using statistical shape and density modelling,” *Comput. Methods Biomech. Biomed. Engin.*, vol. 15, no. 2, pp. 101–110, 2012.
- [94] E. Schileo *et al.*, “An accurate estimation of bone density improves the accuracy of subject-specific finite element models,” *J. Biomech.*, vol. 41, no. 11, pp. 2483–2491, 2008.
- [95] S. Gupta and P. Dan, “Bone geometry and mechanical properties of the human scapula using computed tomography data,” *Trends Biomater Artif Organs*, vol. 17, no. 2, pp. 61–70, 2004.
- [96] C. K. Fitzpatrick, D. P. FitzPatrick, and D. D. Auger, “Size and shape of the resection surface geometry of the osteoarthritic knee in relation to total knee replacement design,” *Proc. Inst. Mech. Eng. Part H J. Eng. Med.*, vol. 222, no. 6, pp. 923–932, 2008.
- [97] J. J. Allred, C. Flores-Hernandez, H. R. Hoenecke Jr, and D. D. D’Lima, “Posterior augmented glenoid implants require less bone removal and generate lower stresses: a finite element analysis,” *J. Shoulder Elb. Surg.*, vol. 25, no. 5, pp. 823–830, 2016.
- [98] C. Rao, C. K. Fitzpatrick, P. J. Rullkoetter, L. P. Maletsky, R. H. Kim, and P. J. Laz, “A statistical finite element model of the knee accounting for shape and alignment variability,” *Med. Eng. Phys.*, vol. 35, no. 10, pp. 1450–1456, 2013.
- [99] A. Navacchia, P. J. Rullkoetter, P. Schütz, R. B. List, C. K. Fitzpatrick, and K. B.

- Shelburne, “Subject-specific modeling of muscle force and knee contact in total knee arthroplasty,” *J. Orthop. Res.*, vol. 34, no. 9, pp. 1576–1587, 2016.
- [100] I. Jolliffe, *Principal component analysis*. Springer, 2011.
- [101] A. O. Cifuentes and A. Kalbag, “A performance study of tetrahedral and hexahedral elements in 3-D finite element structural analysis,” *Finite Elem. Anal. Des.*, vol. 12, no. 3–4, pp. 313–318, 1992.
- [102] A. Ramos and J. A. Simoes, “Tetrahedral versus hexahedral finite elements in numerical modelling of the proximal femur,” *Med. Eng. Phys.*, vol. 28, no. 9, pp. 916–924, 2006.
- [103] R. Huiskes and E. Y. S. Chao, “A survey of finite element analysis in orthopedic biomechanics: the first decade,” *J. Biomech.*, vol. 16, no. 6, pp. 385–409, 1983.
- [104] P. J. Prendergast, “Finite element models in tissue mechanics and orthopaedic implant design,” *Clin. Biomech.*, vol. 12, no. 6, pp. 343–366, 1997.
- [105] R. S. Boorman, B. Kopjar, E. Fehring, R. S. Churchill, K. Smith, and F. A. Matsen, “The effect of total shoulder arthroplasty on self-assessed health status is comparable to that of total hip arthroplasty and coronary artery bypass grafting,” *J. Shoulder Elb. Surg.*, vol. 12, no. 2, pp. 158–163, 2003.
- [106] A. V. Deshmukh, M. Koris, D. Zurakowski, and T. S. Thornhill, “Total shoulder arthroplasty: Long-term survivorship, functional outcome, and quality of life,” *J. Shoulder Elb. Surg.*, vol. 14, no. 5, pp. 471–479, 2005.
- [107] E. M. Padegimas, M. Maltenfort, M. D. Lazarus, M. L. Ramsey, G. R. Williams, and S. Namdari, “Future Patient Demand for Shoulder Arthroplasty by Younger Patients: National Projections,” *Clin. Orthop. Relat. Res.*, vol. 473, no. 6, pp. 1860–1867, 2015.
- [108] S. A. Antuna, J. W. Sperling, R. H. Cofield, and C. M. Rowland, “Glenoid revision surgery after total shoulder arthroplasty,” *J. Shoulder Elb. Surg.*, vol. 10, no. 3, pp. 217–224, 2001.
- [109] K. Issa, T. Pierce, S. Josephs, B. A. Zikria, J. H. Medicine, and Q. Naziri, “Total Shoulder Arthroplasty Demographics , Incidence , and Complications — A Nationwide Inpatient Sample Database Study,” no. June 2017, 2016.
- [110] L. Favard, “Revision of total shoulder arthroplasty,” *Orthop. Traumatol. Surg. Res.*, vol. 99, no. 1, pp. S12–S21, 2013.
- [111] H. Alidousti, J. W. Giles, R. J. H. Emery, and J. Jeffers, “Spatial mapping of humeral head bone density,” *J. Shoulder Elb. Surg.*, vol. 26, no. 9, pp. 1653–1661, 2017.
- [112] C. Lorenz and N. Krahnstöver, “Generation of point-based 3D statistical shape models for anatomical objects,” *Comput. Vis. Image Underst.*, vol. 77, no. 2, pp. 175–191, 2000.
- [113] T. L. Bredbenner, R. L. Mason, L. M. Havill, E. S. Orwoll, and D. P. Nicolella, “Fracture risk predictions based on statistical shape and density modeling of the

- proximal femur,” *J. Bone Miner. Res.*, vol. 29, no. 9, pp. 2090–2100, 2014.
- [114] T. Okada *et al.*, “Automated Segmentation of the Liver from 3D CT Images Using Probabilistic Atlas and Multilevel Statistical Shape Model,” *Acad. Radiol.*, vol. 15, no. 11, pp. 1390–1403, 2008.
- [115] X. Zhang, J. Tian, K. Deng, Y. Wu, and X. Li, “Automatic liver segmentation using a statistical shape model with optimal surface detection,” *IEEE Trans. Biomed. Eng.*, vol. 57, no. 10 PART 2, pp. 2622–2626, 2010.
- [116] J. Lötjönen, S. Kivistö, J. Koikkalainen, D. Smutek, and K. Lauerma, “Statistical shape model of atria, ventricles and epicardium from short- and long-axis MR images,” *Med. Image Anal.*, vol. 8, no. 3, pp. 371–386, 2004.
- [117] W. Bai *et al.*, “A bi-ventricular cardiac atlas built from 1000+ high resolution MR images of healthy subjects and an analysis of shape and motion,” *Med. Image Anal.*, vol. 26, no. 1, pp. 133–145, 2015.
- [118] X. Tao, J. L. Prince, and C. Davatzikos, “Using a statistical shape model to extract sulcal curves on the outer cortex of the human brain,” *IEEE Trans. Med. Imaging*, vol. 21, no. 5, pp. 513–524, 2002.
- [119] D. Shen, E. H. Herskovits, and C. Davatzikos, “An adaptive-focus statistical shape model for segmentation and shape modeling of 3-D brain structures.,” *IEEE Trans. Med. Imaging*, vol. 20, no. 4, pp. 257–270, 2001.
- [120] K. T. Rajamani, M. A. Styner, H. Talib, G. Zheng, L. P. Nolte, and M. A. G. Ballester, “Statistical deformable bone models for robust 3D surface extrapolation from sparse data,” *Med. Image Anal.*, vol. 11, no. 2, pp. 99–109, 2007.
- [121] P. Vanden Berghe, J. Demol, F. Gelaude, and J. Vander Sloten, “Virtual anatomical reconstruction of large acetabular bone defects using a statistical shape model,” *Comput. Methods Biomech. Biomed. Engin.*, vol. 20, no. 6, pp. 577–586, 2017.
- [122] D. Kainmueller, H. Lamecker, S. Zachow, and H.-C. Hege, “An articulated statistical shape model for accurate hip joint segmentation.,” *Conf. Proc. Annu. Int. Conf. IEEE Eng. Med. Biol. Soc. IEEE Eng. Med. Biol. Soc. Annu. Conf.*, vol. 2009, pp. 6345–6351, 2009.
- [123] T. L. Bredbenner, T. D. Eliason, R. S. Potter, R. L. Mason, L. M. Havill, and D. P. Nicolella, “Statistical shape modeling describes variation in tibia and femur surface geometry between Control and Incidence groups from the Osteoarthritis Initiative database,” *J. Biomech.*, vol. 43, no. 9, pp. 1780–1786, 2010.
- [124] J. S. Coogan, D. G. Kim, T. L. Bredbenner, and D. P. Nicolella, “Determination of sex differences of human cadaveric mandibular condyles using statistical shape and trait modeling,” *Bone*, vol. 106, pp. 35–41, 2018.
- [125] K. Plessers *et al.*, “Virtual reconstruction of glenoid bone defects using a statistical shape model,” *J. Shoulder Elb. Surg.*, vol. 27, no. 1, pp. 160–166, 2018.
- [126] A. Fedorov *et al.*, “3D Slicer as an image computing platform for the Quantitative Imaging Network,” *Magn. Reson. Imaging*, vol. 30, no. 9, pp. 1323–1341, 2012.

- [127] E. A. Lalone, R. T. Willing, H. L. Shannon, G. J. W. King, and J. A. Johnson, "Accuracy assessment of 3D bone reconstructions using CT : an intro comparison," *Med. Eng. Phys.*, vol. 37, no. 8, pp. 729–738, 2015.
- [128] P. Cignoni *et al.*, "MeshLab: an open-source mesh processing tool," *Eurographics Ital. Chapter Conf.*, pp. 129–136, 2008.
- [129] H. Si, "TetGen, a Quality Tetrahedral Mesh Generator," *AMC Trans. Math. Softw.*, vol. 41, no. 2, p. 11, 2015.
- [130] Y. Pauchard *et al.*, "Interactive graph-cut segmentation for fast creation of finite element models from clinical ct data for hip fracture prediction," *Comput. Methods Biomech. Biomed. Engin.*, vol. 19, no. 16, pp. 1693–1703, 2016.
- [131] J. D. Evans, *Straightforward statistics for the behavioral sciences*. Thomson Brooks/Cole Publishing Co, 1996.
- [132] A. Jacobson *et al.*, "Glenohumeral anatomic study: a comparison of male and female shoulders with similar average age and BMI," *Bull. NYU Hosp. Jt. Dis.*, vol. 73, no. S1, pp. S68--S68, 2015.
- [133] D. D. Robertson, J. Yuan, L. U. Bigliani, E. L. Flatow, and K. Yamaguchi, "Three-dimensional analysis of the proximal part of the humerus: Relevance to arthroplasty," *J. Bone Jt. Surg. - Ser. A*, vol. 82, no. 11, pp. 1594–1602, 2000.
- [134] M. J. Tingart, M. Apreleva, D. von Stechow, D. Zurakowski, and J. J. Warner, "The cortical thickness of the proximal humeral diaphysis predicts bone mineral density of the proximal humerus," *J. Bone Jt. Surg.*, vol. 85, no. 4, pp. 611–617, 2003.
- [135] F. Barvencik *et al.*, "Age- and sex-related changes of humeral head microarchitecture: Histomorphometric analysis of 60 human specimens," *J. Orthop. Res.*, vol. 28, no. 1, pp. 18–26, 2010.
- [136] S. M. M. Roosa, A. L. Hurd, H. Xu, R. K. Fuchs, and S. J. Warden, "Age-related changes in proximal humerus bone health in healthy, white males," *Osteoporos. Int.*, vol. 23, no. 12, pp. 2775–2783, 2012.
- [137] K. C. *et al.*, "Age and gender as determinants of the bone quality of the greater tuberosity: A HR-pQCT cadaver study," *BMC Musculoskelet. Disord.*, vol. 13, p. 221, 2012.
- [138] A.-M. Laval-Jeantet, C. Bergot, R. Carroll, and F. Garcia-Schaefer, "Cortical bone senescence and mineral bone density of the humerus," *Calcif. Tissue Int.*, vol. 35, no. 1, pp. 268–272, 1983.
- [139] F. Gelaude, T. Clijmans, P. L. Broos, B. Lauwers, and J. Vander Sloten, "Computer-aided planning of reconstructive surgery of the innominate bone: Automated correction proposals," *Comput. Aided Surg.*, vol. 12, no. 5, pp. 286–294, 2007.
- [140] F. Verhaegen, K. Plessers, O. Verborgt, L. Scheys, and P. Debeer, "Can the contralateral scapula be used as a reliable template to reconstruct the eroded scapula during shoulder arthroplasty?," *J. Shoulder Elb. Surg.*, vol. 27, no. 6, pp.

1133–1138, 2018.

- [141] L. Shi, J. F. Griffith, J. Huang, and D. Wang, “Excellent side-to-side symmetry in glenoid size and shape,” *Skeletal Radiol.*, vol. 42, no. 12, pp. 1711–1715, 2013.
- [142] G. Diederichs, J. Korner, J. Goldhahn, and B. Linke, “Assessment of bone quality in the proximal humerus by measurement of the contralateral site: A cadaveric analyze,” *Arch. Orthop. Trauma Surg.*, vol. 126, no. 2, pp. 93–100, 2006.
- [143] D. F. Massimini, G. Li, and J. P. Warner, “Glenohumeral contact kinematics in patients after total shoulder arthroplasty,” *J. Bone Jt. Surg. - Ser. A*, vol. 92, no. 4, pp. 916–926, 2010.
- [144] I. K. Y. Lo, R. B. Litchfield, S. Griffin, K. Faber, S. D. Patterson, and A. Kirkley, “Quality-of-life outcome following hemiarthroplasty or total shoulder arthroplasty in patients with osteoarthritis: A prospective, randomized trial,” *J. Bone Jt. Surg. - Ser. A*, vol. 87, no. 10, pp. 2178–2185, 2005.
- [145] D. M. Rispoli, J. W. Sperling, G. S. Athwal, C. D. Schleck, and R. H. Cofield, “Humeral head replacement for the treatment of osteoarthritis,” *J. Bone Jt. Surg. - Ser. A*, vol. 88, no. 12, pp. 2637–2644, 2006.
- [146] J. W. Sperling, R. H. Cofield, and C. M. Rowland, “Neer hemiarthroplasty and Neer total shoulder arthroplasty in patients fifty years old or less: Long-term results,” *J. Bone Jt. Surg. - Ser. A*, vol. 80, no. 4, pp. 464–473, 1998.
- [147] D. Bryant, R. Litchfield, M. Sandow, G. M. Gartsman, G. Guyatt, and A. Kirkley, “A comparison of pain, strength, range of motion, and functional outcomes after hemiarthroplasty and total shoulder arthroplasty in patients with osteoarthritis of the shoulder: A systematic review and meta-analysis,” *J. Bone Jt. Surg. - Ser. A*, vol. 87, no. 9 I, pp. 1947–1956, 2005.
- [148] T. M. Turner, D. R. Sumner, R. M. Urban, R. Igloria, and J. O. Galante, “Maintenance of Proximal Cortical Bone with Use of a Less Stiff Femoral Component in Hemiarthroplasty of the Hip without Cement,” *J. Bone Jt. Surg. (American Vol.)*, vol. 79, no. 9, pp. 1381–1390, 1997.
- [149] D. R. Sumner and J. O. Galante, “Determinants of stress shielding: Design versus materials versus interface,” *Clin. Orthop. Relat. Res.*, no. 274, pp. 202–212, 1992.
- [150] R. Huiskes, “The various stress patterns of press-fit, ingrown, and cemented femoral stems,” *Clin. Orthop. Relat. Res.*, no. 261, pp. 27–38, 1990.
- [151] S. Arno *et al.*, “Evaluation of femoral strains with cementless proximal-fill femoral implants of varied stem length,” *Clin. Biomech.*, vol. 27, no. 7, pp. 680–685, 2012.
- [152] R. L. Austman, G. J. W. King, and C. E. Dunning, “Bone stresses before and after insertion of two commercially available distal ulnar implants using finite element analysis,” *J. Orthop. Res.*, vol. 29, no. 9, pp. 1418–1423, 2011.
- [153] R. Bieger, A. Ignatius, R. Decking, L. Claes, H. Reichel, and L. Dürselen, “Primary stability and strain distribution of cementless hip stems as a function of implant design,” *Clin. Biomech.*, vol. 27, no. 2, pp. 158–164, 2012.

- [154] B. J. Erickson and F. A. Cordasco, "Why short-stemmed implants are the implant of choice in a 60-year-old with shoulder osteoarthritis," *Semin. Arthroplasty*, vol. 29, no. 2, pp. 72–76, 2018.
- [155] B. Kadum, H. Hassany, M. Wadsten, A. Sayed-Noor, and G. Sjöden, "Geometrical analysis of stemless shoulder arthroplasty: a radiological study of seventy TESS total shoulder prostheses," *Int. Orthop.*, vol. 40, no. 4, pp. 751–758, 2016.
- [156] X. Wang *et al.*, "Topological design and additive manufacturing of porous metals for bone scaffolds and orthopaedic implants: A review," *Biomaterials*, vol. 83, pp. 127–141, 2016.
- [157] P. Tack, J. Victor, P. Gemmel, and L. Annemans, "3D-printing techniques in a medical setting: A systematic literature review," *Biomed. Eng. Online*, vol. 15, no. 1, pp. 1–21, 2016.
- [158] S. Gross and E. W. Abel, "A finite element analysis of hollow stemmed hip prostheses as a means of reducing stress shielding of the femur," *J. Biomech.*, vol. 34, no. 8, pp. 995–1003, 2001.
- [159] J. Schmidt and M. H. Hackenbroch, "The Cenos hollow stem in total hip arthroplasty: first experiences in a prospective study," *Arch. Orthop. Trauma Surg.*, vol. 113, no. 3, pp. 117–120, 1994.
- [160] C. Mattheck, U. Vorberg, and C. Kranz, "Effects of hollow shaft endoprosthesis on stress distribution in cortical bone," *Biomed. Tech. (Berl.)*, vol. 35, no. 12, pp. 316–319, 1990.
- [161] C. T. Yang, H. W. Wei, H. C. Kao, and C. K. Cheng, "Design and test of hip stem for medullary revascularization," *Med. Eng. Phys.*, vol. 31, no. 8, pp. 994–1001, 2009.
- [162] D. L. Fat, J. Kennedy, R. Galvin, F. O'Brien, F. M. Grath, and H. Mullett, "The Hounsfield value for cortical bone geometry in the proximal humerus—an in vitro study," *Skeletal Radiol.*, vol. 41, no. 5, pp. 557–568, 2012.
- [163] G. Dahan, N. Trabelsi, O. Safran, and Z. Yosibash, "Verified and validated finite element analyses of humeri," *J. Biomech.*, vol. 49, no. 7, pp. 1094–1102, 2016.
- [164] B. Helgason *et al.*, "The influence of the modulus-density relationship and the material mapping method on the simulated mechanical response of the proximal femur in side-ways fall loading configuration," *Med. Eng. Phys.*, vol. 38, no. 7, pp. 679–689, 2016.
- [165] D. Christian Wirtz *et al.*, "Critical evaluation of known bone material properties to realize anisotropic FE-simulation of the proximal femur," *J. Biomech.*, vol. 33, pp. 1325–1330, 2000.
- [166] B. Helgason, E. Perilli, E. Schileo, F. Taddei, S. Brynjólfsson, and M. Viceconti, "Mathematical relationships between bone density and mechanical properties: A literature review," *Clin. Biomech.*, vol. 23, no. 2, pp. 135–146, 2008.
- [167] J. A. Grant, N. E. Bishop, N. Götzen, C. Sprecher, M. Honl, and M. M. Morlock, "Artificial composite bone as a model of human trabecular bone: The implant-

- bone interface,” *J. Biomech.*, vol. 40, no. 5, pp. 1158–1164, 2007.
- [168] K. R. S. Holzbaur, W. M. Murray, and S. L. Delp, “A model of the upper extremity for simulating musculoskeletal surgery and analyzing neuromuscular control,” *Ann. Biomed. Eng.*, vol. 33, no. 6, pp. 829–840, 2005.
- [169] S. L. Delp *et al.*, “OpenSim: Open-Source Software to Create and Analyze Dynamic Simulations of Movement,” vol. 54, no. 11, pp. 1940–1950, 2007.
- [170] G. Wu *et al.*, “ISB recommendation on definitions of joint coordinate systems of various joints for the reporting of human joint motion—Part II: shoulder, elbow, wrist and hand,” *J. Biomech.*, vol. 38, no. 5, pp. 981–992, 2004.
- [171] J. R. Lawrence, *Advances in laser materials processing: technology, research and applications*. Woodhead Publishing, 2017.
- [172] R. L. Austman, B. J. B. Beaton, C. E. Quenneville, G. J. W. King, K. D. Gordon, and C. E. Dunning, “The Effect of Distal Ulnar Implant Stem Material and Length on Bone Strains,” *J. Hand Surg. Am.*, vol. 32, no. 6, pp. 848–854, 2007.
- [173] S. Arabnejad, B. Johnston, M. Tanzer, and D. Pasini, “Fully porous 3D printed titanium femoral stem to reduce stress-shielding following total hip arthroplasty,” *J. Orthop. Res.*, vol. 35, no. 8, pp. 1774–1783, 2017.

Appendices

Appendix A. Specimen Reconstruction using a compact SSM/SDM

For each specimen, the root mean square error (RMSE) in reconstructing the surface of the humerus using the first 6 PCs of the SSM, and the RMSE in reconstructing the surface of the scapula using the first 14 PCs were computed. The maximum RMSE among all the specimens in reconstructing the surface of the humerus using the compact SSM was 4.1 mm, while the mean RMSE was 1.8 mm. The maximum RMSE in reconstructing the surface of the scapula using the compact SSM was 2.3 mm, while the mean RMSE was 1.6 mm.

The density distribution of each specimen was also reconstructed using the first 6 PCs of the SDM for the humerus, and the first 14 PCs for the scapula and then was compared with its original CT. We were able to capture the pattern of density distribution for each specimen for both the humerus and scapula to a great extent (Figure A.1).

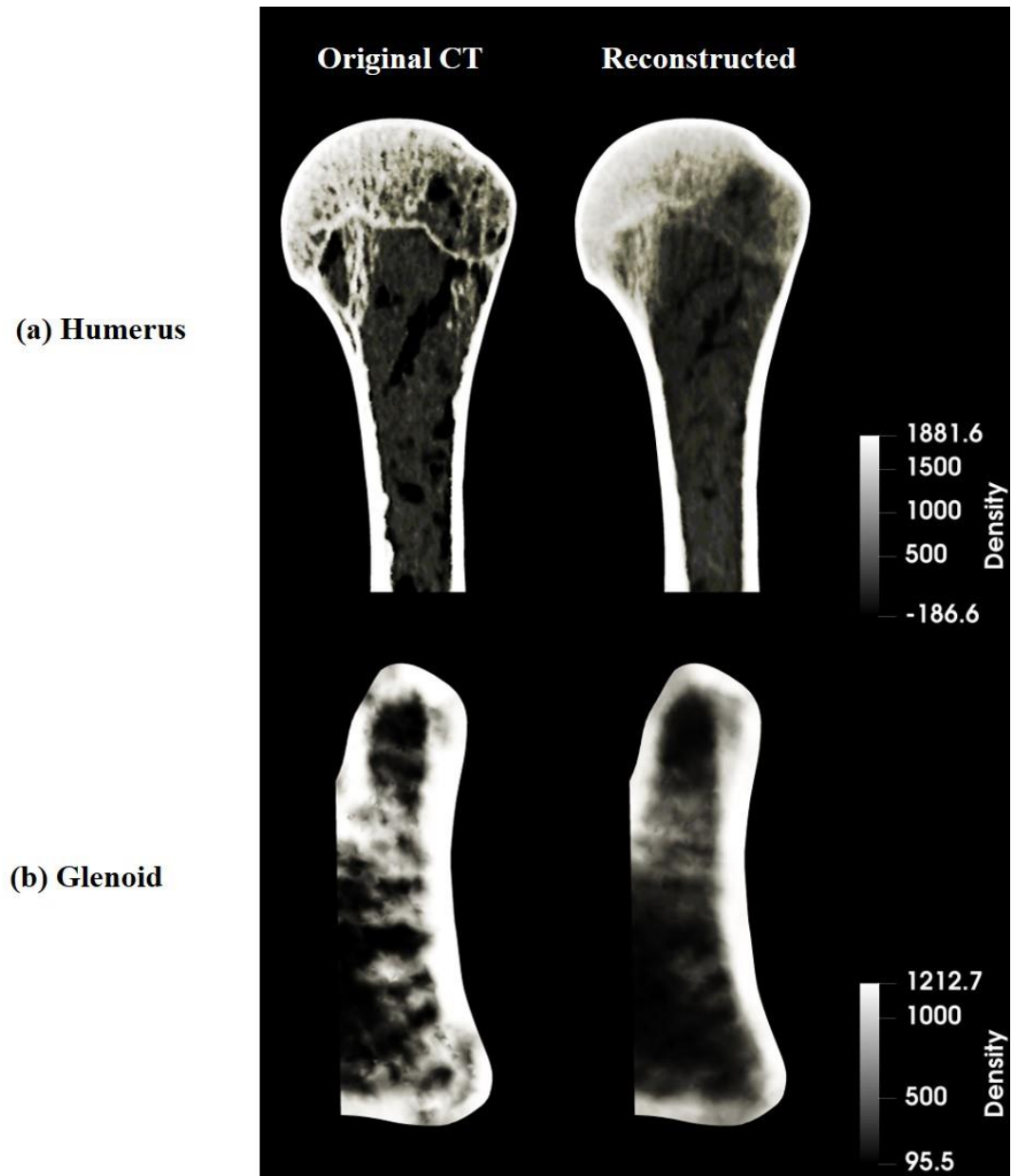


Figure A.1 Comparing the original CT image of the specimen with the maximum reconstruction error (left) with its reconstructed model (right); (a) for the humerus, (b) for the glenoid

Appendix B. SSM Robustness Analysis

A subset of 10 scapulae was chosen for intra-/inter- observer error analysis. The average absolute surface to surface distance over the entire scapula was quantified between the mean shape and meshes transformed +1 standard deviation (SD) along each PC (Figure B.1). Using the same CT-based models, a second SSM was generated by a second observer, and comparisons of the resulting mean shape and PCs were performed (in terms of the average absolute surface to surface distances). Finally, the PC values required to reproduce the shape of a specific scapula from the training set were compared for the two SSMs.

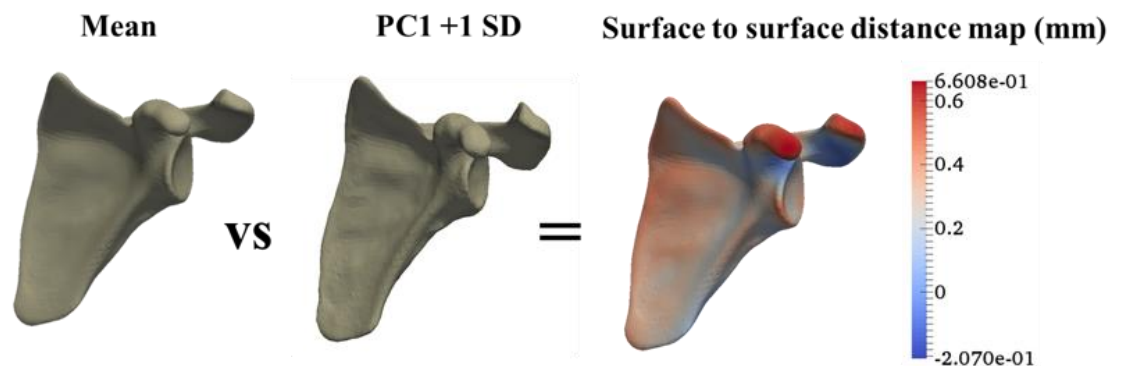


Figure B.1 An example of the absolute surface to surface distance between the mean and +1 SD along a PC

The first five (of nine) PCs accounted for 95.2% of the variation in the subset (Figure B.2). A similar trend was observed in the average surface to surface distances associated with transforming along each PC (Figure B.2). The average surface to surface distance between the mean shapes of the two different SSMs was 0.002 mm, and the PCs computed for either SSM corresponded in terms of their influence on the model shape. Finally, similar scaling of PCs from either SSM was required to reproduce the shape of two of the training set specimens (Figure B.3), further suggesting the robustness of the SSMs.

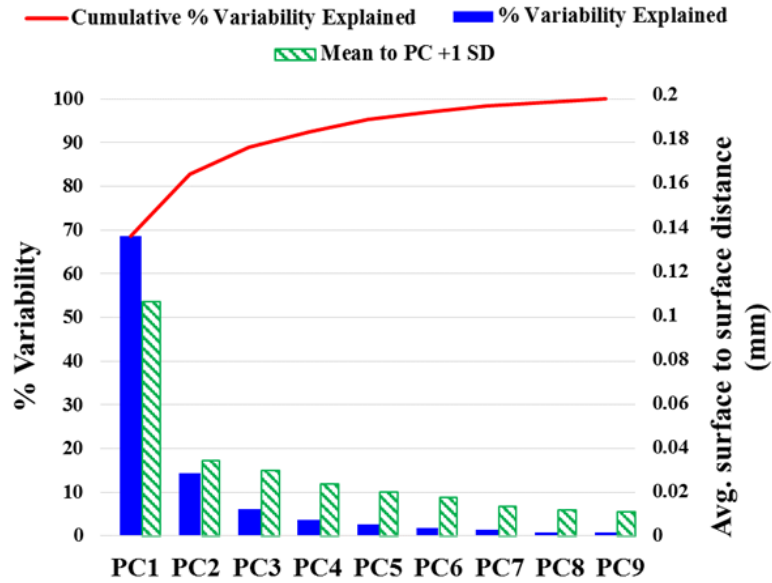


Figure B.2 The percentage of variability in the training set explained by each PC and cumulative percentage of variability (read from the left side) as well as the surface to surface distance between the mean shape and +1 SD of each PC (read from the right scale)

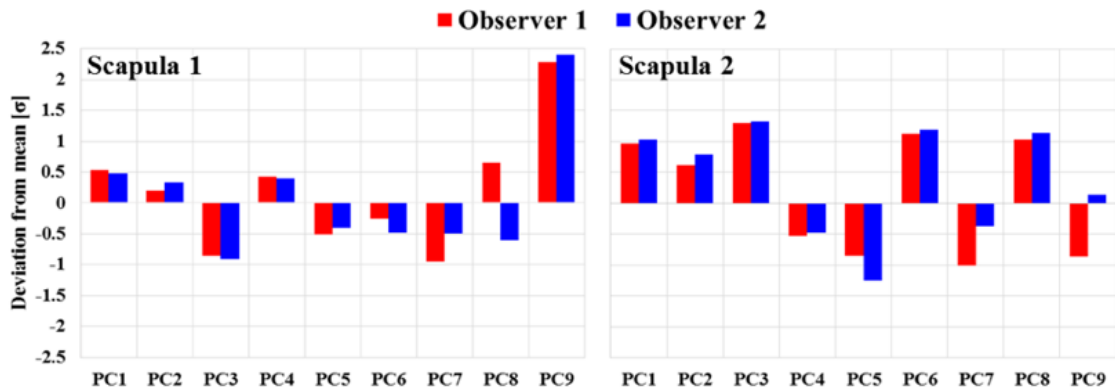
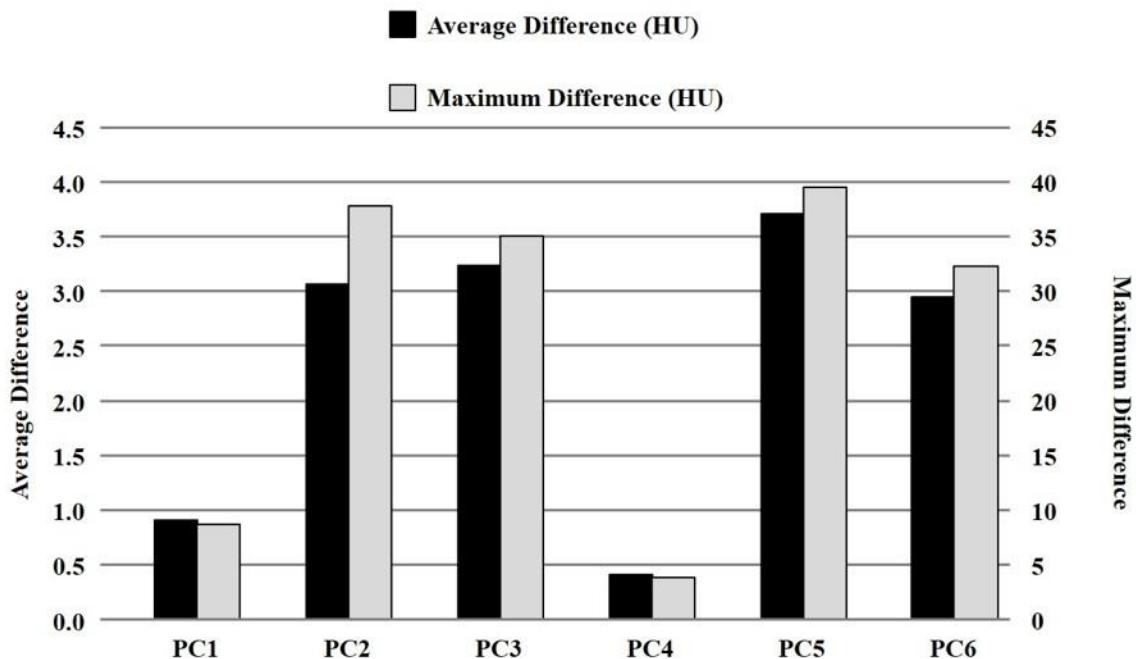


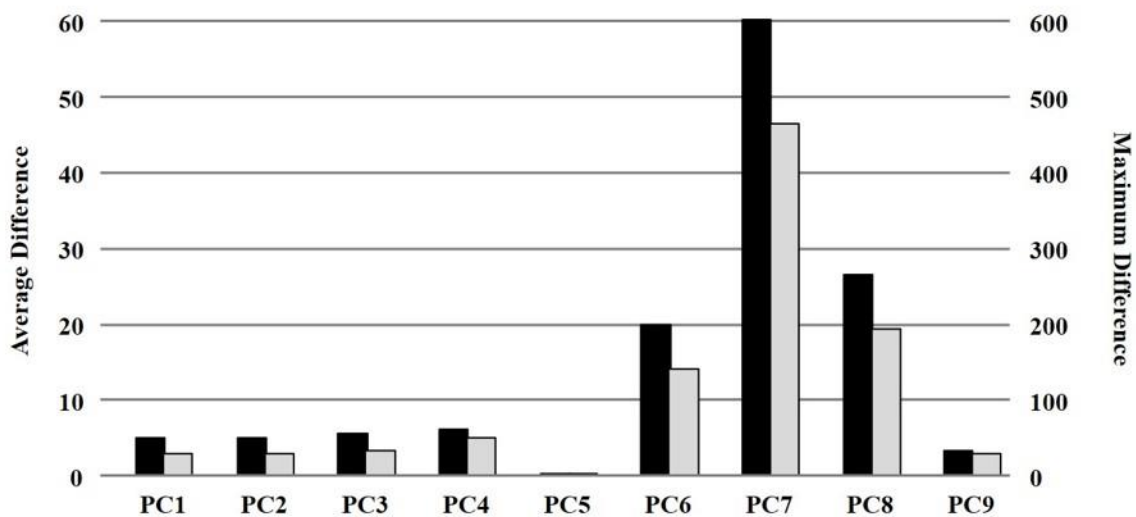
Figure B.3 The SD values of each PC required to produce two scapulae in the training set with two SSMs generated by different observers

Appendix C. SDM Robustness Analysis

To assess the robustness of the SDMs against particular specimens, we used the add-one-in-approach. One additional specimen was included in the sets of humeri and scapulae, after which PCA was performed again to determine the sensitivity of the spatial distribution of the densities to the particular specimens used in the study. The additional bone instances were excluded from the original SSMs and SDMs, as the CT image of the extra humerus was missing its corresponding scapula and vice versa. In the evaluation of the robustness of the model, the average and the maximum of the absolute differences in the densities across all the nodes of the SDM based on 75 specimens and the one including the extra specimen, by a deviation of one σ along the first few PCs, were calculated (Figure C.1).



(a) Humerus



(b) Scapula

Figure C.1 The average and the maximum of the absolute differences in densities in HU across all the nodes by a deviation of σ along the first few PCs; (a) for the humerus, (b) for the scapula

Curriculum Vitae

Name: Pendar Soltanmohammadi

Post-secondary Education and Degrees: Sharif University of Technology
Tehran, Iran
2012-2016 B.Sc.

Western University
London, Ontario, Canada
2017-2019 M.E.Sc.

Related Work Experience Research and Teaching Assistant
Western University
2017-2019

Publications:

P. Soltamohammadi and R. Willing, Development of a Statistical Density Model of the Shoulder, The Orthopaedic Research Society (ORS), Austin, TX, USA (Poster, February 2019).

P. Soltamohammadi and R. Willing, Investigating the Effects of Demographics on Shoulder Shape and Density using Statistical Shape and Density Modeling, Ontario Biomechanics Conference (OBC), Alliston, ON, Canada (Poster, March 2019).

P. Soltamohammadi and R. Willing, The Effects of Sex and Age on Shoulder Density for Population-based Design of Orthopedic Implants, London Health Research Day (LHRD), London, ON, Canada (Poster, April 2019).

P. Soltamohammadi and R. Willing, The Effects of Demographics on Shoulder Shape and Density for Population-based Design of Orthopedic Implants, the Canadian Society for Mechanical Engineering (CSME), London, ON, Canada (Podium Presentation, June 2019).

P. Soltamohammadi and R. Willing, Development of a Statistical Shape and Density Model of the Shoulder, the International Combined Orthopaedic Research Societies (ICORS), Montréal, QC, Canada (Podium Presentation, June 2019).

P. Soltamohammadi, G. Athwal and R. Willing, Hollow-stemmed Implants Can Be a Solution to the Problem of Stress Shielding of Proximal Humerus After Shoulder Arthroplasty, International Society for Technology in Arthroplasty (ISTA), Toronto, ON, Canada (ePoster, October 2019).